Master Thesis

Study of Super-Kamiokande detector calibration using cosmogenic neutron capture on Gadolinium

（ガドリニウムによる核破砕中性子捕獲を用いたスーパーカミオカンデ検出器較正の研究）

March 19, 2023

Department of Physics, Graduate School of Science
The University of Tokyo
東京大学大学院理学系研究科物理学専攻

Shizuka Shima
志摩靜香

Abstract

The Super-Kamiokande experiment is an experiment observing neutrinos and searching for proton decay using the world's largest water Cherenkov detector. In the summer of 2020, the gadolinium was added to pure water in Super-Kamiokande. This resulted in a gadolinium concentration of about 0.01%, and significantly improved the efficiency of neutron detection. Furthermore, in the summer of 2022, additional Gd was introduced, increasing the Gd concentration from 0.01% to 0.03%.

In this study, spallation neutrons are used for calibrating and monitoring the Super-Kamiokande detector. Spallation neutron is the neutron produced by the spallation reaction of cosmic ray muons with oxygen nuclei in water. There are two advantages of using spallation neutrons. First, they can be detected across the entire detector, which allows us to investigate detailed position dependence. Second, sufficient statistics can be obtained in a short time. They have also the disadvantages that the detected energy is low and background is difficult to remove, and they are affected by pile-up. The event selection for spallation neutrons has been developed to take these into account.

The stability of the detector response at ordinarily times and the Gd concentration during Gd-loading are monitored using these properties. In the former, the stability of the detector was checked by evaluating the energy and Gd concentration. As a result, the energy detected by the detector was stable at about $\pm 1\%$, and the Gd concentration was also stable at about $\pm 2\%$. In the latter, the transition of Gd concentration during Gd-loading was checked by evaluating the number of spallation neutron signals and the time constant. We checked that Gd was loaded as expected.

An energy calibration method is studied using the spallation neutron. Firstly, to check if the neutron capture signal by Gd can be used to evaluate the energy scale of electron events, the position dependence of the energy scale of neutron and electron is compared using MC simulation. The result is that the energy scale for electron and neutron events are consistent within about $\pm 2\%$ of the entire detector. This is however a larger deviation compared to the goal of correcting positional dependence to within 0.5%. It will be important to understand the causes of this in the future. Next, to check if the MC simulation reproduces the data, the position dependence of the energy scale for neutrons is compared between the data and MC simulation. As a result, it is found that the closer to the barrel wall of the tank, the larger the energy of the MC simulation compared to the data, and at the bottom of the tank, the MC simulation differ from the data by about $\pm 1\%$. Since energy reconstruction is carried out using MC simulations, it is important to investigate these in more detail in the future and to improve the MC simulation to better reproduce the data.

Contents

Chapter 1

Physics Motivation

In this thesis, the energy calibration of Super-Kamiokande for the observation of solar neutrino and Diffuse Supernova Neutrino Background (DSNB), which are physical targets in a few to tens of MeV (the low energy region in Super-Kamiokande), is discussed. Firstly, in this chapter, explanation of neutrino and introduction of solar neutrino and DSNB are given.

1.1 Neutrino

Neutrinos are elementary particles with no electric charge. They interact with other particles via the weak force and gravity only. Neutrinos interact with other matter only rarely. They were predicted to exist by Pauli in 1930 to explain the missing energy in beta decays, and were first observed by C. Cowan and F. Reines in 1956 [1]. If we can observe neutrinos produced in the Universe, we can investigate the phenomena occurring at their source. So far, astrophysical neutrinos have been observed from fusion reactions in the center of the Sun [2], supernova explosions [3], and blazars [4].

1.1.1 Neutrino oscillation

Neutrino oscillation is one of the important properties of neutrinos. Neutrino oscillation is a phenomenon in which one flavor of neutrino stochastically changes to another flavor with time evolution. Neutrino was thought to have no mass in the standard model of particle physics. However, neutrino oscillation was discovered with observations of atmospheric and solar neutrinos, revealing that neutrinos have masses [[5],[6]]. The neutrino flavor eigenstates $|\nu_\alpha\rangle$ ($\alpha = e, \mu, \tau$) can be expressed

using their mass eigenstates $|\nu_i\rangle$ $(i = 1, 2, 3)$:

$$|\nu_\alpha\rangle = \sum_{i=0} U_{\alpha i} |\nu_i\rangle \tag{1.1}$$

where U is a 3×3 unitary matrix which is called Pontecorvo-Maki-Nakagawa-Sakata (PMNS) matrix [7]. This PMNS matrix can be written as,

$$
\begin{aligned}
U &= \begin{pmatrix} 1 & 0 & 0 \\ 0 & c_{23} & s_{23} \\ 0 & -s_{23} & c_{23} \end{pmatrix} \begin{pmatrix} c_{13} & 0 & s_{13}e^{-i\delta_{\mathrm{CP}}} \\ 0 & 1 & 0 \\ -s_{13}e^{i\delta_{\mathrm{CP}}} & 0 & c_{13} \end{pmatrix} \begin{pmatrix} c_{12} & s_{12} & 0 \\ -s_{12} & c_{12} & 0 \\ 0 & 0 & 1 \end{pmatrix} \\
&= \begin{pmatrix} c_{12}s_{13} & s_{12}c_{13} & s_{13}e^{-i\delta_{\mathrm{CP}}} \\ -s_{12}c_{23} - c_{12}s_{13}s_{23}e^{-i\delta_{\mathrm{CP}}} & c_{12}c_{23} - s_{12}s_{13}s_{23}e^{i\delta_{\mathrm{CP}}} & c_{13}s_{23} \\ s_{12}s_{23} - c_{12}s_{13}s_{23}e^{i\delta_{\mathrm{CP}}} & c_{12}c_{23} - s_{12}s_{13}s_{23}e^{-i\delta_{\mathrm{CP}}} & c_{13}c_{23} \end{pmatrix},
\end{aligned}
\tag{1.2}
$$

where $c_{ij} = \cos\theta_{ij}$ and $s_{ij} = \sin\theta_{ij}$ which are the parameters representing the degree of mixing of mass eigenstates, and are called neutrino mixing angles. δ_{CP} represents the CP phase in the lepton sector, indicating that the CP symmetry of neutrino is broken when $\sin\delta_{\mathrm{CP}} \neq 0$, but this has not yet been observed. In vacuum, the time evolution of the neutrino mass eigenstate $|\nu_i(t)\rangle$ satisfies the following Schrödinger equation,

$$-i\frac{d}{dt}|\nu_i\rangle = \mathcal{H}|\nu_i(t)\rangle = E_i |\nu_i(t)\rangle \tag{1.3}$$

$$|\nu_i\rangle = \exp(-iE_i t)|\nu_i(0)\rangle, \tag{1.4}$$

where E_i is the energy of mass eigenstate, $\mathcal{H}$ represents Hamiltonian and t is a travering time of the neutrino. From Eq 1.1, the time evolution of a flavor eigenstate $|\nu_\alpha(t)\rangle$ can be written as

$$|\nu_\alpha(t)\rangle = \sum_i U_{\alpha i}\exp(-iE_i t)|\nu_i(0)\rangle \tag{1.5}$$

The amplitude when ν_β is detected at time t starting from ν_α is

$$
\begin{aligned}
A(\nu_\alpha \to \nu_\beta) = \langle \nu_\beta | \nu_\alpha(t)\rangle &= \sum_i \sum_j \exp(-iE_i t)U_{\alpha i}U_{\beta i}^\dagger \langle \nu_i | \nu_j\rangle \\
&= \sum_i e^{-iE_i t}U_{\alpha i}U_{\beta i}^\dagger,
\end{aligned}
\tag{1.6}
$$

The neutrino oscillation probability $(\nu_\alpha \to \nu_\beta)$ in vacuum is given as follows.

$$
\begin{aligned}
P(\nu_\alpha \to \nu_\beta) &= |A(\nu_\alpha \to \nu_\beta)|^2 \\
&= \sum_i \sum_j U_{\alpha i}U_{\beta i}^\dagger U_{\alpha j}^\dagger U_{\beta j}\exp(-i(E_i - E_j)t)
\end{aligned}
\tag{1.7}
$$

When the squared mass of a neutrinos m_i^2 are small compared to their momenta $\boldsymbol{p}$, an approximation is as follow,

$$E_i = \sqrt{p_i^2 + m_i^2} \approx p_i + \frac{m_i^2}{2p_i} \approx p + \frac{m_i^2}{2E_i}, \tag{1.8}$$

where p_i and m_i represent the momentum eigenvalue and mass eigenvalue, respectively. Then, Eq 1.7 becomes

$$\begin{aligned}
P(\nu_\alpha \to \nu_\beta) &= \sum_{i,j} U_{\alpha i} U_{\beta i}^\dagger U_{\alpha j}^\dagger U_{\beta j} \exp\left(-i\frac{(m_i^2 - m_j^2)}{2E}t\right) \\
&= \sum_{i,j} U_{\alpha i} U_{\beta i}^\dagger U_{\alpha j}^\dagger U_{\beta j} \exp\left(-i\frac{\Delta m_{ij}^2}{2E}t\right) \\
&= \sum_{i,j} U_{\alpha i} U_{\beta i}^\dagger U_{\alpha j}^\dagger U_{\beta j} \exp\left(-i\frac{\Delta m_{ij}^2}{2E}L\right) \\
&= \delta_{\alpha\beta} - 4\sum_{i<j} \text{Re}[U_{\alpha i} U_{\beta i}^\dagger U_{\alpha j}^\dagger U_{\beta j}] \sin^2\left(\frac{\Delta m_{ij}^2}{4E}L\right) \\
&\quad + 2\sum_{i<j} \text{Im}[U_{\alpha i} U_{\beta i}^\dagger U_{\alpha j}^\dagger U_{\beta j}] \sin\left(\frac{\Delta m_{ij}^2}{2E}L\right),
\end{aligned} \tag{1.9}$$

where $\Delta m_{ij}^2 = m_i^2 - m_j^2$ is a mass-squared difference, E is the average neutrino energy $E \simeq \gamma(m_i + m_j)/2$, t is replaced with a travel distance $L = ct$ and $\delta_{\alpha\beta}$ is the Kronecker's delta.

Considering two generations of neutrino oscillation at $\nu_e \leftrightarrow \nu_\mu$ for simplicity, since the unitary matrix is written as

$$U_{2\times 2} = \begin{pmatrix} \cos\theta & \sin\theta \\ -\sin\theta & \cos\theta \end{pmatrix} \tag{1.10}$$

the neutrino oscillation probability $P(\nu_e \leftrightarrow \nu_\mu)$ is written as,

$$\begin{aligned}
P(\nu_e \leftrightarrow \nu_\mu) &= \sin^2 2\theta \sin^2\left(\frac{\Delta m^2}{4E}L\right) \\
&= \sin^2 2\theta \sin^2\left(\frac{1.27\Delta m^2[\text{eV}^2]L[\text{m}]}{E[\text{MeV}]}\right)
\end{aligned} \tag{1.11}$$

From Eq 1.11, it can be seen that neutrino oscillation occurs when there is a difference in the neutrino mass eigenvalues.

Neutrino oscillation parameters

Neutrino oscillation in a vacuum can be described by six parameters:

$$\theta_{12},\ \theta_{23},\ \theta_{13},\ \Delta m_{21}^2,\ \Delta m_{32}^2,\ \delta_{\text{CP}} \tag{1.12}$$

These parameters have been measured by using various neutrino sources: solar, reactor, atmospheric and accelerator neutrinos. The best fit values of global analysis of neutrino data are summarized in Table 1.1. There are two possibilities of mass ordering, which depend on the ordering of the neutrino mass eigenstates. This is because neutrino oscillation experiments can mainly measure the absolute value of δm^2, but they are not very sensitive to its sign. The order $m_1 < m_2 < m_3$ is called Normal Ordering (NO), and the order $m_3 < m_1 < m_2$ is called Inverted Ordering (IO).

Table 1.1: Neutrino oscillation parameters [8]. NO is normal mass ordering and IO is inverted mass ordering.

Oscillation parameter	Best fit value
$\sin^2\theta_{12}$	0.307 ± 0.013
$\sin^2\theta_{23}$ (IO)	0.539 ± 0.022
$\sin^2\theta_{23}$ (NO)	0.546 ± 0.021
$\sin^2\theta_{13}$	$(2.20 \pm 0.07) \times 10^{-2}$
Δm_{21}^2	$(7.53 \pm 0.18) \times 10^{-5}\,\text{eV}^2$
Δm_{32}^2 (IO)	$(-2.536 \pm 0.034) \times 10^{-3}\,\text{eV}^2$
Δm_{32}^2 (NO)	$(2.453 \pm 0.033) \times 10^{-3}\,\text{eV}^2$

1.2 Solar neutrino

Solar neutrino is neutrino produced from solar fusion reaction. 2×10^{38} electron neutrinos per second are produced mainly through the two processes called pp-chain and CNO cycle. Solar neutrino observations have been carried out at Super-Kamiokande [9], Kamiokande [10], Homestake[11], KamLAND [12], SAGE [13], GALLEX/GNO [14], Borexino [15], and Sudbury Neutrino Observatory (SNO) [6].

1.2.1 Solar neutrino production

pp-chain

In the pp-chain, solar (electron) neutrinos are produced by the following reactions:

- pp neutrino

$$p + p \rightarrow {}^2\mathrm{H} + e^+ + \nu_e \tag{1.13}$$

- pep neutrino

$$p + e^- + p \rightarrow {}^2\mathrm{H} + \nu_e \tag{1.14}$$

- hep neutrino

$${}^3\mathrm{He} + p \rightarrow {}^4\mathrm{He} + e^+ + \nu_e \tag{1.15}$$

- ${}^7\mathrm{Be}$ neutrino

$${}^7\mathrm{Be} + e^- \rightarrow {}^7\mathrm{Li} + \nu_e \tag{1.16}$$

- ${}^8\mathrm{B}$ neutrino

$${}^8\mathrm{B} + e^- \rightarrow {}^8\mathrm{Be}^* + e^+ + \nu_e \tag{1.17}$$
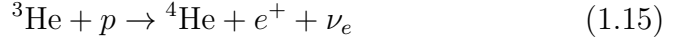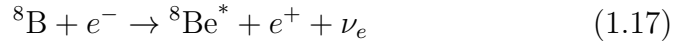
CNO cycle

In the CNO cycle, solar neutrinos are produced by the following reactions:

- ${}^{13}\mathrm{N}$ neutrino

$${}^{13}\mathrm{N} \rightarrow {}^{13}\mathrm{C} + e^+ + \nu_e \tag{1.18}$$

- ${}^{15}\mathrm{O}$ neutrino

$${}^{15}\mathrm{O} \rightarrow {}^{15}\mathrm{N} + e^+ + \nu_e \tag{1.19}$$

- ${}^{17}\mathrm{F}$ neutrino

$${}^{17}\mathrm{F} \rightarrow {}^{17}\mathrm{O} + e^+ + \nu_e \tag{1.20}$$

Since the central temperature of the Sun is about 10^7 K, the pp chain is dominant (about 99%). Figure 1.1 shows the solar neutrino energy spectrum predicted from the standard solar model. The pep neutrinos and ${}^7\mathrm{Be}$ neutrinos are produced with two-body final state, so they have a single energy spectrum, while all the others are produced with three-body final state, so they have a broad energy spectrum. At Super-Kamiokande, the energy threshold is 3.5 MeV, so ${}^8\mathrm{B}$ neutrinos with a relatively large flux above 3.5 MeV can be observed.

1.2.2 MSW effect of solar neutrino

MSW effect

As neutrinos pass through matter, they cause elastic scattering with the electrons, protons and neutrons in that matter, and the matter field acts on the neutrinos. The neutral-current interactions occur in all neutrino flavor states via a neutral current Z boson exchange, whereas the charged-current reactions occur only in electron neutrinos via a charged current $W^\pm$ boson
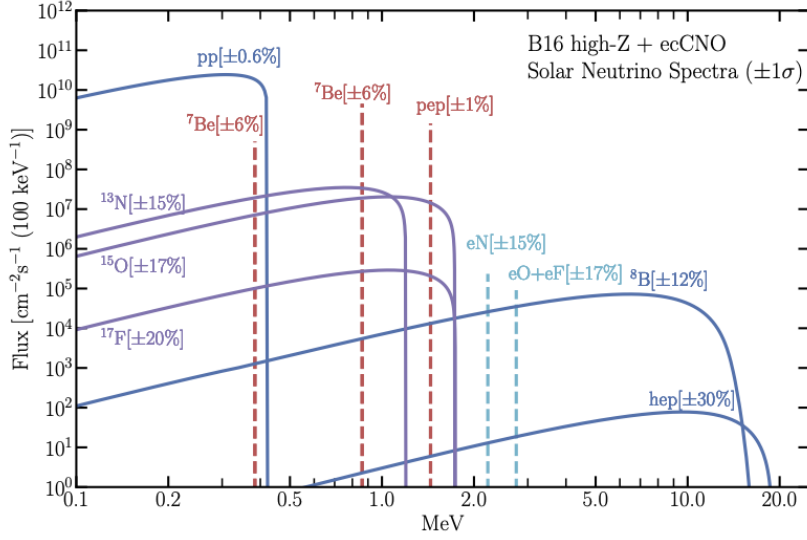
Figure 1.1: Energy spectrum of the solar neutrino [16]

exchange. The charged current interaction affects the oscillation transition due to the additional contribution to the Hamiltonian. The effective potentials of the different neutrino flavors are written as,

$$V_e = V_{\mathrm{CC}} + V_{\mathrm{NC}} \tag{1.21}$$

$$V_\mu = V_\tau = V_{\mathrm{NC}} \tag{1.22}$$

where NC represents the neutral current and CC represents the charged current interactions. They are expressed as

$$V_{\mathrm{CC}} = \sqrt{2} G_F n_e \tag{1.23}$$

$$V_{\mathrm{NC}} = -\frac{\sqrt{2}}{2} G_F n_n \tag{1.24}$$

where n_e is the effective potential of the number density of electrons in the material, n_n is the effective potential of the number density of neutrons in the material, and G_F is the Fermi coupling constant.

Considering two generations of neutrino oscillation at $\nu_e \leftrightarrow \nu_\mu$ for simplicity, the neutrino equation of state in vacuum is expressed as,

$$\frac{d}{dt} \begin{pmatrix} \nu_e \\ \nu_\mu \end{pmatrix} = -i \left[\frac{\Delta m^2}{4E} \begin{pmatrix} -\cos 2\theta & \sin 2\theta \\ \sin 2\theta & \cos 2\theta \end{pmatrix} \right] \begin{pmatrix} \nu_e \\ \nu_\mu \end{pmatrix} \tag{1.25}$$

Considering the additional contribution from the charged current interaction, it is expressed as,

$$\frac{d}{dt}\begin{pmatrix} \nu_e \\ \nu_\mu \end{pmatrix} = -i \left[\frac{\Delta m^2}{4E} \begin{pmatrix} -\cos2\theta & \sin2\theta \\ \sin2\theta & \cos2\theta \end{pmatrix} + \begin{pmatrix} V_{\text{CC}} & 0 \\ 0 & 0 \end{pmatrix} \right] \begin{pmatrix} \nu_e \\ \nu_\mu \end{pmatrix}$$

$$= -i \left[\begin{pmatrix} -\frac{\Delta m^2}{4E}\cos2\theta + \sqrt{2}G_F n_e & \frac{\Delta m^2}{4E}\sin2\theta \\ \frac{\Delta m^2}{4E}\sin2\theta & \frac{\Delta m^2}{4E}\cos2\theta \end{pmatrix} \right] \begin{pmatrix} \nu_e \\ \nu_\mu \end{pmatrix} \quad (1.26)$$

In order to diagonalize the matrix, the mixing matrix in matter U_M is defined as,

$$U_M = \begin{pmatrix} \cos\theta_M & \sin\theta_M \\ \sin\theta_M & \cos\theta_M \end{pmatrix} \quad (1.27)$$

where the effective mixing angel θ_M is given by

$$\tan2\theta_M = \frac{\frac{\Delta m^2}{2E}\sin2\theta}{\frac{\Delta m^2}{2E}\cos2\theta - \sqrt{2}G_F n_e} \quad (1.28)$$

Therefore, the oscillatory term in Eq 1.26 can be written as,

$$\frac{d}{dt}\begin{pmatrix} \nu_e \\ \nu_\mu \end{pmatrix} = -i \left[\frac{\Delta m_M^2}{4E} \begin{pmatrix} -\cos2\theta_M & \sin2\theta_M \\ \sin2\theta_M & \cos2\theta_M \end{pmatrix} \right] \begin{pmatrix} \nu_e \\ \nu_\mu \end{pmatrix} \quad (1.29)$$

where Δm_M^2 is the effective mixing mass difference,

$$\Delta m_M^2 = \Delta m^2 \sqrt{(\cos2\theta - A)^2 + \sin^2 2\theta} \quad (1.30)$$

where

$$A = \frac{2\sqrt{2}G_F n_e E}{\Delta m^2}, \quad (1.31)$$

The neutrino oscillation probability $P_M(\nu_e \leftrightarrow \nu_\mu)$ in matter is expressed as follows.

$$P_M(\nu_e \leftrightarrow \nu_\mu) = \sin^2 2\theta_M \sin^2\left(\frac{\Delta m_M^2}{4E}L\right) \quad (1.32)$$

It can be seen that the oscillation probability is determined by the density of matter passing through in addition to the neutrino energy and flight distance. If $A = \cos2\theta$, that is,

$$n_e^R = \frac{\Delta m^2}{2\sqrt{2}G_F E}\cos2\theta \quad (1.33)$$

the neutrino mixing is maximum. This effect is called the MSW(Mikheyev-Smirnov-Wolfenstein) effect [17].

11
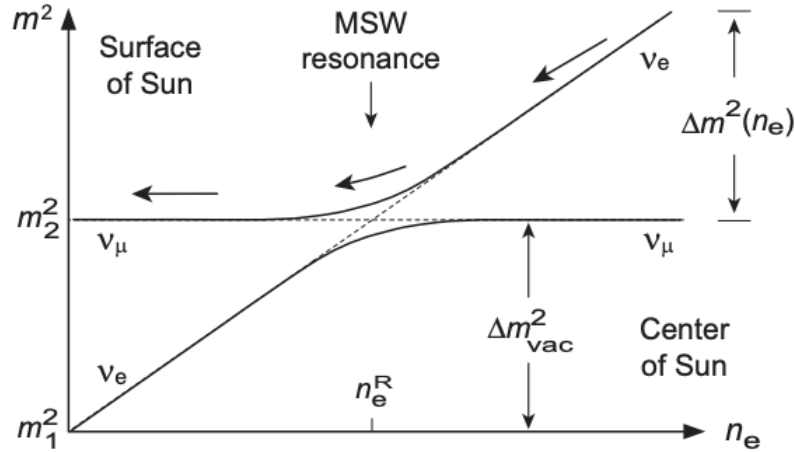
Figure 1.2: Electron density dependence of neutrino masses in the sun [6]. The vertical axis represents neutrino mass squared, the horizontal axis represents electron density.

MSW effect of solar neutrino

Solar neutrinos are produced near the high-density solar center and are therefore affected by the MSW effect in the process of reaching the surface of the sun.

Figure 1.2 shows the dependence of neutrino mass on electron density in the Sun. The flavors of neutrinos are mixed, so they transition along the solid line in the figure, keeping $\Delta m_M^2 \neq 0$. Thus, ν_e produced near the dense solar center changes to ν_μ when it comes to the solar surface ($n_e = 0$) due to the MSW effect.

1.3 Diffuse Supernova Neutrino Background (DSNB)

1.3.1 Supernova explosion

A supernova explosion is an explosion that occurs when a massive star or white dwarf reaches the end of its life or exceeds a certain amount of mass due to interaction with another dwarf star. After the explosion, the energy ($\sim 10^{51}$ erg) spreads throughout the universe and is the basis for the evolution of galaxies, planets, and other stars. Therefore, supernova events are of great interest to astrophysics.
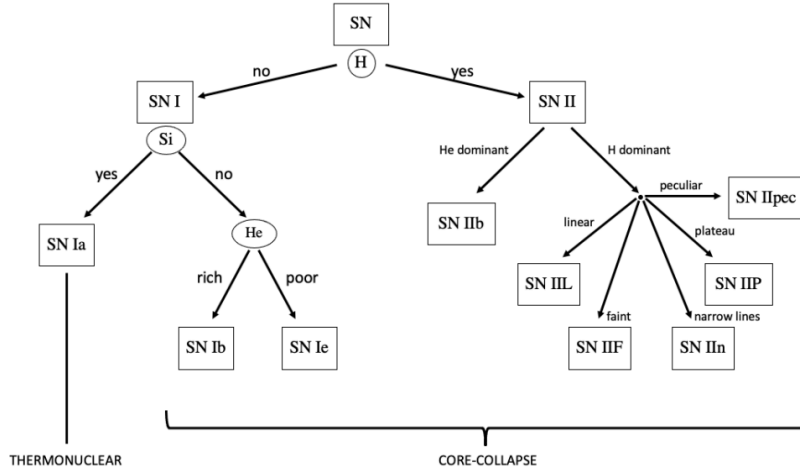
Figure 1.3: The supernova classification [18].

Supernova explosions are classified according to the emission lines in the spectrum as shown in Figure 1.3. Type Ia supernova explosion is caused by the reaction of thermonuclear fusion. Neutrinos emitted by Type Ia supernova explosions have energies of 10^{49} erg or less. On the other hand, type Ib, Ic and II supernova explosions are caused by core collapse. Neutrinos emitted by them have energies of $\sim 10^{53}$ erg.

1.3.2 Supernova neutrino

Supernova neutrinos refer mainly to neutrinos produced by supernova explosions caused by core collapse (Type Ib, Ic and II). How neutrinos are emitted from these supernova explosions is described below.

1. Start of gravitational collapse
   The iron core in the star starts to collapse and the density and temperature increase. Accompanying this, electron capture of elements occurs and neutrinos are produced.

$$e^- + A(N, Z) \rightarrow \nu_e + A(N + 1, Z - 1) \tag{1.34}$$
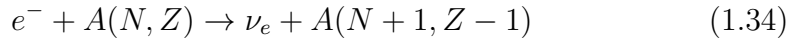
2. Production of neutrino sphere
   When the core becomes ultra-dense around $10^{11} - 10^{12}$ g/cm^3, a region (neutrino sphere) is created in the center of the star where neutrinos are trapped and can only gradually escape.

13

3. Shock wave
   When the core density reaches the nucleon density, neutron degeneracy pressure stops contraction. However, since material falls from the outer core at supersonic speed, a shock wave is generated at the interface between the inner core and the outer core.

4. Neutronization burst
   Electron neutrinos are produced by the capture of surrounding electrons by protons produced during shock wave propagation. While the shock wave is propagating inside the neutrino sphere, the electron neutrinos cannot escape, but when the shock wave reaches the outside of the neutrino sphere, the electron neutrinos can fly out. This is called ν_e neutronization burst. Also, a Proto Neutron Star (PNS) is formed inside the star.

5. Cooling of the PNS
   After the shock wave has passed through, the nuclei, electrons and positrons produced fall into the PNS. The various flavor neutrinos are produced at this time. The neutrinos heat the material behind the shock wave, reviving the stalled shock wave. The PNS is also cooled because of the heat brought out by the neutrinos.

6. Supernova explosion
   When the shock wave reaches the surface of the star, a supernova explosion occurs, blowing away all the outer layers.

Neutrinos of different flavors evolve differently, giving the following energy hierarchy.

$$\langle E_{\nu_e} \rangle < \langle E_{\nu_{\bar{e}}} \rangle < \langle E_{\nu_x} \rangle \tag{1.35}$$

where $x = \mu, \tau$. Figure1.4 shows the time distribution of neutrino energy and luminosity obtained by simulation. ν_x in the figure represents $\nu_x = (\nu_\mu + \bar{\nu_\mu} + \nu_\tau + \bar{\nu_\tau})/4$. These energies range from 10 MeV to around 20 MeV.

1.3.3 Diffuse Supernova Neutrino Background

The Diffuse Supernova Neutrino Background (DSNB) is the overall neutrino flux of all core-collapse Supernovae that happened in the history of universe. There are DSNB in the universe from $\sim 10^{17}$ supernova explosions from the Big Bang to the present.

The differential DSNB flux on Earth, taking into account also redshift effects, is given by,

$$\frac{d\Phi}{dE_\nu} = c \int_0^\infty R_{\mathrm{SN}}(z)(1+Z)\frac{dN_\nu[E_\nu(1+z)]}{dE_\nu}\frac{dt}{dz}dz \tag{1.36}$$
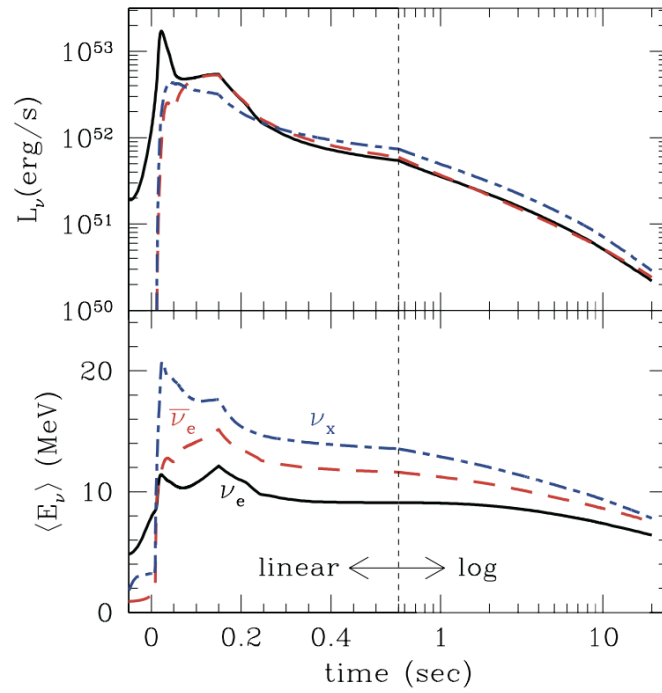
Figure 1.4: Time distribution of supernova neutrino energy and luminosity [19]

where $R_{\mathrm{SN}}(z)$ is the Supernova rate at redshift z, E_ν is the neutrino energy received, dN_ν/dE_ν is the number spectrum emitted by the explosion where the neutrino was emitted at a higher energy $E_\nu(1+z)$. dz/dt is the relation between cosmic time t and redshift z given by,

$$\frac{dz}{dt} = -H_0(1+z)\sqrt{\Omega_\Lambda + \Omega_m(1+z)^3} \qquad (1.37)$$

where H_0 is the Hubble constant and Ω is the cosmological parameters.

Many theoretical models have been proposed to predict the DSNB flux. Figure 1.5 shows the predicted energy distribution of the $\bar{\nu}_e$ flux. Various searches for supernova background neutrinos have been conducted so far, but they have not yet been discovered. In Super-Kamiokande, gadolinium has been loaded to improve the detection capability of DSNB and DSNB event rate is expected to be several times per year [20]. The details are explained in Section 2.5. If we can observe the supernova background neutrinos and compare their energy spectra with theoretical predictions, we will be able to understand the mechanism and rate of supernova explosions, as well as the initial mass distribution of stars.
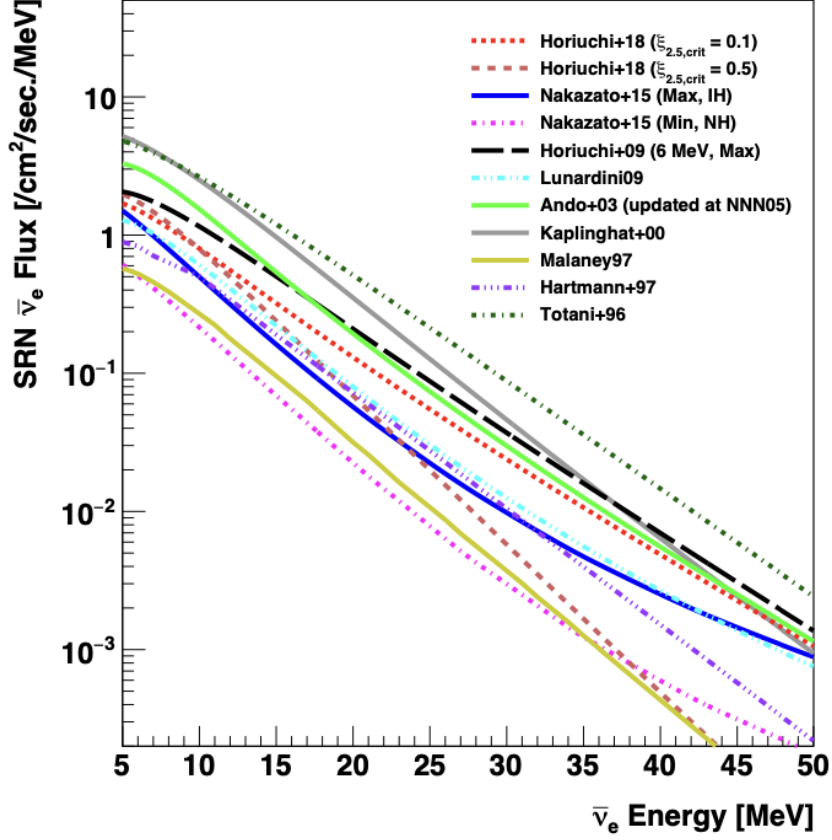
Figure 1.5: DSNB $\bar{\nu}_e$ flux predictions from various theoretical models [20] The color of each line represents the difference in theoretical models.(red dotted line and brown dotted line: Horiuchi +18 model [21], blue line and pink dotted line: Nakazato +15 model [22], light blue dotted line: Lunardini +09 model [23], green line: Ando +03 model [24], Gray line: Kaplinghat +00 model [25], ocher line: Malaney +97 model [26], purple dotted line: Hartmann +97 model [27], dark green dotted line: Totani +96 model [28])

Chapter 2

Super-Kamiokande experiment

2.1 The Super-Kamiokande detector

Super-Kamiokande detector (SK detector) [29] is a 50 kton water Cherenkov detector. It is placed 1,000 m underground of Mt. Ikenoyama, in the Kamioka mine, Hida City, Gifu Prefecture, Japan. SK detector is a cylindrical tank with 39.3 m in diameter and 41.4 m in height as shown in Figure 2.1. Previously, pure water was used as the detector medium. In 2020, gadolinium with a concentration of 0.01% was introduced. The concentration was increased to about 0.03% in 2022.

2.1.1 Cherenkov light

Cherenkov light is emitted when a charged particle moves faster than the speed of light in a medium. It is emitted in a conical shape at an opening angle θ_c with respect to to the direction of movement of the charged particle as shown in Figure 2.2. The opening angle θ_c between the charged particle and Cherenkov light is given by

$$\cos\theta_c = \frac{1}{n\beta}, \tag{2.1}$$

where n is the refractive index of the medium and $\beta = v/c$ is the speed of the charged particle. When the medium is water, the refractive index is $n \sim 1.34$. Similarly for gadolinium water, $n \sim 1.34$. The opening angle is around 42° for particles travelling at $\beta \sim 1$ in water. The momentum threshold for the Cherenkov radiation is

$$p_{\text{thresh}} = \frac{mc}{\sqrt{n^2 - 1}}. \tag{2.2}$$

The threshold for electron and muon are summarized in Table 2.1
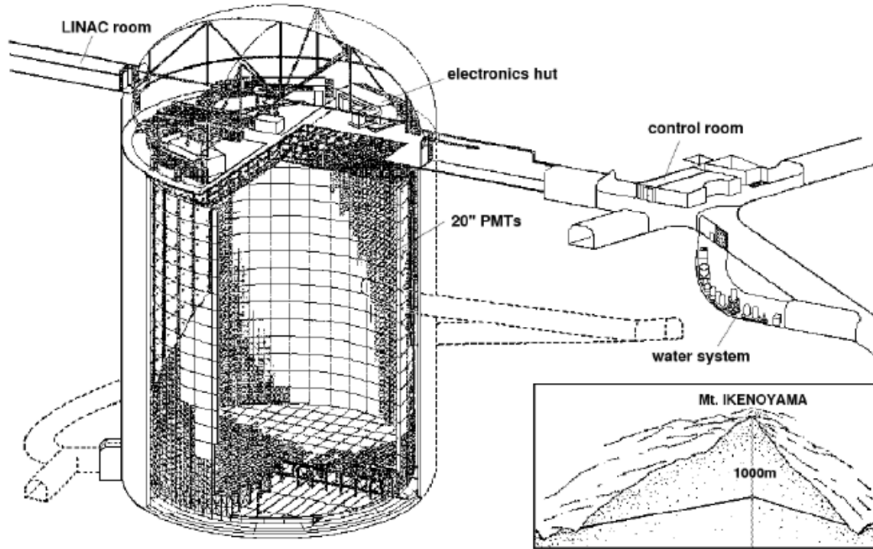
Figure 2.1: SK detector [30]

The number of Cherenkov photons dN emitted by a particle with charge 1e per flight distance dx is given by

$$\frac{\mathrm{d}^2 N}{\mathrm{d}\lambda \mathrm{d}x} = \frac{2\pi\alpha}{\lambda^2}(1 - \frac{1}{n^2\beta^2}),\tag{2.3}$$

where λ is the wavelength of emitted light and α is the fine structure constant $(= \frac{1}{137})$.

When an electron travels 1 cm, in the PMT's sensitivity range of light wavelengths of 300-600 nm, the number of Cherenkov photons N is given by

$$N = \int_0^{1\mathrm{cm}} \mathrm{d}x \int_{300\mathrm{nm}}^{1600\mathrm{nm}} \mathrm{d}\lambda \frac{2\pi\alpha}{\lambda^2}(1 - \frac{1}{n^2\beta^2}) \simeq 340.\tag{2.4}$$

Gamma rays can also be detected by Compton-scattered electrons and by pair-produced electrons and positrons.

Table 2.1: The summary of Cherenkov momentum thresholds in water.

particle	mass [MeV/c^2]	p_{thresh}[MeV/c]
electron	0.511	0.572
muon	105.66	158.73
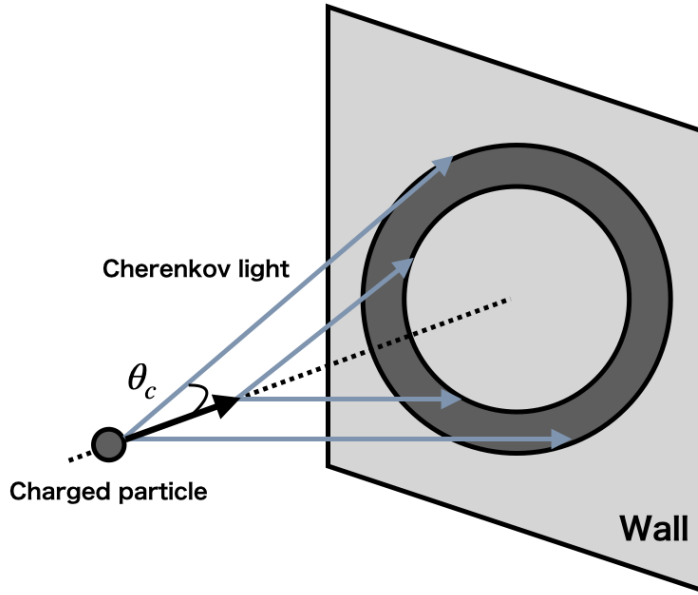
Figure 2.2: Outline drawing of Cherenkov light

2.1.2   Inner detector and Outer detector

The Super-Kamiokande detector is divided into two regions: the Inner Detector (ID) and the Outer Detector (OD). (Figure 2.3)

ID is a cylindrical detector with diameter of 33.8 m and height of 36.3 m. 20-inch PMTs are installed on the inner wall facing inside. They detect the Cherenkov light emitted by charged particles within the volume of 32.6 kton and is responsible for reconstructing the position and energy of the event. There are currently a total of 11,129 PMTs, covering approximately 40% of the surface area of the ID. The surfaces without the PMTs are covered with the black sheets to prevent light reflection on the wall surfaces.

OD is the region outside the ID, covering with the thickness of 2.05 m on the top and bottom surfaces and 2.2 m on the sides. 1,885 8-inch PMTs are installed facing outwards on the walls. The OD is responsible for identifying cosmic ray muons and shielding rock-derived neutrons and gamma rays. The surfaces except the PMTs are covered with the white reflective sheet called a Tyvek sheet in order to improve the light collection efficiency of the PMTs of the OD and to prevent light generated in the OD from entering the ID.

The coordinate of the SK detector is taken as shown in Figure 2.4. The x and y axes are taken in the horizontal direction and the z axis in the vertical direction. The zero point of each axis is the black dot in the figure.
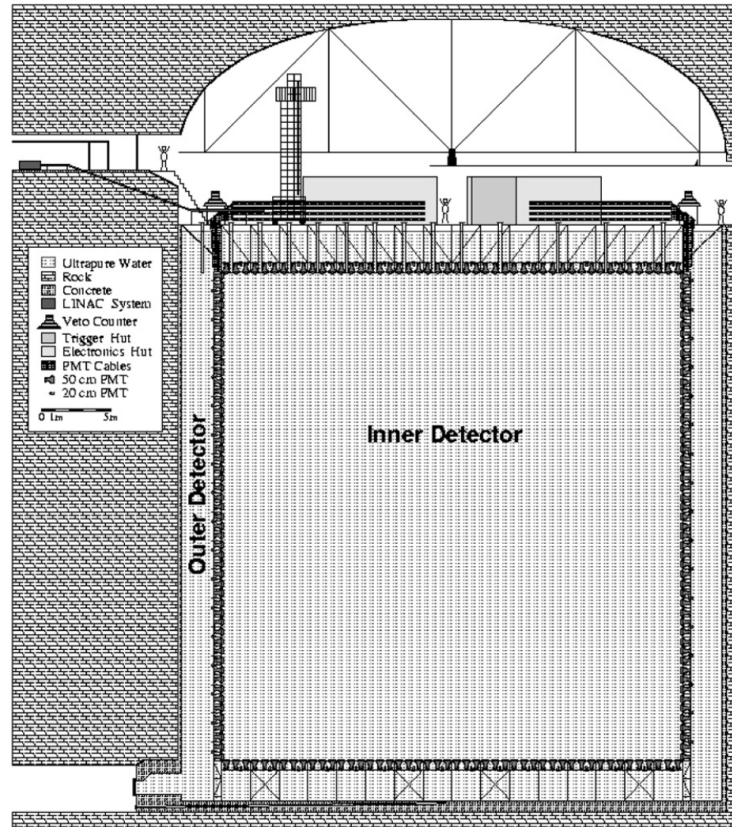
Figure 2.3: The cross-section of SK detector [29]
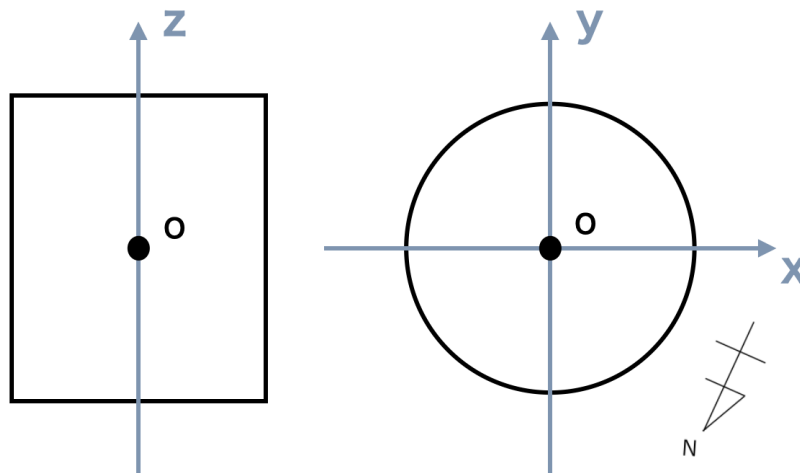
Figure 2.4: Coordinate setting of SK detector.
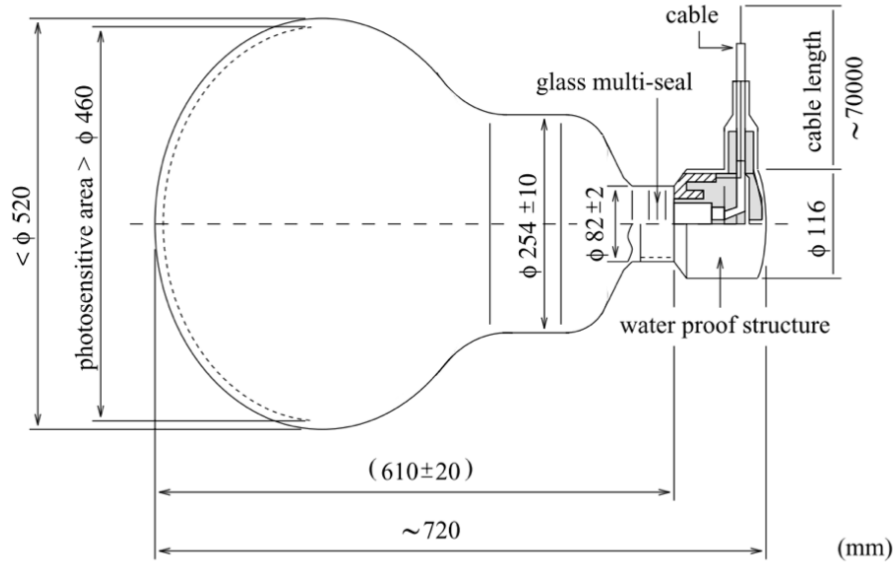
Figure 2.5: Schematic view of a 20-inch ID PMT [29]

2.1.3 Photo Multiplayer Tube (PMT)

20-inch PMTs developed by Hamamatsu Photonics and University of Tokyo are used for Inner Detector [29]. (Figure 2.5) The performance of the 20-inch ID PMTs is shown in Table 2.2. The photocathodes of the PMTs are made by the bialkali (Sb-K-Bs) and the sensitive wavelength range is $280 \sim 600$ nm. This wavelength range is suitable for detecting of Cherenkov light. The quantum efficiency is $\sim 22\%$ at wavelengths $360 \sim 400$ nm, as shown in Figure 2.6.

There is an average geomagnetic field of 450 mG around the SK detector. In order to prevent the influence of this magnetic field, Helmholtz coils are installed in the horizontal and vertical directions around the detector. Thanks to this, the magnitude of the magnetic field inside the detector is suppressed to an average of 32 mG, and the effect of geomagnetism on the collection efficiency of the PMTs is estimated to be $1 \sim 2\%$.

In the wake of the November 2001 explosion, the PMTs are covered with the acrylic and the fiber reinforced plastic (FRP) covers to prevent the chain failure.

2.2 Data acquisition systems

QBEE

All PMT signals are read out by a front-end electronics called QBEE (QTC-

Table 2.2: Typical performance of the 20-inch ID PMTs. [29]

Model number	R3600
Photocathode material	Bialkali (Sb-K-Bs)
Photoelectron collection efficiency	70%
Quantum efficiency	$\sim 22\%$ ($\lambda : 360 - 400$nm)
Dynode structure	11-stage Venetian blind type
Gain	10^7 at 2000V
Dark current	200 nA at 10^7 gain
Dark rate	3 kHz at 10^7 gain
Transit time	90 ns at 10^7 gain
Transit time spread	2.2 ns (1σ)
Weight	13 kg
Pressure resistance	6 kg/cm^2
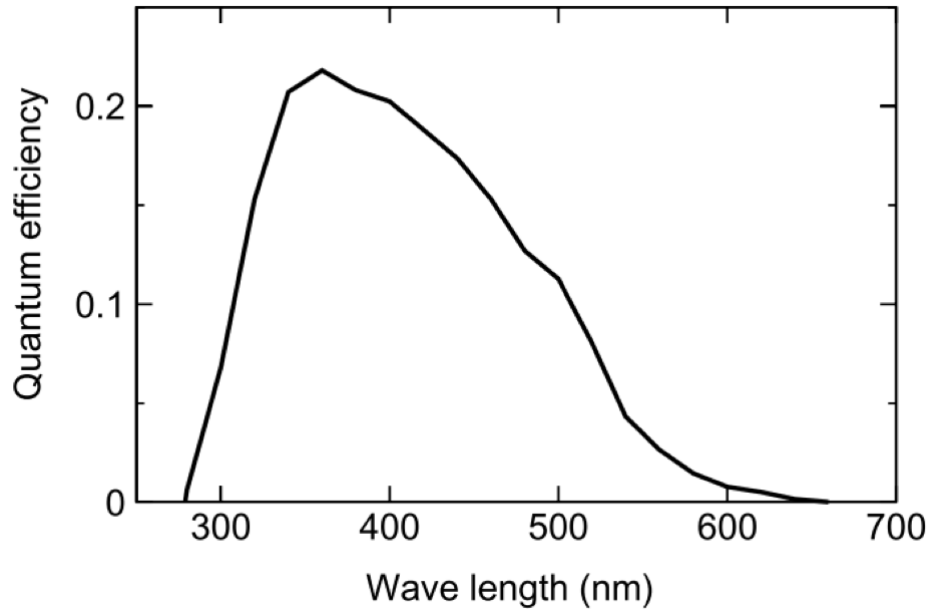
Figure 2.6: Quantum efficiency of PMT as a function of wavelength [29]
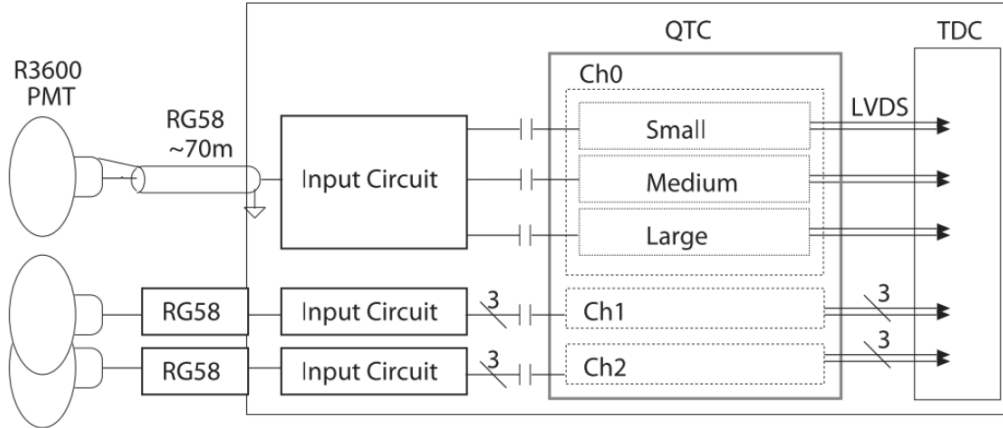
Figure 2.7: QBEE system [31]

Based Electronics with Ethernet). The diagram of QBEE is shown in Figure 2.7. When the amplitude of the PMT signal exceeds a value corresponding to 0.25 photoelectron(p.e.), QTC (charge to time converter) calculates the integrated charge over 400ns and a square wave with a time width proportional to the amount of charge is generated. The rising edge of the square wave corresponds to the PMT hit time. By digitizing this square wave with TDC (time-to-digital converter), the PMT hit time and integrated charge information can be read out. The signal information stored in TDC is read out by FPGA (Field Programmable Gate Array), processed, and recorded.

Software trigger

The above recorded data are software-triggered to extract events. When the number of PMT hits in 200ns (N_{200}) exceeds a certain threshold, each software trigger is issued and the surrounding hit information is stored. Those triggers are classified as SLE (Super Low Energy), LE (Low Energy), HE (High Energy), SHE (Super High Energy), OD (Outer Detector). The thresholds and the time window of these triggers are summarized in table 2.3. In addition, when SHE trigger is issued, AFT trigger which is the $500\mu s$ trigger from $[+5, +535]\mu s$ is issued following SHE trigger. The AFT trigger is the trigger designed for searching for DSNB. Previously, it was issued when SHE trigger was issued but OD was not issued, but from June 2020, for SK-Gd, AFT trigger is also issued when OD trigger is issued at the same time as SHE trigger to capture the signal of neutron capture by gadolinium generated by the spallation reaction of cosmic muon.

Table 2.3: The summary of the software triggers

Trigger	N_{200} threshold	time window [μs]
SLE	34	[-0.5, +1.0]
LE	49	[-5, +35]
HE	52	[-5, +35]
SHE	60	[-5, +35]
OD	22	[-5, +35]

2.3 Detector performance per data acquisition period

There have been seven phases for data taking at Super-Kamiokande. Each phase is explained below, and the detector condition of each phase is summerized in Table 2.4.

SK-I

The first data taking period from the start of observations in April 1996 to July 2001.

In July 2001, work was carried out to replace the faulty PMT. However, in November 2001, after the replacement work was completed, the PMT implosion accident occurred while filling water into the detector. The accident resulted in the loss of 6,777 PMTs in the inner tank and 1,100 PMTs in the outer detector.

SK-II

After the PMT implosion accident, the experiment was resumed from October 2002 with 5,128 PMTs in the ID. Data taking was continued until October 2005. From SK-II, the PMT is equipped with an anti-shock case to prevent cascading implosion to the PMT.

SK-III

In June 2006, the new PMTs were installed to replace those lost in the crash. As a result of this installation work, the number of the PMTs in the inner tank increased to 11,129. Data taking was carried out from July 2006 to August 2008.

SK-IV

Data acquisition period from September 2008 to May 2018.In August 2008 the data acquisition electronics were upgraded from ATM to QBEE.

SK-V

For the SK-Gd experiment, waterproofing reinforcement work, improvement of piping inside the tank and replacement of faulty photomultiplier tubes, etc. was carried out from July 2018 to January 2019. Data taking period from the end of January 2019 after the completion of the repair work to June 2020 when the gadolinium addition work started.

SK-VI

From July 2020, 13 ton of $Gd_2(SO_4)_3 \cdot 8H_2O$ was introduced into the detector. This loading was completed in August 2020 and SK-VI started. As a result, the mass concentration of Gd is approximately 0.01% and the neutron capture efficiency is approximately 50%.

SK-VII

From June 2022, the additional 27 ton of $Gd_2(SO_4)_3 \cdot 8H_2O$ was introduced into the detector. This loading was completed in July 2022 and SK-VII started. As a result, the mass concentration of Gd is approximately 0.03% and the neutron capture efficiency is approximately 75 %.

Gd-loading of SK-VI and SK-VII is explained in detail in section 2.4.

Table 2.4: Detector performance per data acquisition period

Phase	Period	ID PMT	Gd concentration	coverage	electronics
SK-I	1996/04 – 2001/07	11,146	0%	40%	ATM
SK-II	2002/10 – 2005/10	5,182	0%	19%	ATM
SK-III	2006/07 – 2008/08	11,129	0%	40%	ATM
SK-IV	2008/08 – 2018/05	11,129	0%	40%	QBEE
SK-V	2019/01 – 2020/06	11,129	0%	40%	QBEE
SK-VI	2020/08 – 2022/06	11,129	0.01%	40%	QBEE
SK-VII	2022/06 –	11,129	0.03%	40%	QBEE

2.4 Super-Kamiokande with Gd

2.4.1 Gadolinium

In ultrapure water without Gd, neutrons are captured by hydrogen and a single 2.2 MeV gamma ray is emitted. This signal is difficult to distinguish from background events due to its low energy, and the neutron detection efficiency was 20%.

Gadolinium (Gd) is a rare earth element with atomic number 64. ^{157}Gd has the largest thermal neutron capture cross-section among natural elements. The thermal neutron capture cross-sections for different isotopes of gadolinium are shown in Table 2.5. When ^{157}Gd (^{155}Gd) captures a neutron, it becomes the excited state of ^{158}Gd(^{156}Gd). Then ^{158}Gd(^{156}Gd) emits gamma rays which energies are 7.9 MeV for ^{157}Gd and 8.4 MeV for ^{155}Gd in total as it transitions to the ground state of ^{158}Gd(^{156}Gd). The proportion of thermal neutrons that are captured by gadolinium as a function of the mass concentration of gadolinium dissolved in pure water is as shown in Figure 2.8. In the 2020 Gd-loading, at the mass concentration of 0.011%, the proportion was 50%, and in the additional Gd-loading in 2022, at the mass concentration of 0.03%, the proportion was about 75%. SK collaboration has set a goal of 0.1% mass concentration in the end, and the proportion at that time will be about 90%.

Table 2.5: Thermal neutron capture cross section for each gadolinium isotope

Isotope	Natural abundance ratio [%]	Cross section [b]
^{152}Gd	0.20	740
^{154}Gd	2.18	85.8
^{155}Gd	14.80	611000
^{156}Gd	20.47	1.81
^{157}Gd	15.65	254000
^{158}Gd	24.84	2.22
^{160}Gd	21.86	1.42

2.4.2 Recirculation system for Gd-loaded water

The loading of gadolinium into the SK tank is done by dissolving the $Gd_2(SO_4)_3 \cdot 8H_2O$ powder through the SK water purification system. The conventional water purifiers have ion-exchange resins, where ions are removed, but in SK-Gd, it is necessary to circulate water while retaining gadolinium ions (Gd^{3+}) and sulfate ions (SO_4^{2-}). Therefore, a new circulation system was developed to remove ions other than gadolinium ions and sulfate ions. The main purification steps are shown below and the SK-Gd water system is shown in Figure 2.9.

Purification system

1. UV total organic carbon reduction lamp (TOC lamp)
   Irradiate ultraviolet rays with a wavelength of 184.9 nm to oxidize and decompose organic matter. It also sterilizes bacteria by irradiating ultraviolet rays with a wavelength of 253.7 nm.
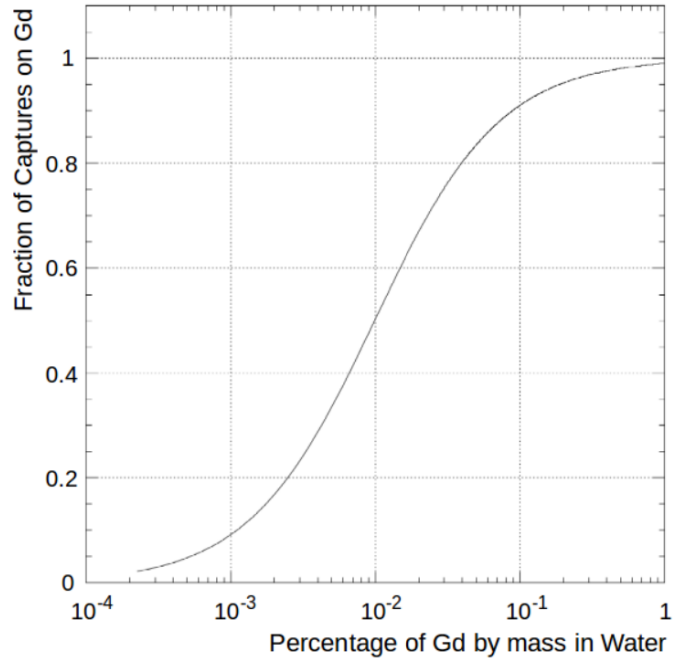
Figure 2.8: The proportion of thermal neutrons that are captured by gadolinium

2. Heat exchanger (HE)
   The temperature of the water in the detector rises due to the heat generated by the circulation pump and high-voltage PMT. This temperature increase causes dark noise, bacterial growth, and water convection. In order to prevent them, three heat exchangers are used for one cycle of water circulation, and water temperature is adjusted to about 13 degrees.

3. Strongly acidic cation exchange resin (2400L) ("C-Ex Resin" in Fig 2.9)
   The acidic cation resin is inert to gadolinium ions. Ions other than gadolinium ions are removed.

4. Strongly basic anion exchange resin (4600L) ("A-Ex Resin" in Fig 2.9)
   The basic cation resin is inert to gadolinium sulfate ions. Negatively charged impurities are removed.

5. 1 μm mesh filter
   Remove dust of 1μm or more and radioactive materials attached to it.

6. UV sterilizer
   Ultraviolet radiation is irradiated to kill bacteria.

7. UF modules

Remove particles smaller than 1 μm using filtration.

8. Membrane degasifier (MD)
   Remove Rn dissolved in the water.

The two sets of HE, C-EX, A-EX, middle filter (1 μm), and UV sterilizer are connected in parallel. Each has a supply of 60 ton/hour, making it possible to supply a total of 120 ton/hour Gadolinium sulfate.

The water supplied to SK detector is purified groundwater in the Kamioka Mine (Appendix A). It is important to remove Radon ^{222}Rn, which is a radioactive substance dissolved in water. Radon becomes a background for analysis near the threshold (3.5 MeV) in solar neutrino observations because radon's daughter nucleus, ^{214}Bi, emits 3.26 MeV electron through beta decay. Through the above purification process, the purified ultrapure water has a radon concentration of ~ 1.7mBq/m^3.

In addition, by the water circulating system in which purified water is put in from the bottom and withdrawn from the top, there is a problem of top bottom asymmetry in water quality with higher water transmission at the bottom of the detector than at the top.

Dissolving system

1. The weighing hopper
   The $Gd_2(SO_4)_3 \cdot 8H_2O$ powder is weighed.

2. The circle feeder
   The $Gd_2(SO_4)_3 \cdot 8H_2O$ powder is delivered in regulated quantities via the circle feeder.

3. The solvent tank a fraction of the SK water being continuously recirculated is fed.

4. The shear blender and the dissolving tank
   $Gd_2(SO_4)_3 \cdot 8H_2O$ powder is dissolved in water from the solvent tank.

5. The solution tank
   The resulting solution is sent.

Pre-treatment system

1. Ultra-filters (3 μm, 1 μm, 0.2 μm)
   It remove very small dust.

2. UV total organic carbon reduction lamp (TOC lamp)

3. C-EX resin and A-EX resin These are cation exchange resin inert to Gd^{+3}, anion exchange resin inert to SO_4^{2-}.
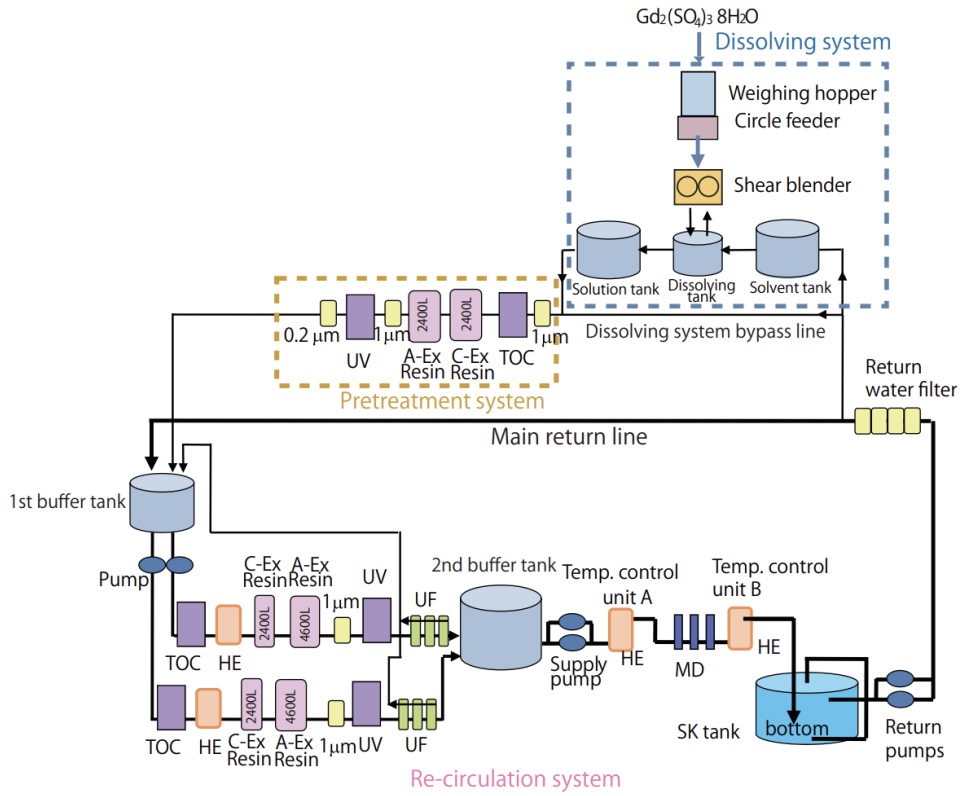
Figure 2.9: Schematic diagram of SK-Gd water system [32]

4. UV sterilizer
   Bacteria are removed.

2.4.3   Gadolinium loading

The first Gd-loading [32] was carried out between July 14 and August 17 2020, with 13.2 ton of $Gd_2(SO_4)_3 \cdot 8H_2O$ powder dissolved via the system described above. At this loading, the mass concentration of $Gd_2(SO_4)_3 \cdot 8H_2O$ was 0.026%, which corresponds to the mass concentration of Gd of 0.011%. The time evolution of the mass of the dissolved $Gd_2(SO_4)_3 \cdot 8H_2O$ powder is shown in Figure 2.10. It shows that $Gd_2(SO_4)_3 \cdot 8H_2O$ was stably loaded up to the target of 13.2 ton. Water with dissolved $Gd_2(SO_4)_3 \cdot 8H_2O$ is introduced from the bottom of the detector. At that time, by making the temperature 0.35 degrees lower than the water in the detector, the water in the tank was replaced with gadolinium water from the bottom as shown in Figure 2.11. The state of Gd-loading can be confirmed by observing
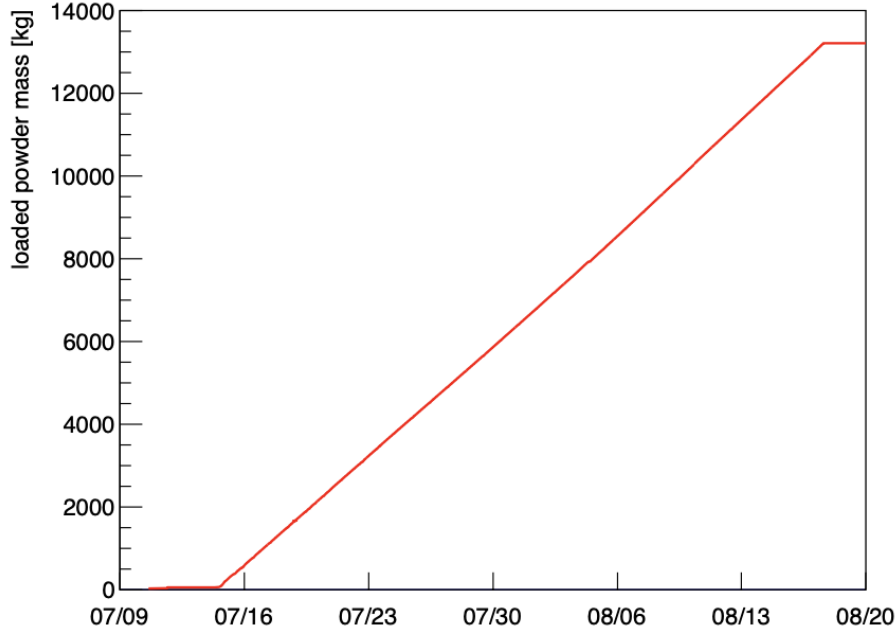
Figure 2.10: The time transition of the mass of the dissolved $Gd_2(SO_4)_3 \cdot 8H_2O$ powder in 2020

neutrons generated by the spallation reaction of cosmic muons. Figure 2.12 shows the event distribution for each week from July 9, 2020 to August 23, 2020. We confirmed that the gadolinium sulphate solution was gradually introduced from the bottom of the tank and the concentration was constant throughout the tank.

Additional Gd-loading was carried out between 1 June 2022 and 4 July 2020. In this loading, 27.3 tons of $Gd_2(SO_4)_3 \cdot 8H_2O$ powder was dissolved, resulting in the $Gd_2(SO_4)_3 \cdot 8H_2O$ mass concentration of 0.078% and the Gd concentration of 0.033%. The time evolution of the mass of the dissolved gadolinium powder is shown in Figure 2.13. It can be seen that this Gd-loading was also performed stably. In this study, we observed Gd-loading by using the number of events in which spallation neutrons from cosmic muon are captured by gadolinium and the time constant until spallation neutrons are captured by gadolinium. The results are explained in Section 7.2.
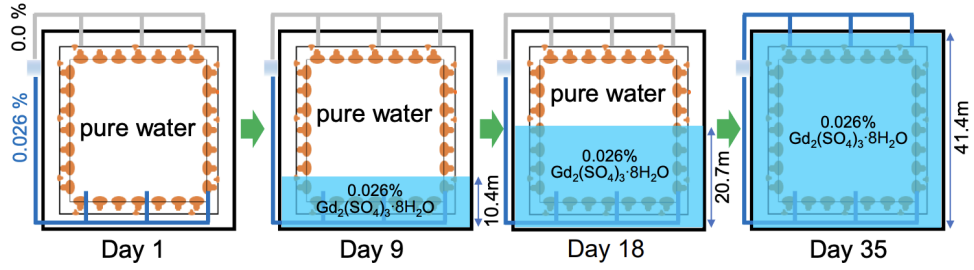
Figure 2.11: Gadolinium loading scheme
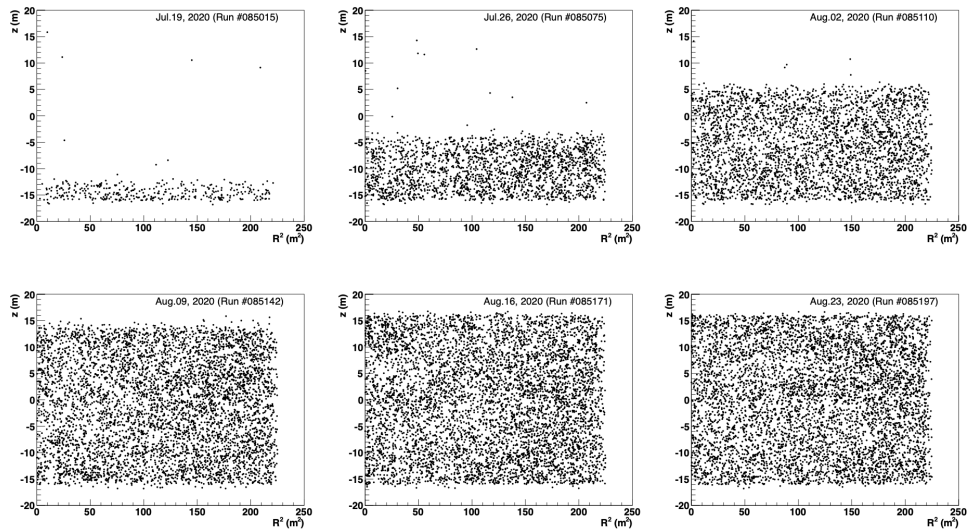
Figure 2.12: Event distribution of cosmic muon derived neutrons captured by gadolinium. The horizontal axis represents the square of the radius of the reconstructed vertex position, and the vertical axis represents the height.
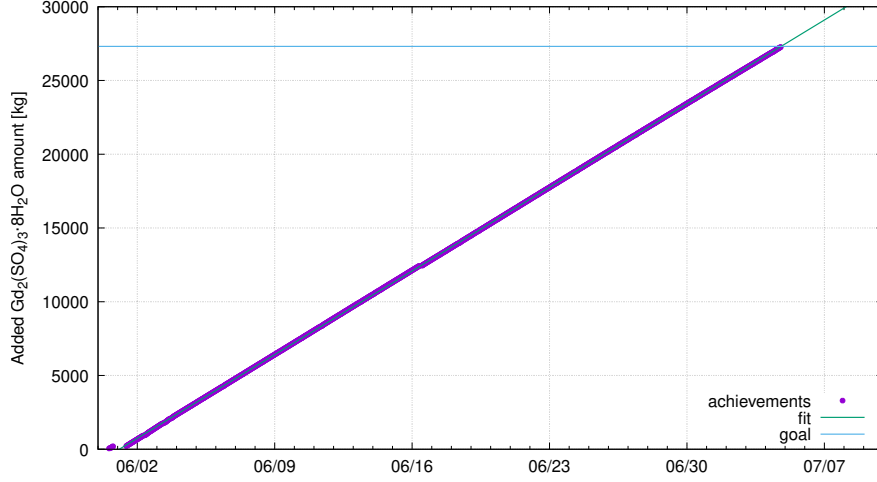
Figure 2.13: The time transition of the mass of the dissolved $Gd_2(SO_4)_3 \cdot 8H_2O$ powder in 2022

2.5 Search for DSNB in SK-Gd

2.5.1 DSNB signal

The search for DSNB by the Super-Kamiokande has provided the world's most stringent upper limit for the flux of DSNB, but it has yet to be discovered. This is because the flux of DSNB is $O(1)\mathrm{cm}^{-1}\mathrm{s}^{-1}$, which is very small, and even with the effective volume of Super-Kamiokande (22.5 tons), only 0.8 to 5 events occur per year.

In Super-Kamiokande, the search for supernova background neutrinos is carried out using inverse beta decay reactions (Eq. (2.5)) between electron antineutrino and proton in the water.

$$\bar{\nu}_e + p \rightarrow e^+ + n \tag{2.5}$$

The search is carried out in the energy range of 10-30 MeV, where the influence of reactor neutrinos and atmospheric neutrinos is relatively small (Figure 2.14).

When the inverse beta reaction occurs in pure water, positron and neutron are produced. Firstly positron emits Cherenkov light and it is detected by PMTs. Then neutron is captured by hydrogen with a time constant of about 200μs. At that time, gamma ray with an energy of 2.2 MeV are emitted. Electrons are generated by electromagnetic interaction in water and emit Cherenkov light, which is detected by PMTs. In the search for DSNB, delayed coincidence measurement is used with two such signals, the prompt signal from the positron and the delayed signal from the gamma rays emitted when the neutron is captured by hydrogen.
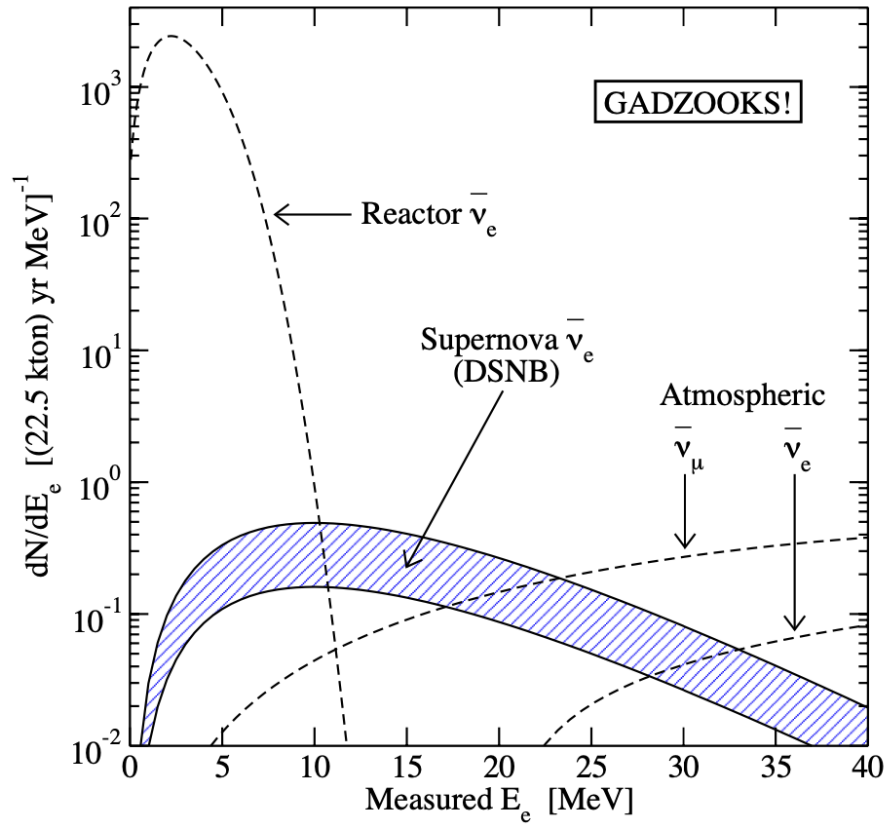
Figure 2.14: Fluxes of DSNB (blue diagonal line) and background event neutrinos expected at Super-Kamiokande [33]. The flux of DSNB depends on the model and has a range.
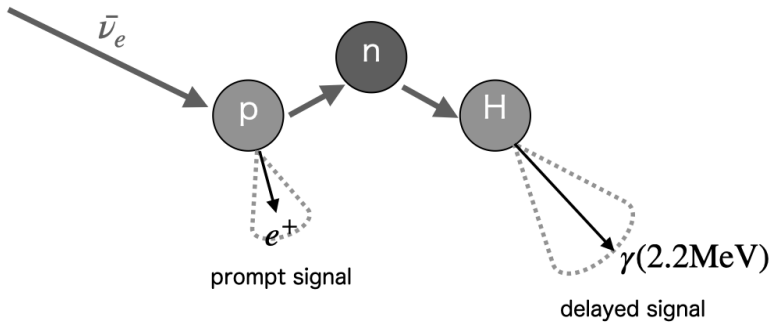
Figure 2.15: The signals from DSNB (electron antineutrino) observed in pure water

The schematic diagram of this reaction is shown in Figure 2.15. However, it is difficult to detect neutron capture events by hydrogen. This is because that, firstly the neutron capture cross-section of hydrogen atom is as small as 0.3 barn, secondly the time taken to capture a neutron is as long as 200 μs, thirdly the gamma ray energy emitted is as low as 2.2 MeV, making it difficult to distinguish from low energy background events. Gadolinium was introduced to overcome these weaknesses.

SK-Gd, by introducing gadolinium, improves the neutron detection efficiency and has the purpose of searching for DSNB with high statistics and low background. In SK-Gd, the search for DSNB is performed by delayed coincidence measurement using the prompt signal from positron and the delayed signal from several gamma rays with a total energy of about 8 MeV emitted by the neutron captured by Gd. The schematic diagram of this reaction is shown in Figure 2.16. The 8 MeV energy can be separated from low energy background events and the signal is easy to tag. As described in the previous chapter, the neutron capture cross-section of Gd is 60,900 barn for ^{155}Gd and 254,000 barn for ^{157}Gd, approximately 200,000 and 1,000,000 times that of hydrogen atoms, and the neutron detection efficiency is estimated to reach about 90% at a Gd concentration of 0.1% (Figure 2.8).

2.5.2 Backgrounds for DSNB

The observed SK-IV data and expected background spectra are shown in Figure 2.17. As the figure shows, there are three main backgrounds in DSNB search below 20 MeV: Atmospheric neutrinos (NCQE), Atmospheric neutrinos (non-NCQE), and spallation ^{9}Li.

Atmospheric neutrinos (NCQE)
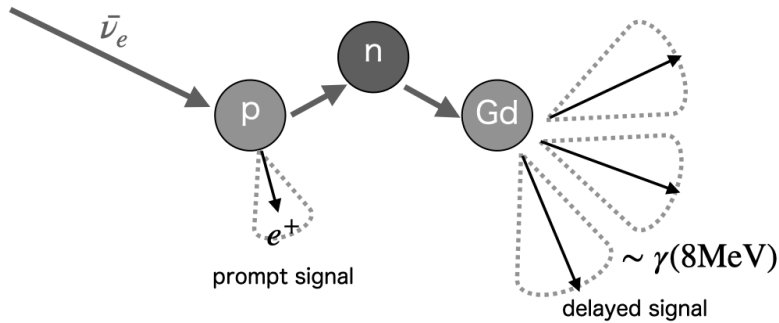
Figure 2.16: The signals from DSNB (electron antineutrino) observed if Gd exist

In the energy region below 16 MeV, Neutral Current Quasi-Elastic scattering (NCQE) of atmospheric neutrinos and oxygen atoms ^{16}O in water dominate as background events. In this event, the gamma rays emitted when excited oxygen nuclei are de-excited are the prompt signal, and neutrons with energies of tens to hundreds of MeV, which are kicked out by atmospheric neutrino, are detected as the delayed signal. Nucleons ejected from oxygen atom have high energy and collide with surrounding oxygen atom to emit secondary gamma rays and neutrons. Figure 2.18 shows the flow of this interaction. In the event where multiple neutrons are emitted, multiple neutron capture signals are detected after the prompt signal by gamma ray. On the other hand, since only one neutron is generated from inverse beta decay by DSNB, it can be distinguished from NCQE in which multiple neutron signals are detected. Therefore, it is estimated that the background of atmospheric neutrinos by NCQE is reduced to 1/3 with neutron tagging with Gd.

Atmospheric neutrinos (non-NCQE)

Charged-current quasielastic (CCQE) interaction and pion production dominate at high energy region above 20 MeV. Cherenkov light from electrons produced by the decay of muons and pions is detected in this reaction. So, the reconstructed energy follows the Michel energy spectrum from about 15 to 50 MeV. Atmospheric neutrino events are simulated using the HKKM 2011 flux [35].

Cosimc ray muon spallation

SK is exposed to cosmic ray muons at a rate of $\sim$2 Hz. Muons produce electromagnetic and hadron showers in water. Spallation of oxygen nuclei induced by the muons or by secondary particles produce radioactive isotopes. Those decays could be misidentified as IBD events in the DSNB search and
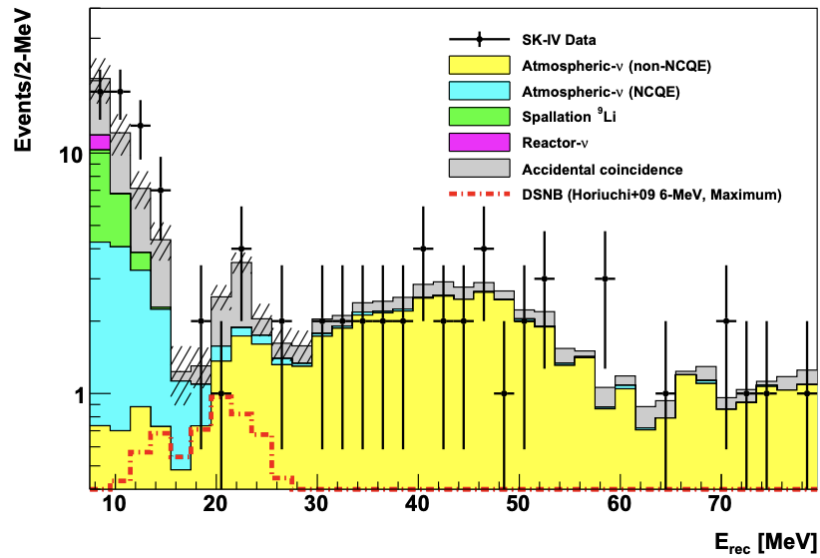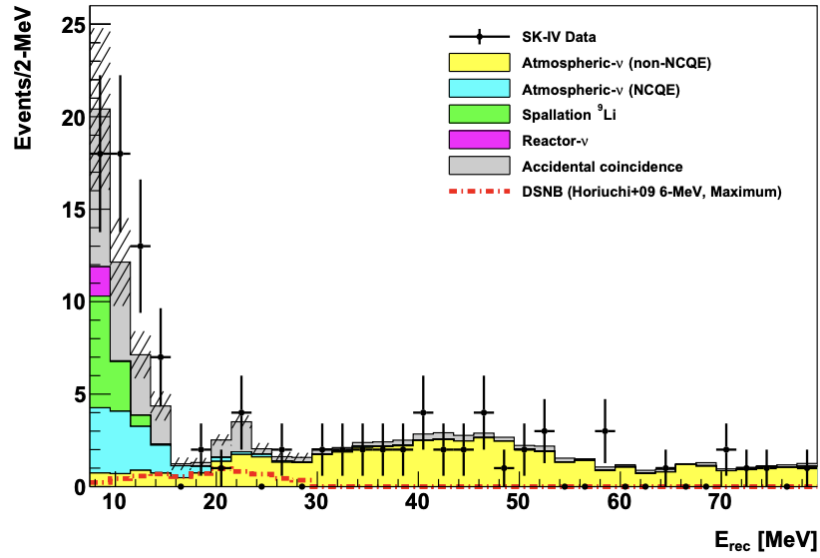
Figure 2.17: The energy spectra of DSNB background [20]
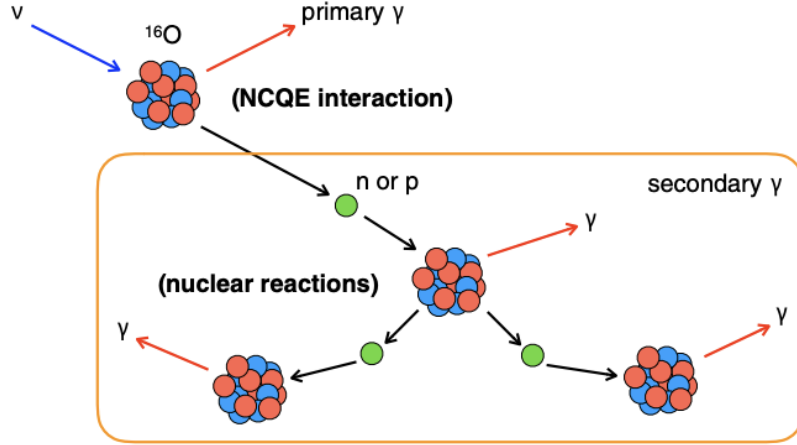
Figure 2.18: Schematic of NCQE interaction [34]

become background events. In the energy region below about 20 MeV, the associated background is about 106 times higher than the DSNB flux prediction and the spallation reduction is essential.

Most spallation isotope produce only β and γ and these backgroud events can be reduced using neutron tagging, but a few isotopes undergo a $\beta + n$ decay that mimics the IBD signal and these backgroud events cannot be removed using only neutron tagging. These spallation reductions require both dedicated reduction techniques and neutron tagging, with the modelling matched to each isotope. The isotope lifetimes and the end-point energies of their decays are summarized in Figure 2.19. Isotopes that undergo $\beta + n$ decays include ^{8}He, ^{11}Li, ^{16}C and ^{9}Li. In particular, ^{9}Li has a non-negligible yield ($1.9 \times 10^{-7} \, \mu^{-1}.\mathrm{g}^{-1}.\mathrm{cm}^2$), a half-life of about 0.18 sec, decays into $\beta + n$ pair with a branching ratio of 50.8%, and the decay of ^{9}Li is similar to the IBD event in DSNB. The differences are that the β of ^{9}Li is an electron and the neutron energy is higher in ^{9}Li than in DSNB. However, since SK does not distinguish between positrons and electrons and neutron energies cannot be measured, ^{9}Li decay is modelled using IBD Monte-Carlo simulations. ^{9}Li production rate is estimated to be $0.86 \pm 0.12(\mathrm{stat.}) \pm 0.15(\mathrm{syst.}) \, \mathrm{kton}^{-1}.\mathrm{day}^{-1}$ [36].
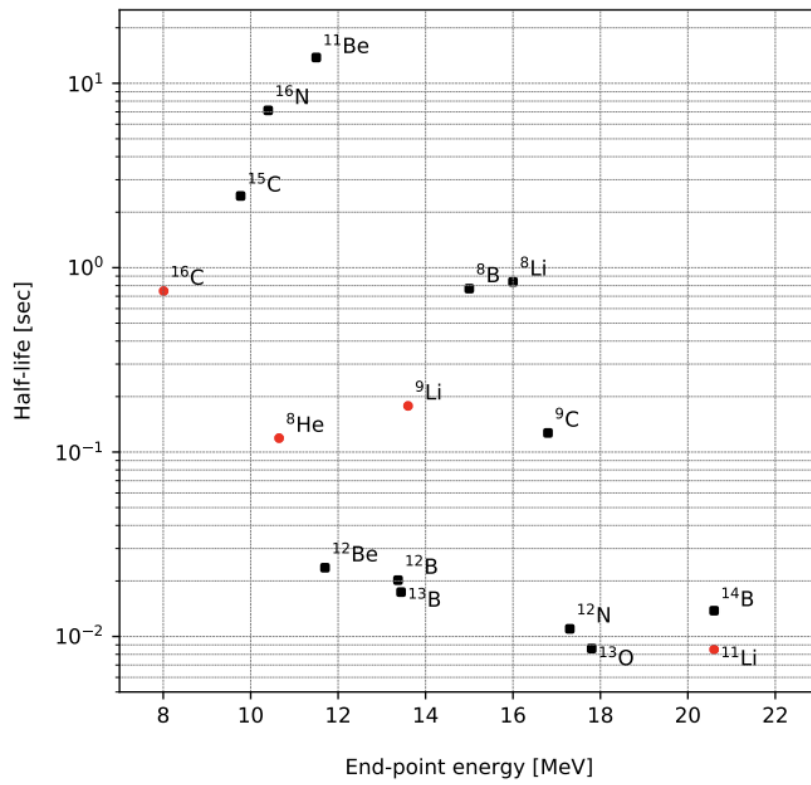
Figure 2.19: End-point energies and half-lives [20]

Chapter 3

Overview of calibrations in a few to tens of MeV region

In this section, an overview of calibration for the SK low energy region is described. To evaluate the energy of the particles which are interacted in the SK detector precisely, calibration is very important. The schematic diagram of the flow of conversion of energy and the kind of calibration used in this flow is shown in Figure 3.1.

3.1 Basic calibrations

In the low energy region, the number of PMT hits is used for energy. This is because the number of photoelectrons detected at each PMT is mostly 1 or 0, as the expected value of the number of incoming photons per PMT is sufficiently smaller than 1. Therefore, the number of PMTs that detect photoelectrons is a good approximation of the total number of photoelectrons. N_{50} is the number of PMT hits within 50 ns. Since the N_{50} has the event vertex position dependence due to water conditions and effects of dark noise and quantum efficiency of PMT, the N_{50} is corrected for these effects. Basic calibrations can be divided into two main categories: PMT related and water related, and these calibrations are used for these correction factors described in the below "Summary of calibration parameters". The relation between each correction factor (calibration parameter) and calibration is shown as follows.

Summary of calibration parameters

- PMT related
    - Gain, C_{gain}
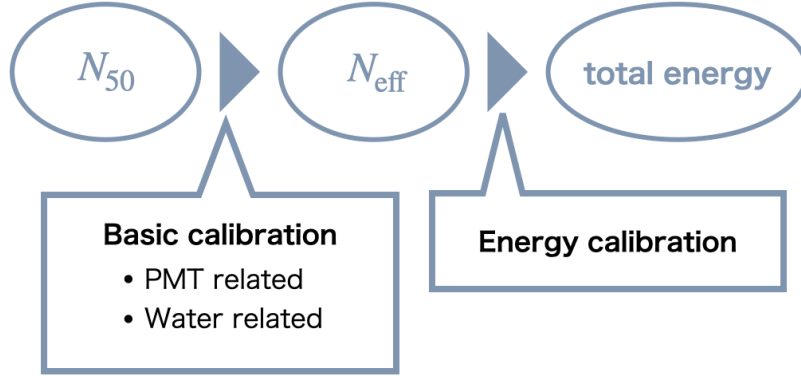
Figure 3.1: The schematic diagram of the flow of conversion of energy and the kind of calibration. In the low energy region, energy is detected using the N_{50} (the number of PMT hits within 50 ns) parameter. N_{eff} (the effective number of hits) is calculated by the correction factors derived from the basic calibration. Energy calibrations allow MC simulation to accurately reproduce the data and the total energy is reconstructed.

Scaling factor of the size of PMT signal. It does not affect the reconstructed energy directly, because the number of PMT hits is used for the energy reconstruction. However, it affects the efficiency to detect a hit above the threshold of the electronics. This effect is reproduced in the simulation.

– QE (Quantum Efficiency to detect photon)
QE affects the probability of a photon detected by a PMT. The evaluation of QE is described in Section 4.1.1.

– Dark noise
Random PMT hit rate mostly caused by spontaneous thermal electron emission. Dark noise for energy reconstruction is randomly produced at a defined rate in MC simulation.

- water related

– α_{abs}, α_{sym}, α_{asym}
coefficients for absorption and scattering (symmetric or asymmetric). The details of these parameters are described in Section 4.2.1.

– C_{abs}
Scaling factor of absorption coefficient to implement time variation of water transparency. It is evaluated by fitting the correlation plot between C_{abs} and water transparency with 50 MeV electrons produced for each different value of C_{abs} in MC simulation.

– C_{sca}

Scaling factor of scattering coefficient to minimize position dependence of N_{eff}. 10 MeV electrons are generated in MC simulation and N_{eff} is calculated at different values of C_{sca}. The best C_{sca} is selected from the value which minimizes the position dependent variation of N_{eff}.

– β

Coefficient for z position dependence of water transparency. The detail of the parameter β is described in Section 4.2.3.

Summary of basic calibration

- calibration using NiCf source

  NiCf source is inserted into the tank and γ rays are detected to measure QE and z position dependence of the water transparency. The detail of NiCf calibration is described in Section 4.1.1.

- laser calibration

  N_2 laser with short pulse widths (< 0.4ns) is used and inserted into the tank to measure PMT hit timing and water parameters. The laser calibration for PMT hit timing is described in Section 4.1.2 and that for water parameters is described in Section 4.2.1.

- Decay electron calibration

  Decay electron is generated from cosmic ray muon stopped in the detector and is used to grasp the temporal variation of the water quality. The detail of decay electron calibration for the water quality measurement is described in Section 4.2.2.

The effective number of hits N_{eff} is calculated by correcting N_{50} using these correction factors. Basic calibrations are explained in Chapter 4.

3.2 Energy calibrations

Energy calibrations are explained in Chapter 5. These calibrations measure the energy scale and help MC simulation reproduces the data more accurately.

The following kinds of energy calibration are used in SK.

Calibration with instruments

- LINAC

  An electron linear accelerator called a LINAC is used to launch electrons

Table 3.1: The relation between calibration parameter and calibration

PMT related parameters	Evaluation method
Gain	the hits in the off-timing window of cosmic muons
C_{gain}	Decay electron
QE	NiCf calibration
Dark noise	the hits in the off-timing window of the LE trigger data

Water related parameters	Evaluation method
α_{abs}, α_{sym}, α_{asym}	laser calibration
Water transparency	Decay electron
C_{abs}	MC simulation
C_{sca}	MC simulation
β	NiCf calibration

of certain energy into each position in the SK tank. The absolute value of the energy scale is calibrated. LINAC is described in Section 5.2.1.

- DT calibration
  Electrons generated isotropically by β decay of ^{16}N are used. The validity of the energy scale determined by LINAC is checked. In addition, DT calibration is used to evaluate the directional dependence of the energy scale. DT calibration is described in Section 5.2.2.

Cosmic ray induced

- ^{16}N
  This calibration is performed using ^{16}N generated by cosmic muon captured by ^{16}O in the tank to evaluate the energy scale for solar neutrino detection. ^{16}N calibration is described in Section 5.2.3.

- Decay electron
  Electrons generated by muon decay are used to evaluate the energy scale. The decay electron for energy scale calibration is described in Section 5.2.4.

LINAC and DT calibration are also used to evaluate the systematic uncertainty of the energy scale. The systematic uncertainty for position dependence of energy reconstruction is estimated by comparing the data from LINAC and MC simulation. The systematic uncertainty for directional dependence is estimated by the data from DT calibration. The systematic uncertainty of the energy scale of the current solar neutrino observation is summarized in Table 3.2.

Table 3.2: Systematic uncertainty of energy scale of the current solar neutrino observation [37]

Position Dependence	0.44%
Direction Dependence	0.10%
Water Transparency	0.20%
LINAC Energy	0.21%
Total	0.54%

The systematic uncertainty for the position dependence of the energy scale in the SK-IV result was 0.44%. This uncertainty is due to the difference between the data and MC simulation. It is necessary to improve MC simulation to reduce this uncertainty with a more accurate evaluation of the position dependence and the time dependence of the water transparency. However, the number of data taking points for LINAC and DT calibration is limited and these calibrations don't provide sufficient information to improve MC simulation. We need to evaluate more detailed position dependence.

3.3 Motivation for energy calibration using spallation neutrons

This study aims to develop a new energy calibration using spallation neutron. In SK, the addition of gadolinium in 2020 made it possible to detect spallation neutrons via Gd(n,γ) reactions. Spallation neutrons have the following features.

- Produced throughout the entire detector.

- Produced all time.

- High rate of production and detection.

LINAC and DT calibration have limited data taking points and data taking periods. Thanks to the above features of the spallation neutrons, we can do the calibration of the energy scale that evaluates the position dependence and time dependence in more detail than LINAC and DT calibration.

More details on spallation neutrons and the event selection method developed in this study are described in Chapter 5, the evaluation of time variation of energy using spallation neutrons is in Chapter 7, and the discussion of energy calibration methods using spallation neutrons is in Chapter 8. In the study of energy calibration using spallation neutron, our aim is to develop a calibration in which the position dependence is suppressed to about the level of systematic uncertainty in

the current solar neutrino observation ($\sim$0.5%). In this thesis, we evaluated the position dependence using current MC simulation and spallation neutron data.

Chapter 4

Calibration of SK detector response

In this chapter, calibration methods in the Super-Kamiokande detector are described. The main components of the detector are the PMT and water. It is extremely important to understand them in order to obtain reliable data and to make accurate measurements.

4.1   PMT related calibration

4.1.1   Relative QE

The number of PMT hits is used for energy reconstruction of low-energy events where only one photon enters one PMT. Each PMT has individual differences and we need to take that into account. In order to understand the properties of each PMT, we calculate the relative quantum efficiency from a detector calibration using NiCf source, and make the QE table that summarizes the PMT identification numbers and relative quantum efficiencies. The structure of the NiCf source is shown in Figure 4.1. A green 16 cm diameter ball made from 35% nickel oxide (NiO) and 65% polyethylene have a hole in the center. A neutron source, californium 252 (^{252}Cf), is placed in the center of the hole, and the top and bottom are covered with brass rods.

The principle of Cherenkov light generation from the NiCf source is as follows.

1. ^{252}Cf has a half-life of 2.65 years, 96.9% undergo α decay and the remaining 3.1% undergo spontaneous fission.

2. The average of 3.76 neutrons with 2.1 MeV and the average of 10 gamma rays with 10 MeV are produced in a single fission.
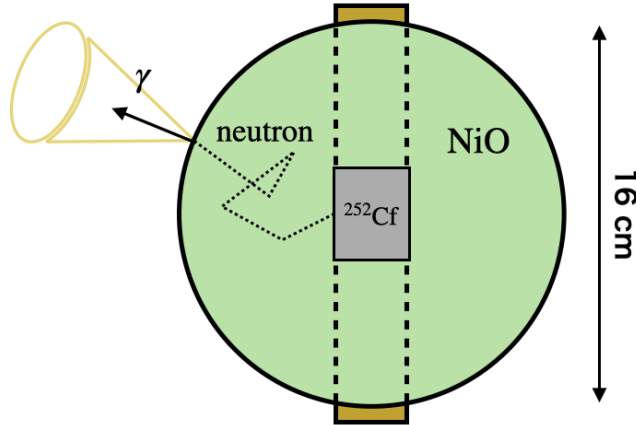
Figure 4.1: Structure of NiCf source

3. The generated neutrons are elastically scattered about 20 times with the protons in the polyethylene in a few μsec.

4. Every time elastic scattering occurs, the neutrons lose energy and are eventually thermalized.

5. Thermalized neutrons are captured by Ni nuclei and gamma rays (6-9 MeV) are emitted.

6. Gamma rays in water cause electron-positron pair production and compton scattering, resulting in the emission of Cherenkov light. Cherenkov light is detected by PMTs.

This Cherenkov light is so weak that only one photon can enter one PMT, and is emitted isotropically from the NiCf source. The NiCf source is therefore suitable for measuring relative quantum efficiency.

Figure 4.2 shows the flow chart of the analysis to obtain the relative QE. NiCf events are selected from the acquired data and the number of hits for each PMT is calculated and corrected to determine the relative hit rate. Equivalent analysis is also performed for MC simulation. Relative QE can be obtained by comparing data and MC hit rates.

$$QE = \frac{\mathrm{HR_{Data}}}{\mathrm{HR_{MC}}} \tag{4.1}$$

where HR represents hit rate.

Figure 4.2 shows the latest (updated on 16/09/2022) relative QE for z-direction of the SK tank.
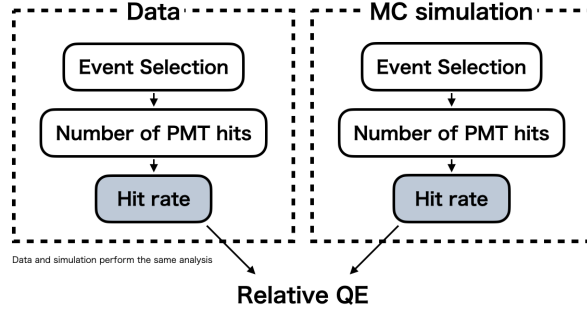
Figure 4.2: the flow chart of the analysis of QE
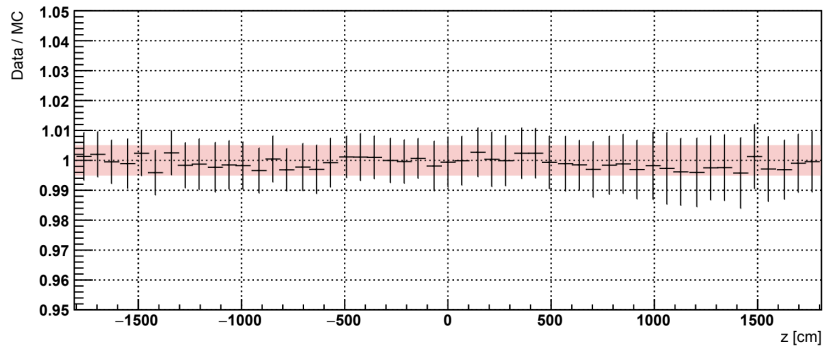
Figure 4.3: The relative QE updated on 16/09/2022 [38]. The vertical axis represents QE (ratio of data hit rate to MC hit rate) and the horizontal axis represents z direction of the SK tank. Black dots represent the QE at each z position. One plot point is the average of 150 PMTs for one round of the barrel. The red area is the area within $\pm 0.5\%$, and the data at any position is within 0.5%.
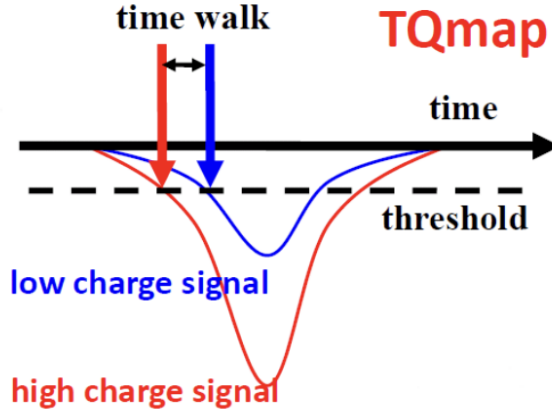
Figure 4.4: Schematic diagram of the time walk [39]. High charge signal (red line) have higher pulses and faster the rise time than low charge signal (blue line).

4.1.2 Relative timing

The PMT timing information is the important item for the reconstruction of the vertex position. Timing responses are not the same between PMTs due to cable length differences and electronics response variations. Timing calibration corrects for these variations. Due to the property of the signal of the PMT, the time-walk occurs when the different amount of charge is observed (Figure 4.4). Time and charge correlation is evaluated using N_2 laser with short pulse widths (< 0.4ns) to correct for time walk and to time calibrate the PMT (Figure 4.5.). The relation between time and charge is called "TQ-map", which is the timing as a function of the pulse height. This map is then fitted by various polynomial functions depending on the charge range. The fitted parameters are then used to correct the time response of each PMT as a function of the observed charge. Figure 4.6 shows the TQ-map for SK-IV. The vertical axis of the TQ-map corresponds to the signal detection time $t - t_{tof}$, and the larger the value, the earlier the detection time. QBin on the horizontal axis represents the value corresponding to the detected charge Q [pC]. The obtained correlation between $t - t_{tof}$ and QBin is fitted with a polynomial function, and the obtained fitting function is added to the signal detection time to correct the time shift due to the time walk.
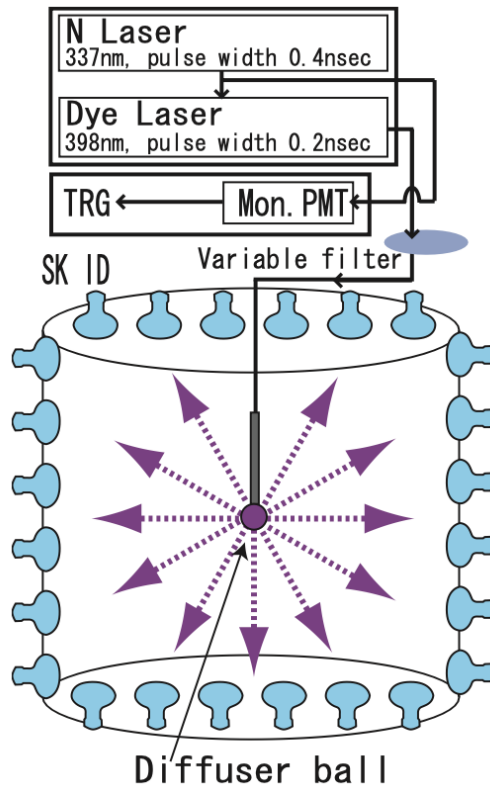
Figure 4.5: Schematic diagram of time calibration using laser
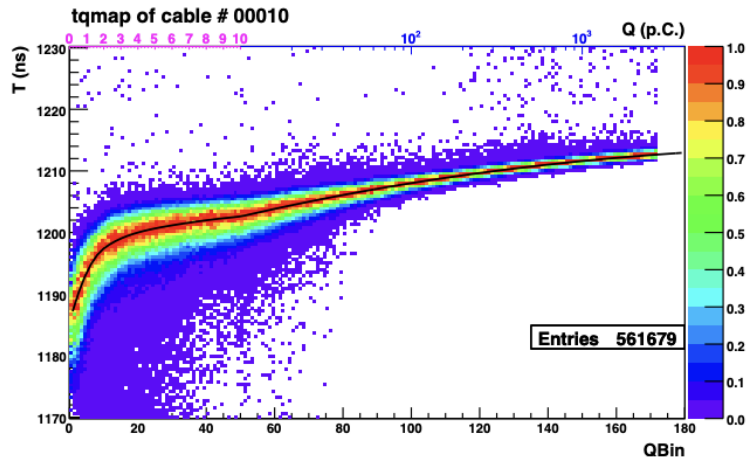
Figure 4.6: TQ-map for SK-IV PMT. The horizontal axis is charge of each hit (QBin), and the vertical axis is time [ns] after subtracting the time of flight.

4.2 Water related calibration

Since the amount of detected Cherenkov light changes depending on the water transparency, the parameters related to water are important correction terms in reconstructing the energy with high accuracy. There are two methods for measuring the water transparency, one using a laser and the other using decay electrons from cosmic ray muon.

4.2.1 Water parameter tuning with laser

The attenuation of light is expressed by the exponential function,

$$I(\lambda) = I_0(\lambda)\exp(-r/L(\lambda)) \tag{4.2}$$

where λ is the wavelength of light, $I_0(\lambda)$ is the initial light intensity, r is the distance traveled by light, and $L(\lambda)$ is the water transparency.

Light is subject to absorption or scattering effects while traveling through water. Scattering is divided into symmetric scattering and asymmetric scattering. When the scattering angle is θ, the angular distribution of scattered light in symmetric scattering is expressed as $1+\cos 2\theta$. In asymmetric scattering, the scattering probability increases linearly when $0 < \cos\theta < 1$, and when $\cos\theta < 0$, the scattering probability is zero (Figure 4.7). The water transparency in MC is expressed by the following equation,

$$L(\lambda) = \frac{1}{\alpha_{\mathrm{abs}}(\lambda) + \alpha_{\mathrm{sym}}(\lambda) + \alpha_{\mathrm{asy}}(\lambda)} \tag{4.3}$$

where $\alpha_{\mathrm{abs}}(\lambda)$, $\alpha_{\mathrm{sym}}(\lambda)$, $\alpha_{\mathrm{asy}}(\lambda)$ represent parameters for absorption, symmetric scattering, and asymmetric scattering, respectively. Also, these parameters are expressed as follows using the coefficients P_0 to P_8.

$$\alpha_{\mathrm{abs}}(\lambda) = P_0 \times \frac{P_1}{\lambda^4} + P_0 \times P_2 \times 0.0279 \times (\frac{\lambda}{500})^{P_3} \tag{4.4}$$

$$\alpha_{\mathrm{sym}}(\lambda) = \frac{P_4}{\lambda^4} \times (1.0 + \frac{P_5}{\lambda^2}) \tag{4.5}$$

$$\alpha_{\mathrm{asy}}(\lambda) = P_6 \times (1.0 + \frac{P_7}{\lambda^4} \times (\lambda - P_8)^2) \tag{4.6}$$

The coefficients P_0 to P_8 are derived by fitting the laser data.

Laser light of five different wavelengths (337, 375, 405, 445, 473 nm) is injected into the tank. Laser injectors are parmanently installed at seven places (Top×1, Barrel×5, Bottom×1) as shown in Figure 4.8 and. For data analysis, we select hits of scattered light from the timing of the hits, compare the hit ratio versus timing
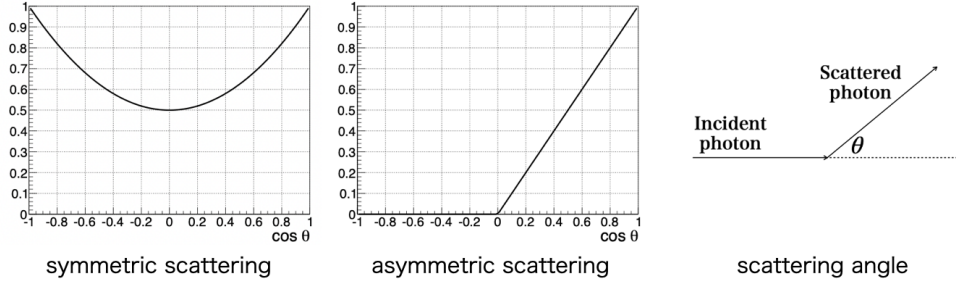
Figure 4.7: photon scattering [40]

plots between the data and MC, and extract the best values for P_0 to P_8. The values of P_0 to P_8 obtained from the data obtained from 01/01/2021 to 01/02/2021 are summarized in the table 4.1.

Table 4.1: The summary of the coefficients P_0 to P_8.

P_0	P_1	P_2	P_3	P_4	P_5	P_6	P_7	P_8
0.615067	44854600	1.14829	14.4675	103455000	77171.9	$2.42803e^{-4}$	14.9426	41475.0

4.2.2 Water transparency measurement with decay electron

Decay electron (decay-e) from cosmic ray muons stopped in the detector are used to measure the average water transparency throughout the detector. The main purpose of this measurement is to constantly monitor the water in the detector, and to grasp the temporal fluctuations of the water quality. After a decay electron event from a cosmic-ray muon is selected, the average charge N_i given by the Cherenkov photon and the average distance d_i between the PMTs that detected the Cherenkov photon signal and the point where the decay electron event occurred is calculated. The relation between the number of Cherenkov photon and the distance is shown in Figure 4.10. Some segments are created by dividing the Cerenkov ring into the polar angle and the azimuthal angle with respect to the direction of decay electron. Then, N_i is calculated in each segment as,

$$N_i = (X_i + \epsilon_{\text{tail}} - \epsilon_{\text{dark}}) \times \frac{N_{\text{alive}}}{N_{\text{all}}} \times \frac{S(0,0)}{S(\theta_i, \phi_i)} \times \frac{1}{QE_i}. \tag{4.7}$$
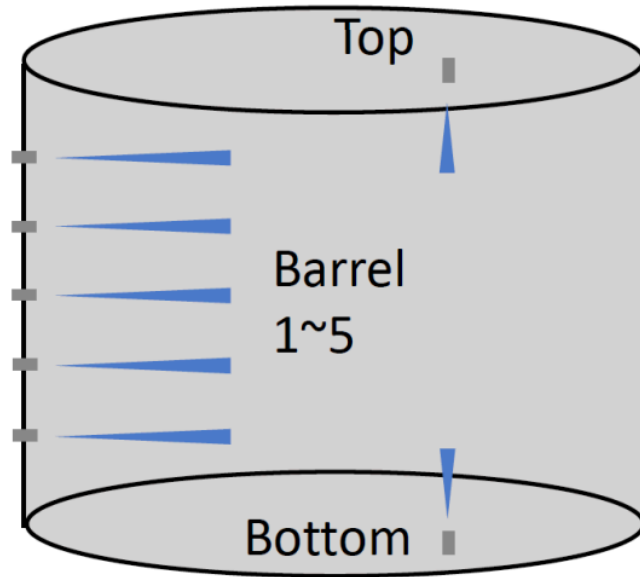
Figure 4.8: The location of laser injector [38]
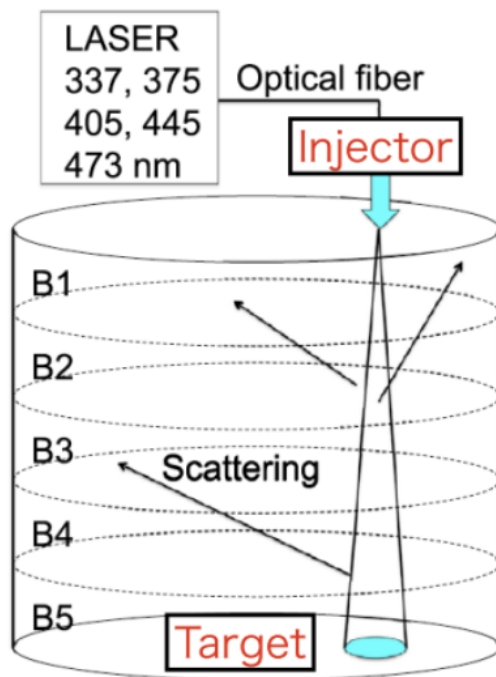
Figure 4.9: Schematic of water parameter measurement using laser [38]
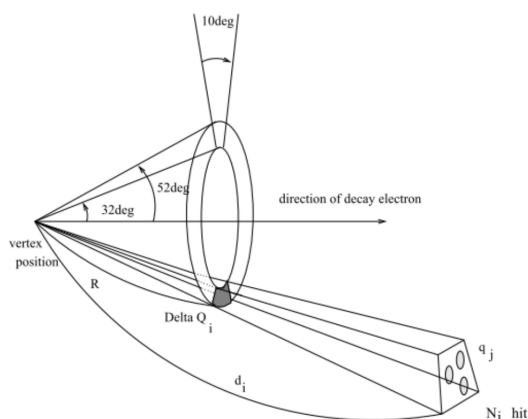
Figure 4.10: The schematic diagram of the Cherenkov ring [41].

Each element used in this formula is explained in 4.1.3.

The derived distribution of charge vs. distance is fitted with an exponential function to derive the attenuation coefficient (= water transparency). Figure 4.11 shows the time variation of water transparency. The data is used from the middle of SK-IV to SK-VI.

4.2.3 Top Bottom Asymmetry

As described in Section 2.4.2, in the SK water circulating system, purified water is put in from the bottom and withdrawn from the top, so the bottom has a higher water transparency than the top. This asymmetry is called Top Bottom Asymmetry (TBA). TBA is monitored by using the laser and the NiCf source.

The measurement of the hit rate by the NiCf source also provides an estimate of TBA of the water transparency. As discussed in Chapter 2, it has been observed that there is a top-bottom asymmetry in water transparency due to the effect of water circulation. The TBA is expressed as the following equation,

$$TBA = \frac{\langle \text{top} \rangle - \langle \text{bottom} \rangle}{\langle \text{barrel} \rangle} \tag{4.8}$$

where $\langle \text{top} \rangle$ is the average PMT hit rate on the top surface, $\langle \text{bottom} \rangle$ is the average PMT hit rate on the bottom surface and $\langle \text{barrel} \rangle$ is the average PMT hit rate on the sides.

The position dependence of the water transmission length is a source of systematic uncertainty in the energy reconstruction. To suppress this, the positional dependence of the water transparency is also introduced in the MC simulation
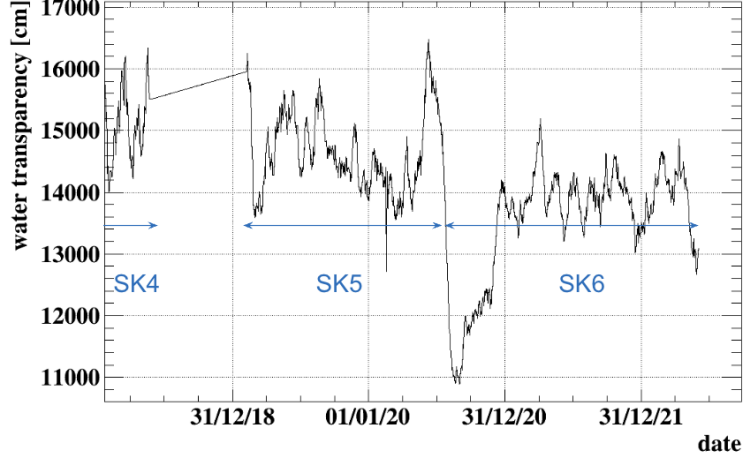
Figure 4.11: Time variation of water transparency [41]. The data of the middle of SK-IV to SK-VI is used.

in the form of dependence linearly in the height z direction, as in the following equation. For SK-IV and SK-VI,

$$
L(\lambda) = \begin{cases} \dfrac{1}{\alpha_{\mathrm{abs}}(\lambda) \cdot (1 + z \times \beta) + \alpha_{\mathrm{sym}}(\lambda) + \alpha_{\mathrm{asy}}(\lambda)} & z > -11\mathrm{m}, \\[4mm] \dfrac{1}{\alpha_{\mathrm{abs}}(\lambda) \cdot (1 - 11 \times \beta) + \alpha_{\mathrm{sym}}(\lambda) + \alpha_{\mathrm{asy}}(\lambda)} & z < -11\mathrm{m} \end{cases} \tag{4.9}
$$

For SK-V,

$$
L(\lambda) = \frac{1}{\alpha_{\mathrm{abs}}(\lambda) \cdot (1 + z \times \beta) + \alpha_{\mathrm{sym}}(\lambda) + \alpha_{\mathrm{asy}}(\lambda)} \tag{4.10}
$$

where β is a parameter that expresses the level of TBA of water quality. In SK-IV and SK-VI, the water at $z < -11$m was convecting and it can be assumed that the water quality is uniform. In SK-V, since convection does not occur, $\alpha_{\mathrm{abs}}(\lambda)$ depends on z for all range in the z direction. The z dependence is applied to only the absorption coefficient $\alpha_{\mathrm{abs}}(\lambda)$.

β is a variable introduced to incorporate TBA and its time variation into MC simulations, expressed as a function of TBA,

$$
\beta = a \times TBA + b \tag{4.11}
$$

The parameters a and b are determined in the analysis of NiCf data. The distribution of hit rates for the NiCf data is calculated from runs of different periods. The value of β that best reproduces the hit rate distribution is then derived for

55
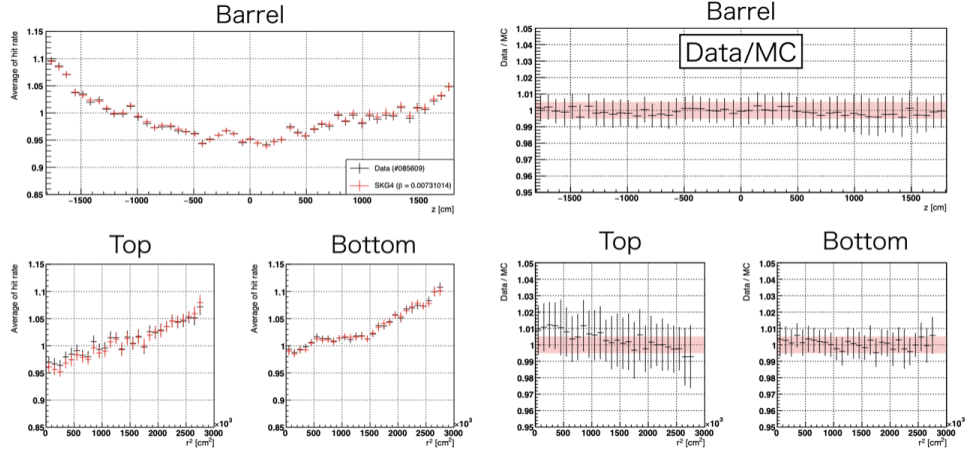
Figure 4.12: Hit rate and its ratio with the best β value [38].

each run. The best β in SK-VI was obtained as 0.00731014 [1/m] uisng the Ni data of Jan, 21st 2021. Hit rate and its ratio with the best β value are shown in Figure 4.12.

In addition, using the obtained a and b, the time variation of β is derived from the time variation of TBA. Time variation of TBA is evaluated using the lamp of the auto-Xe. Figure 4.13 shows the time variation of TBA.
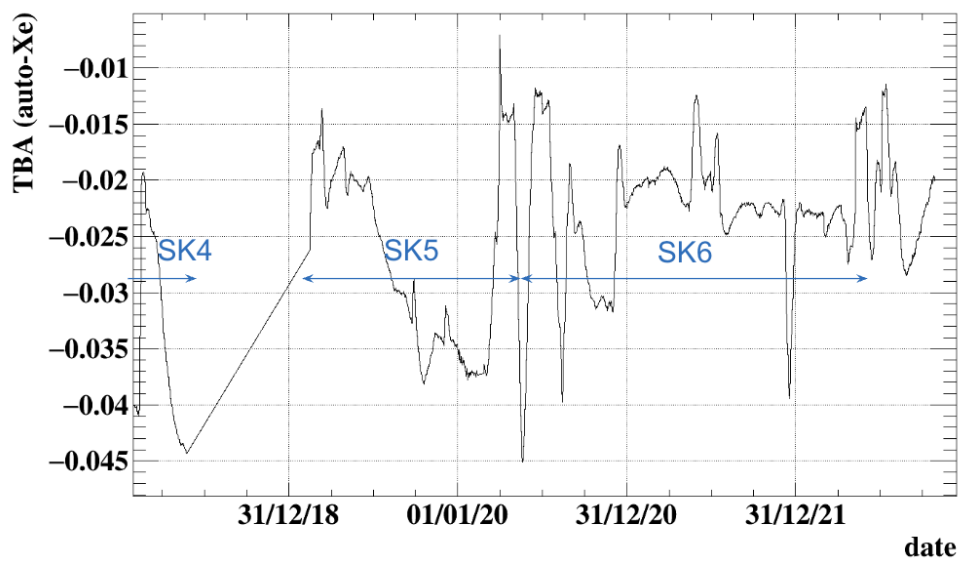
Figure 4.13: Time variation of TBA measured with auto-Xe data [41].

Chapter 5

Energy reconstruction and calibration in a few to tens of MeV region

5.1 Event reconstruction

In the SK, there are many analysis tools to reconstruct events because the SK detector has many physics targets. In this chapter, the event reconstruction method for low energy region is described.

5.1.1 Vertex reconstruction

In the low energy region, the trajectory of the charged particle is assumed to be a point at the vertex. For example, an electron with an energy of 20 MeV can travel a distance of about 10 cm in pure water, which is much smaller than the vertex resolution of 50 cm [37].

In order to reconstruct the vertex position, a maximum likelihood fit to the timing of Cherenkov signal is used. This maximum likelihood fitting program is called BONSAI (Branch Optimization Navigating Successive Annealing Interactions). The time information in the PMT hit information is used to reconstruct the event occurrence point. For each hit PMT, a residual time $t - t_{\text{tof}} - t_0$ is defined, where t is the PMT hit time, t_{tof} is the time it took for the photon to reach the hit PMT from the event point, t_0 is the time of the interaction. Using the timing residual information, the likelihood function is defined as

$$\mathcal{L}(\vec{x}, t_0) = \sum_{i=0}^{N_{\text{hit}}} \ln P(t_i - t_{\text{tof},i} - t_0) \tag{5.1}$$

58
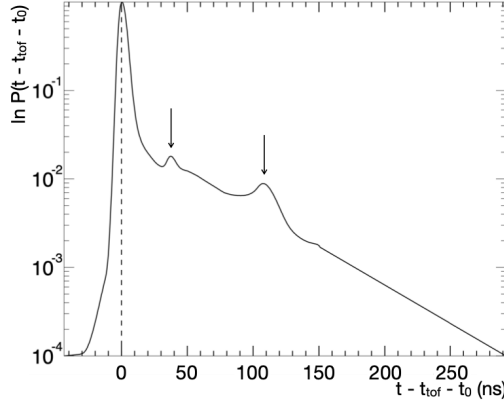
Figure 5.1: The probability density function of the residual time used for the vertex reconstruction maximum likelihood fit [40]. The second and third peaks around 30 nsec and 100 nsec are caused by the PMT's after pulses.

where $\vec{x}$ is the position of the event point candidate and $P(t_i - t_{\text{tof},i} - t_0)$ is the probability density function of the timing residual for a single photoelectron signal as shown in Figure 5.1. The likelihood function $\mathcal{L}(\vec{x}, t_0)$ is calculated at each point while changing $\vec{x}$ in the detector, and the position with the maximum value is determined as the vertex point. The accuracy of event reconstruction depends on the energy, as the number of PMT hits varies with the energy of the generated charged particles. $P(t_i - t_{\text{tof},i} - t_0)$ is derived together with the vertex resolution by LINAC. The vertex resolution is defined as the distance that contains 68% of the reconstructed events of LINAC and its energy dependence is shown in Figure 5.2.

g_{vtx} is defined as parameters that represents the goodness of the vertex reconstruction. The goodness of vertex reconstruction g_{vtx} is evaluated by the PMT hit time information.

$$
g_{vtx} = \frac{\sum_i \exp\left[-\left(\dfrac{t_i - t_{\text{tof},i} - t_0}{\sqrt{2}\omega}\right)^2\right] \exp\left[-\left(\dfrac{t_i - t_{\text{tof},i} - t_0}{\sqrt{2}\sigma}\right)^2\right]}{\sum_i \exp\left[-\left(\dfrac{t_i - t_{\text{tof},i} - t_0}{\sqrt{2}\omega}\right)^2\right]} \tag{5.2}
$$

where ω is the resolution of the $t_i - t_{\text{tof},i}$ distribution and σ is the time resolution of the PMT. g_{vtx} is the variable that takes values in the range 0 to 1, the closer to 1, the better the reconstruction is.
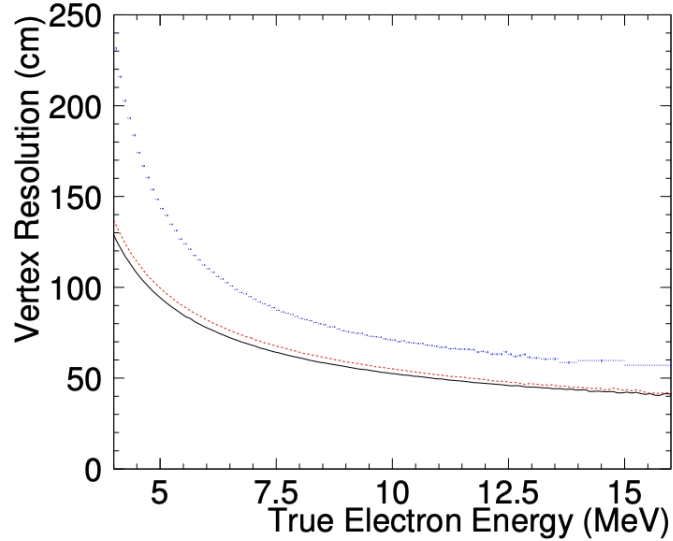
Figure 5.2: The energy dependence of position resolution in vertex reconstruction [42]. Each line represents the SK phase (Blue: SK-I, Red: SK-III, Black: SK-IV).

5.1.2 Direction reconstruction

The Cherenkov light ring pattern is used for direction reconstruction. The direction reconstruction uses the maximum likelihood method. The likelihood function is defined as

$$\mathcal{L}(\vec{d}) = \sum_{i=1}^{N_{20}} \left(\ln f(\cos\Theta_i, E) \times \frac{\cos\theta_i}{F(\theta_i)} \right) \tag{5.3}$$

where $\vec{d}$ is the direction of the charged particle and N_{20} is the number of PMT hits within 20 ns around the event occurrence time. $f(\cos\Theta_i, E)$ is the distribution function of the angle Θ_i between the direction of the charged particle and the observed photon direction. Since electrons pass through water undergoing multiple Coulomb scattering, $f(\cos\Theta_i, E)$ also depends on the energy E. $\frac{\cos\theta_i}{F(\theta_i)}$ is a correction term for solid angle. θ_i represents the angle of incidence of photons on the PMT as shown in Figure 5.3. $F(\theta_i)$ is a function of the sensitive area of the PMT depending on the incident angle θ_i and is given as,

$$F(\theta) = 0.205 + 0.524\cos\theta + 0.390\cos^2\theta - 0.132\cos^3\theta. \tag{5.4}$$

The goodness of the direction reconstruction g_{dir} is evaluated by the uniformity

60
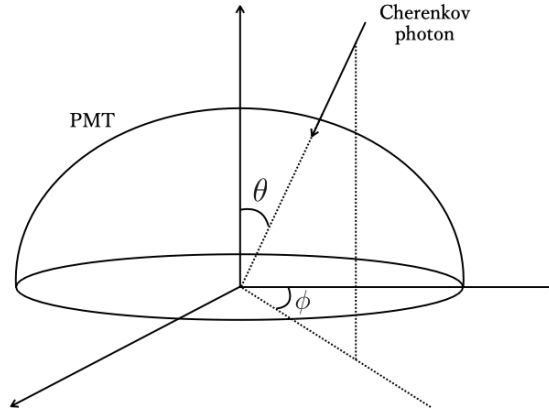
Figure 5.3: The definition of the incident angle of the photon on the PMT [40].

of hit PMTs based on the Kolmogorov-Smirnov test.

$$g_{dir} = \frac{\max\{\angle_{\text{uniform}}(i) - \angle_{\text{data}}(i)\} - \min\{\angle_{\text{uniform}}(i) - \angle_{\text{data}}(i)\}}{2\pi} \tag{5.5}$$

where, $\angle_{\text{uniform}}(i)$ represents the direction angle of the i-th hit PMT when PMT hits are assumed to be uniformly distributed around the ideal Cherenkov ring, and $\angle_{\text{data}}(i)$ represents the direction angle of the actual PMT hit. g_{dir} is the variable that takes values in the range 0 to 1, the closer to 0, the better the reconstruction is.

5.1.3 Energy reconstruction

For the energy reconstruction in the low energy (a few to tens of MeV) region, the effective number of hits N_{eff} is used. N_{eff} is calculated from the number of the PMT hits within 50 nsec time window N_{50} with corrections. N_{eff} is represented as follows,

$$N_{\text{eff}} = \sum_i^{N_{50}} (X_i + \epsilon_{\text{tail}} - \epsilon_{\text{dark}})/(1 + G_i \times C_{\text{gain}})$$

$$\times \frac{N_{\text{alive}}}{N_{\text{all}}} \times \frac{S(0,0)}{S(\theta_i, \phi_i)} \times \frac{1}{QE_i} \exp\left(\frac{r_i}{L_{\text{eff}}}\right) \tag{5.6}$$

The each parameter of the correction is as follows.

- X_i : The occupancy correction factor which corrects for the effect of having multiple photons in a single PMT.

- ϵ_{tail} : The correction factor to add late hits which are scattered or reflected during the travel in the water.

- ϵ_{dark} : The correction to remove dark rate hits in the 50 ns time window.

- $1 + G_i \times C_{\text{gain}}$: The effect of gain. This factor is introduced in SK-IV, but we do not use it in SK-V and SK-VI because the effect was found to be negligible in those periods.

- $\dfrac{N_{\text{alive}}}{N_{\text{all}}}$: The correction for the bad PMTs.

- $\dfrac{S(0,0)}{S(\theta_i, \phi_i)}$: The correction for the coverage of the PMTs as a function of photon incident angles.

- $\dfrac{1}{QE_i}$: The correction for the quantum efficiency (QE).

- $\exp(\dfrac{r_i}{L_{\text{eff}}})$: The correction for the attenuation of Cherenkov light in the water.

After all parameters are corrected and the number of effective PMT hits N_{eff} is determined, the total (kinetic and mass) electron energy is reconstructed as a function of N_{eff}. The relation between N_{eff} and reconstructed energy is given by the following equation obtained from MC simulation.

$$E(N_{\text{eff}}) = \begin{cases} p_0 + p_1 x + p_2 x^2 + p_3 x^3 + p_4 x^4 + p_5 x^5 & (\text{N}_{\text{eff}} < p_6) \\ p_0 + p_1 p_6 + p_2 p_6^2 + p_3 p_6^3 + p_4 p_6^4 + p_5 p_6^5 \\ \quad + (p_1 + p_2 p_6 + p_3 p_6^2 + p_4 p_6^3 + p_5 p_6^4)(x - p_6) & (\text{N}_{\text{eff}} > p_6) \end{cases} \tag{5.7}$$

The values of p_0 to p_6 are obtained by fitting. $E(N_{\text{eff}})$ is a 5th polynomial function below p_6 and a linear function above p_6. Parameters for the linear function are derived from the derivative of the 5th polynomial function, so that two functions are connected smoothly. Figure 5.4 shows the relation between the total reconstructed energy and N_{eff} and the values from p_0 to p_6 of SK-VI data.

5.2 Energy calibration

As mentioned above, in the low energy region, the energy is reconstructed using the effective PMT hit number N_{eff} corrected for the N_{50} number of PMT
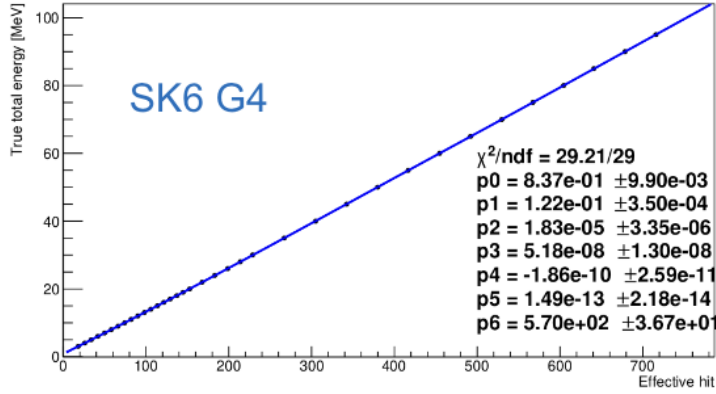
Figure 5.4: The the relation between the total reconstructed energy and N_{eff} and the values p_0 to p_6. Black dots show MC simulation results, blue line represents function derived by fitting. The SK-VI data is used. The values of p_0 to p_6 are obtained by fitting. "G4" written in the figure is the name of the simulation package.

hits that detected the light. In order for MC simulations to accurately reproduce the real data, the difference between the data and the MC simulated detector response must be kept small. For this purpose, energy calibration is carried out in the Super-Kamiokande using the electron linear accelerator LINAC (Linear accelerator) and the DT (Deuterium-Tritium neutron generator). Also, since the condition of the water in the detector is continuously changing, it is important to check the energy scale. Cosmic-ray-induced calibration sources are used for the energy scale evaluation. Since cosmic ray muons enter the entire detector at about 2Hz, the calibration source generated from the muons is constantly detected throughout the entire detector. In this chapter, the energy scale evaluation by ^{16}N and decay electron are also explained.

5.2.1 LINAC

Overview

The LINAC is placed above the tank of the SK detector. The LINAC beam pipe is inserted into the detector through a hole, called calibration hole, at the top of the detector, and electrons with the single energy (5, 6, 8, 10, 12 and 18 MeV) are ejected downwards. By the LINAC, the absolute value of the energy scale is calibrated and the systematic uncertainty on the position dependence of the energy reconstruction is estimated. The position of the calibration holes and the length of the beam pipe are fixed and data taking
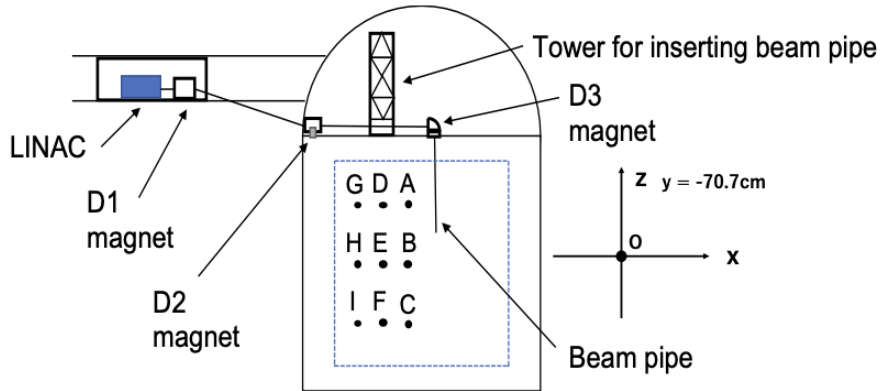
Figure 5.5: Schematic diagram of the LINAC measurement in Super-Kamiokande [43]. Points A to I represent data taking points.

is done typically at the nine points as shown in Figure 5.5.

Motivation

In the LINAC analysis, the value called COREPMT is determined which is introduced to correct for the average quantum efficiency of the PMTs installed in the detector. The N_{eff} between data and MC are compared and the value of COREPMT is tuned so that the value of N_{eff} becomes the same between data and MC. Then, the equation for the conversion from N_{eff} to energy is obtained on the basis of the correlation between N_{eff} and the energy of the generated charged particles. Furthermore, the data and the corresponding MC simulation are compared and the systematic uncertainty on the position dependence of the energy reconstruction is estimated (Figure 5.6).

Advantage

- Single energy electrons such as 5, 8, 10, 12 and 18 MeV can be injected.

Disadvantage

- The calibration holes are fixed, so detailed positional dependence cannot be checked.
- A lot of people is needed. At least 10 people are required to move the tower and manually extend each 4m beam pipe.
- The calibration can only be carried out once or twice a year.
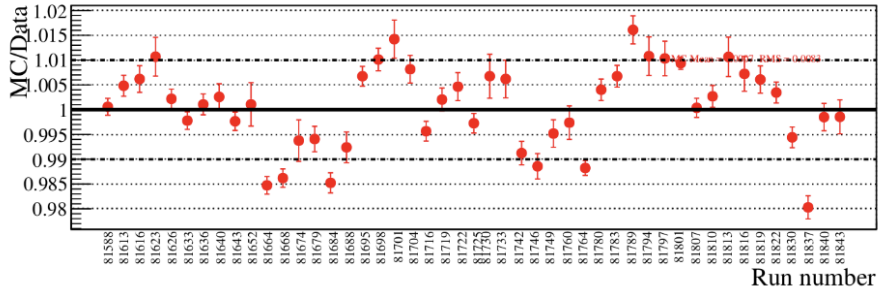
Figure 5.6: Ratio of N_{eff} obtained from data and MC simulation [41]. Data from August 6, 2019 to August 23, 2019 is used.

5.2.2 Deuterium-Tritium (DT) calibration

Overview

DT (Deuterium-Tritium neutron generator) calibration is a calibration that detects gamma rays and electrons using ^{16}N generated from the following reactions. First, helium and deuterium react to emit neutrons.

$$^{3}\text{He} + {}^{2}\text{H} \rightarrow {}^{4}\text{He} + n \tag{5.8}$$

Neutrons have an energy of 14.2 MeV and they are captured by ^{16}O. Then ^{16}N and protons are produced.

$$^{16}\text{O} + n \rightarrow {}^{16}\text{N} + p \tag{5.9}$$

The generated ^{16}N decay has the half life time of 7.13 s according to the Branching Ration (BR). Those with the BR greater than 1% are described below:

$$^{16}\text{N} \rightarrow {}^{16}\text{O} + \beta^{-}(\text{Q}:4.3\,\text{MeV}) + \gamma(6.1\,\text{MeV}) \qquad (\text{BR}:66.2\%) \tag{5.10}$$
$$^{16}\text{N} \rightarrow {}^{16}\text{O} + \beta^{-}(\text{Q}:10.4\,\text{MeV}) \qquad (\text{BR}:28\%) \tag{5.11}$$
$$^{16}\text{N} \rightarrow {}^{16}\text{O} + \beta^{-}(\text{Q}:3.3\,\text{MeV}) + \gamma(7.11\,\text{MeV}) \qquad (\text{BR}:4.8\%) \tag{5.12}$$
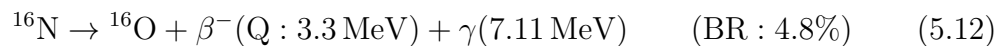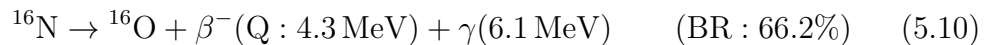
Reactions 5.8 and 5.9 are occurred in the SK detector using a Deuterium Tritium Generator (DTG) as shown in Figure 5.7. The flow of DT calibration is as follows.(Figure 5.8)

1. Submerge the DTG in water. DT calibration is carried out in the same position as LINAC.

65
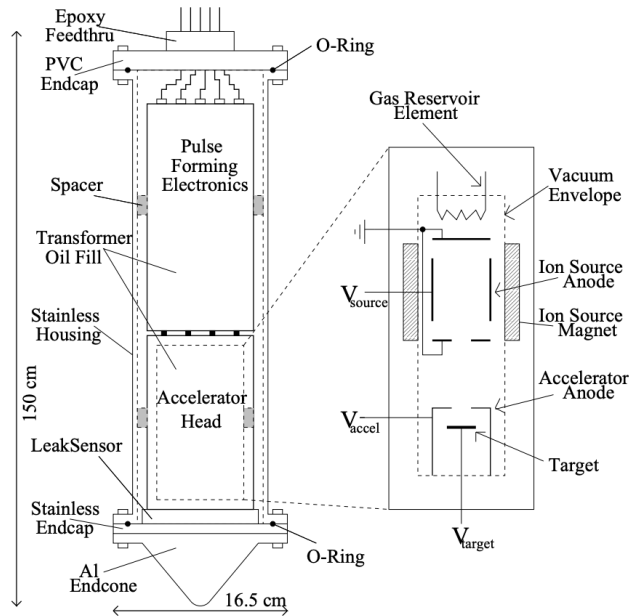
Figure 5.7: Schematic of the DTG setup [44]

2. Activate the DTG and emit neutrons. The pulse are irradiated at maximum 100Hz, $\sim 3 \times 10^6$ neutrons are emitted three times.

3. Raise the DTG by 2m so that it does not cast shadows. During this period, the data is not taken in order to eliminate the background caused by electrical noise generated by the crane.

4. Data taking is done for 40 seconds.

5. Repeat No.1 $\sim$ 4 20 $\sim$ 25 times per position.

Motivation

The DT calibration is performed to validate the energy scale and to evaluate the systematic uncertainty of the energy reconstruction determined by LINAC. In addition, electrons are produced isotropically in DT, whereas in LINAC electrons were only emitted in a downward direction. Therefore, systematic uncertainties on the directional dependence of the energy reconstruction, which could not be checked in LINAC, can be estimated.

Advantage

- Position dependence can be investigated at position where LINAC cannot be used.
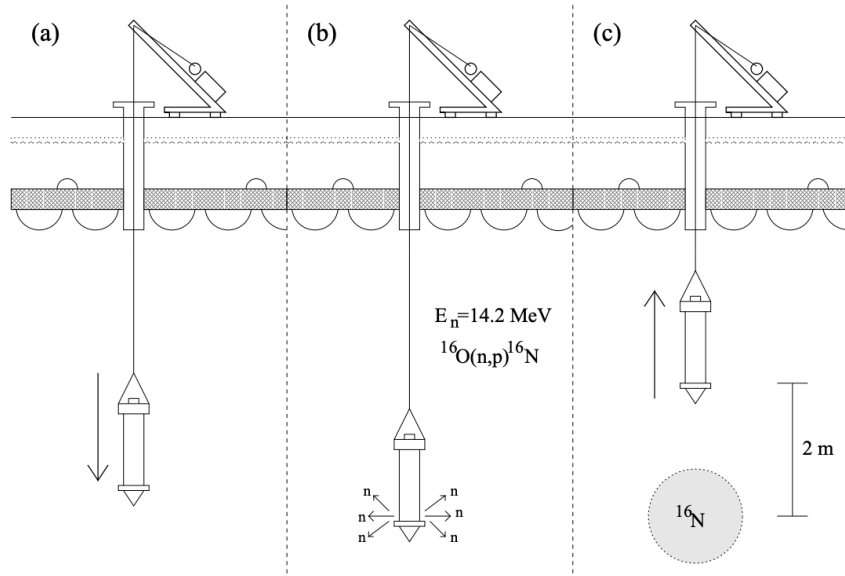
Figure 5.8: An overview of DTG data taking

- DT calibration can be worked with 2-3 people, less than LINAC.

Disadvantage

- The DTG itself interferes with the propagation of Cherenkov light, making it impossible to accurately analyze the energy response in some zenith angles.
- Because of beta decay, the electron energy is in a continuous spectrum.
- There are some branch events.

Result

Figure 5.9 shows the results of comparing N_{eff} obtained from the data and N_{eff} obtained from the MC simulation for each direction of the reconstructed electrons. A similar comparison was carried out for different generating positions and the systematic uncertainty for the directional dependence in the energy reconstruction was calculated to be 0.10 %.

5.2.3 ^{16}N energy scale calibration

Overview
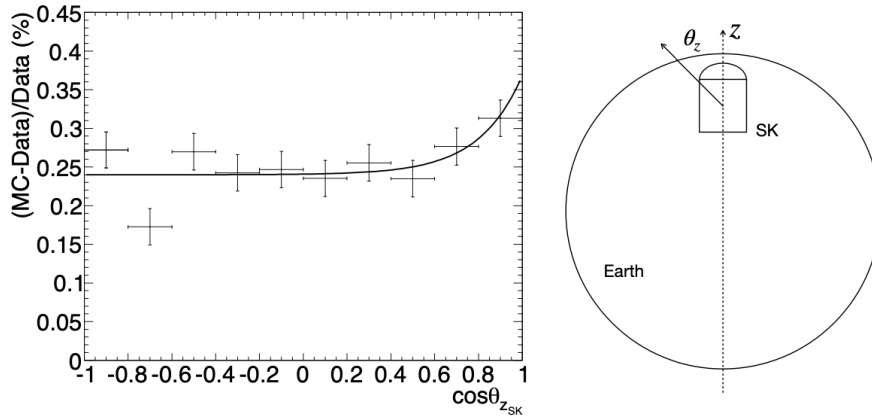
Figure 5.9: Directional (θ_z) dependence of the difference in N_{eff} obtained from data and MC simulations [44]. The horizontal axis represents the value obtained by taking the cos of θ_z, and the vertical axis represents the deviation between the data and the MC simulation. The rise seen around $\cos\theta_z = 1$ is due to the MC simulation not reproducing the effect of shadows created by the DT device itself.

When a cosmic ray muon is captured by ^{16}O, ^{16}O becomes ^{16}N and a muon neutrino is emitted,

$$^{16}\text{O} + \mu^- \rightarrow {}^{16}\text{N} + \nu_\mu \tag{5.13}$$

The produced ^{16}N undergoes the processes in Eqs. 5.10-5.12, which is the same as ^{16}N produced by the DT generator. These can be also used for energy calibration.

Motivation

^{16}N decay events are background events for solar neutrino observations. ^{16}N calibration is used to evaluate the energy scale for solar neutrino detection, since the observed decay events have the same energy range as solar neutrino.

Advantage

- Energy scale evaluation can be performed throughout the entire SK detector.
- The directional dependence of the energy scale can be investigated.
- The analysis can be performed using the entire SK period.
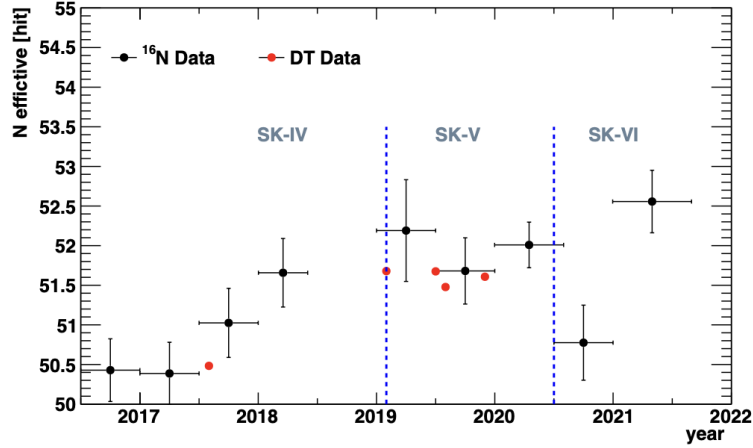
Figure 5.10: Energy scale evaluaiton of ^{16}N analysis and DT calibraiton analysis [43]. Black dots represent ^{16}N data, red dots represent DT calibration data.

Disadvantage

- ^{16}N are produced at a low rate and takes a long time to get enough statistics.

Result

Figure 5.10 shows the results of the time variation of the energy scale evaluated from the ^{16}N calibration. Using the selected ^{16}N events, the energy scale was evaluated every 2 years for SK-IV and every 6 months for SK-V and SK-VI [43]. It was found that the energy scale in the detector did not change significantly before and after the introduction of gadolinium, with agreement from SK-IV to SK-VI within the statistical error range.

The positional and directional dependence of the energy scale were analyzed using SK-IV data and compared with the DT calibration data. The results are shown in Figure 5.11 and Figure 5.12 respectively. It was shown that the energy scale has no position or direction dependence within a statistical error of ^{16}N.

5.2.4   Decay electron

Overview

Decay-e are used to evaluate the energy scale as well as time variations in the water transparency. Figure 5.13 shows the reconstructed energy spectrum of
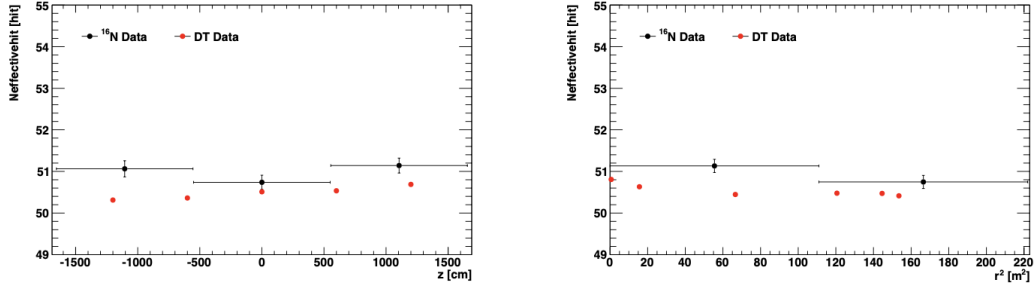
Figure 5.11: Pocation dependence of energy scale evaluated from ^{16}N analysis and DT calibraiton analysis [43] as a function of z(left) and r^2(right) with respect to reconstructed vertex.
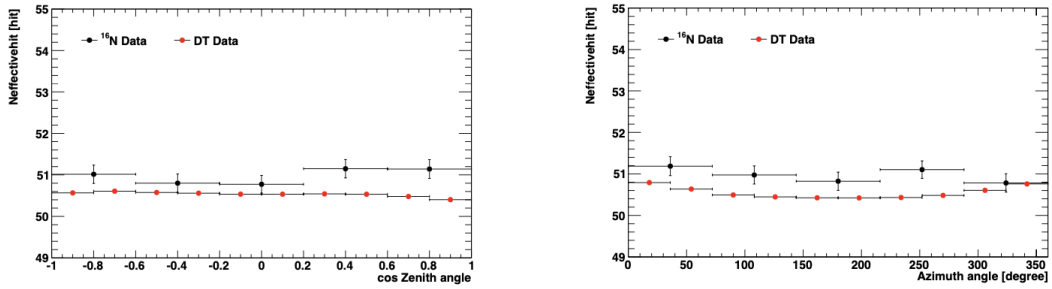
Figure 5.12: Directional dependence of energy scale evaluated from ^{16}N analysis and DT calibraiton analysis [43]. left: zenith angle cosθ. right: azimuth ϕ
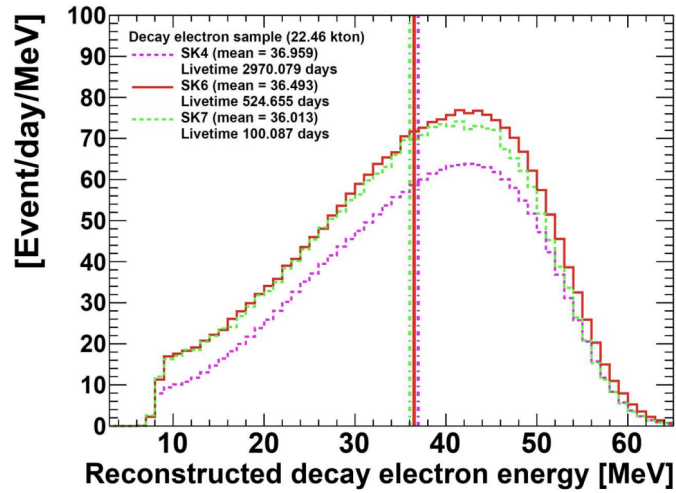
Figure 5.13: The reconstructed energy spectrum of decay-e [45].

decay electrons. Decay-e take energy from about 10 MeV to about 60 MeV. Therefore, in the low energy region, it is possible to evaluate the energy scale larger than 10MeV.

Advantages

- Energy scale evaluation can be performed throughout the entire SK detector.
- The analysis can be performed using the entire SK period.

Disadvantage

- Decay-e are produced at a low rate and takes a long time to get enough statistics.

Result

Figure 5.14 shows the results of the energy scale evaluation using decay-e. The gray area represents Gd-loading period. Soon after Gd-loading, the energy scale change at most ~2.7% level. For periods other than Gd-loading, the energy scale is consistent within ~1% level.

71
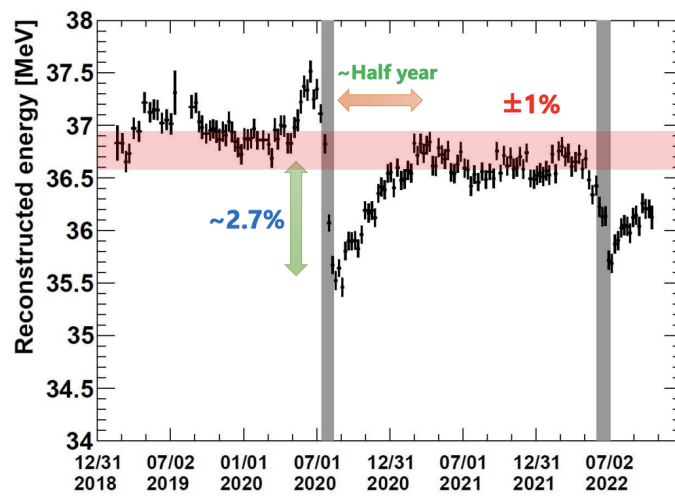
Figure 5.14: Energy scale evaluation of decay-e. The gray area represents Gd-loading period [45]. Soon after Gd-loading, the energy scale change at most ~2.7% level. For periods other than Gd-loading, the energy scale is consistent within ~1% level.

Chapter 6

Evaluation of spallation neutron signal

6.1 Motivation

The physics targeted by the low energy region of SK is the observation of solar neutrinos and the search for DSNB. For solar neutrino observations, the systematic uncertainty of the energy scale is 0.54%, of which 0.44% is due to position dependence [37]. To reduce this systematic uncertainty, it is necessary to calibrate the energy scale with a more detailed position dependence. As will be discussed later, spallation neutrons can be used to calibrate the position dependence of the energy scale in more detail. Also, for DSNB searches using the IBD reaction, it is important to check the uniformity and stability of the Gd concentration. These can be checked by using spallation neutrons.

In this chapter, firstly spallation neutrons and their characteristics are explained, then the method developed by us in this study to select and evaluate spallation neutrons is described.

6.2 Spallation neutron

6.2.1 Feature of spallation neutrons

When cosmic ray muons enter the SK detector, they can fragment nuclei in the water. This reaction is called spallation. Cosmic-ray muons mainly undergo spallation reactions with oxygen nuclei and produce neutrons and various types of radioisotopes. The neutrons produced in this reaction are called spallation neutrons. Spallation neutrons are thermalized in water within about 5 μs and captured by hydrogen or gadolinium. When captured by hydrogen, one γ ray of
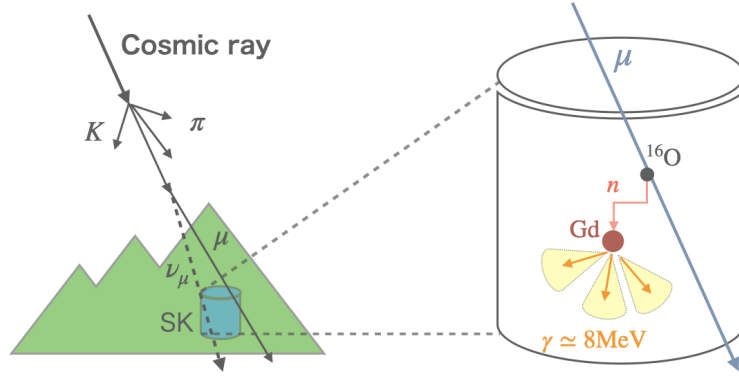
Figure 6.1: The neutron capture signal by gadolinium in the SK tank. Cosmic ray muons undergo a spallation reaction with oxygen atoms in the SK detector, and spallation neutrons are emitted. Spallation neutrons are then thermalized and captured by gadolinium, and finally a total of 8 MeV gamma rays are emitted.

2.2 MeV is emitted, and when captured by gadolinium, several γ rays of about 8 MeV in total are emitted. Figure 6.1 shows the schematic of spallation neutron signal in the SK tank.

Figure 6.2 shows the dt distribution of the spallation neutron signal. The dt is the time difference between the arrival of the cosmic ray muon and the neutron capture by gadolinium. The spallation neutron signal decreases exponentially with dt while the background is constant (Figure 6.2a). In this study, we utilize this feature to remove the background and extract only the signal. For this, the time window is divided into signal part time window ($[35, 235]\mu$s) and background part time window ($[335, 535]\mu$s) (Figure 6.12a). Then, the background part is subtracted from the signal part.

6.2.2 Advantages and disadvantages of spallation neutrons

There are two major advantages to conducting these studies using spallation neutrons. These events occur at a high rate and also throughout the entire detector volume. As described in Chapter 2, cosmic ray muons arrive at the SK detector at the rate of about 2Hz. It is expected that about 100,000 spallation neutrons are produced each day in the SK detector. Thanks to this high rate, we can obtain sufficient statistics in a short time. In addition, since cosmic ray muons enter the detector almost uniformly, spallation neutrons can also be detected almost uniformly in the detector. On the other hand, there are disadvantages, such as the low detected energy and close to the trigger threshold, which requires special
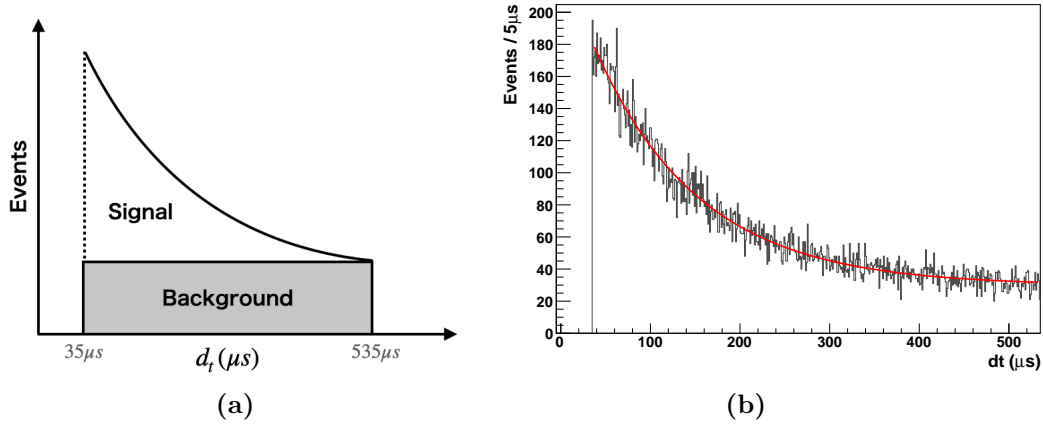
Figure 6.2: (a) The schematic of dt distribution. The spallation neutron signal decreases exponentially, but the background, mostly radioactive impurities, remains constant. (b) The dt distribution seen from data.

treatment to remove background and the need to consider the effects of pile-up. From these, it requires special treatment to evaluate energy correctly. Also, since gamma-rays are initially produced, reconstruction is more difficult than calibrations with electrons. The comparison of advantages and disadvantages with other energy calibrations are summarised in Figure 6.3.

In addition, spallation neutrons can check the stability of the gadolinium concentration in a short time and the uniformity of the gadolinium concentration throughout the entire detector.

6.2.3 Study using spallation neutron

In this study, using the spallation neutron signal, we develop the energy calibration method, monitor the stability of the detector response, and monitor the additional Gd-loading in 2022.

For the development of energy calibration method, it is possible to investigate the position dependence in the detector in more detail than with the other energy calibration methods. The aim is to develop a calibration with an accuracy of 0.5%, which is the same level of position dependence as the systematic uncertainty of solar neutrino measurement [37]. For the monitoring, it is possible to monitor the entire detector in a short time.

	Calibration	advantage	disadvantage
Calibration with instruments	Linac	• Injection of single energy electrons	• Number of people needed • Once or twice a year • The position is fixed
Calibration with instruments	DT calibration	• More positional flexibility than Linac • Possible to work with a relatively small number of people	• DTG itself interferes with the progress of Cherenkov light • The energy of the electrons is not fixed
Calibration with instruments	Ni	• Possible to work with a relatively small number of people	• The position is fixed
Cosmic ray induced	decay e	• Detection is possible throughout the entire SK tank • Analysis over the entire period is possible	• Few numbers of observed events • Long observation time required
Cosmic ray induced	^{16}N	• Detection is possible throughout the entire SK tank • Analysis over the entire period is possible • Investigation of directional dependence of energy scale is possible	• Few numbers of observed events (About 20 events per day) • Long observation time required
Cosmic ray induced	Spallation neutron	• Detection is possible throughout the entire SK tank • Analysis over the entire period is possible • A large number of observed events (About 100,000 events per day)	• Detect photon energy (difficult to reconstruct compared to electron) • Relatively low energy

Figure 6.3: Comparison of spallation neutrons with other energy calibration methods.
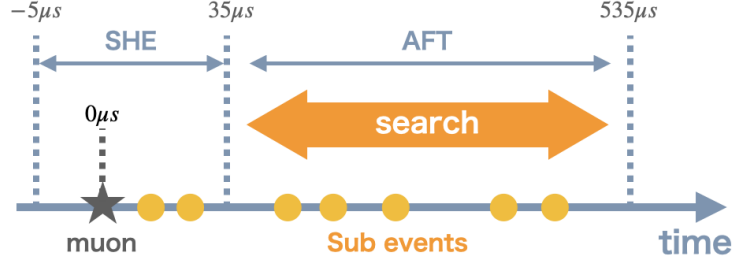
Figure 6.4: SHE trigger and AFT trigger opened when cosmic-ray muon enter the SK tank, and sub-events following muon. Signals that exceed the sub-trigger threshold ($N_{200} = 20$) every 1.3 μs time window are stored as sub-events.

6.3 Event selection of Spallation neutron

6.3.1 Triggers for spallation neutron event search

When a cosmic ray muon passes through the SK detector, SHE trigger ([-5, 35]μs) is issued, and then AFT trigger ([35, 535]μs) is issued. Sub-events are searched by applying sub-trigger (off-line screening triggers for low-energy events) to data stored by SHE trigger and AFT trigger (Figure 6.4). The sub-trigger is applied to SHE and AFT triggers and sub-events are searched by this sub-trigger. If there are 20 hits within 200 ns, the sub-trigger is applied and 1.3μs before and after that is saved as the sub-event. Sub-event is the candidate for neutron capture signals by gadolinium.

6.3.2 Muon selection

The conditions for the event selection of cosmic ray muon are the following two points.

- Both OD and SHE triggers are issued.

- The total integrated charge of the signal observed in the ID $Q_\mu > 10,000$ p.e.

Cosmic ray muons emit Cherenkov light immediately after entering the detector. After PMTs in the outer detector (OD) detect the light and the OD trigger is issued, the cosmic ray muon loses several GeV of energy in the inner detector (ID) and emits Cherenkov light, which is detected by PMTs in the ID and the SHE trigger is issued.

Also, it is required that the total integral charge observed in the ID, Q_μ, to be $Q_\mu > 10,000$ p.e. The distribution of Q_μ is shown in Figure 6.5.
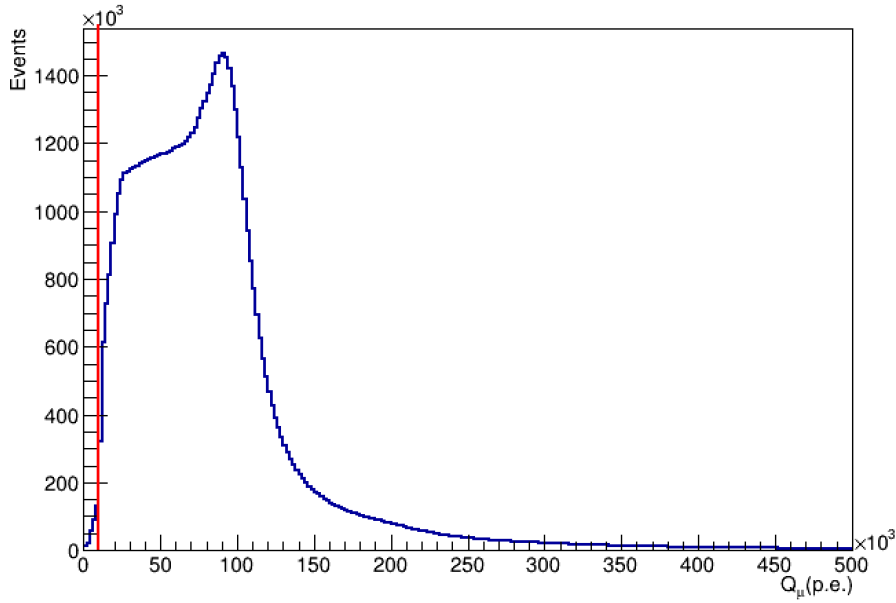
Figure 6.5: The distribution of Q_μ. Q_μ is the total amount of Cherenkov light detected by ID PMTs. The red line indicates the position of $Q_\mu = 10,000$ p.e., the events to the right of the red line are selected.

6.3.3 Neutron selection

In this section, the event selection of neutron captures by Gadolinium is described.

Fiducial volume

PMTs are installed on the wall of the SK tank and the noise related to PMTs increases near the wall. Therefore, the area more than 2 m away from the walls of the ID is taken as the fiducial volume.

Time window

The neutron capture signal by gadolinium is searched for in the AFT trigger. This is to remove the signal of muon decay electrons and PMT afterpulse. It has been found that the PMTs attached to the SK tank generate the afterpulse about 10–20 μs after receiving the main pulse [46].

Reconstruction quality

The main background in the spallation neutron signal is radioactive impurities in the SK tank. These backgrounds are constantly occurring near the wall of the tank. These reconstruction quality cuts remove the events near the wall accidentally reconstructed in the fiducial volume. The parameters g_{vtx} and g_{dir} are used to assure the good accuracy of the reconstruction (Refer to chapter 3). The distributions of g_{vtx} and g_{dir} are shown in Figure 6.6b and Figure 6.7b, respectively. These two distributions are obtained by subtracting the background part ($[335, 535]\mu$s) from the signal part ($[35, 235]\mu$s) (Figure 6.6a and Figure 6.7a). Only the cut that selects the fiducial volume is applied to the signal part and the background part. Looking at Figure 6.6b, peaks can be seen even in the range where the value of g_{vtx} is low. These are events in which background events are mistaken for spallation neutron signals. The range of $g_{vtx} < 0.40$ is excluded. g_{dir} is also set to condition $g_{dir} > 0.40$ to select events with high reconstruction accuracy.

Therefore the conditions for the parameter g_{vtx} and g_{dir} are set,

$$(g_{vtx} > 0.40) \cap (g_{dir} < 0.40). \tag{6.1}$$
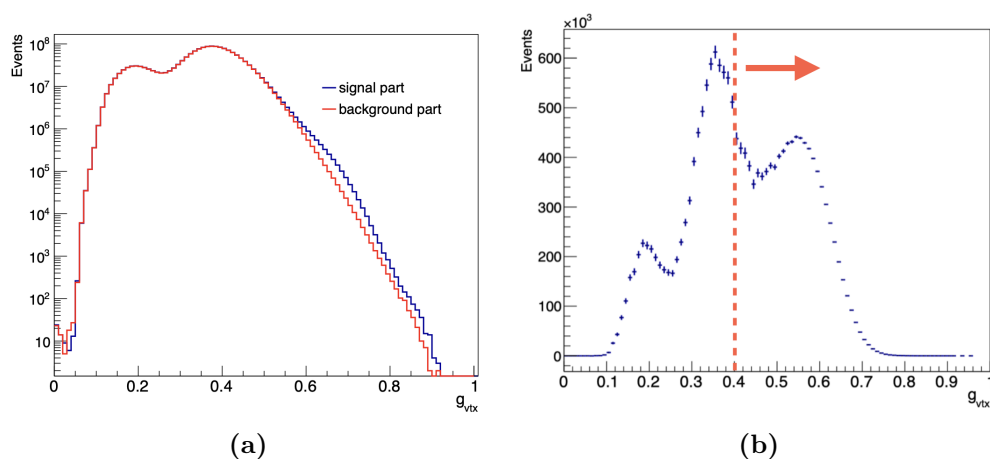
Figure 6.6: (a) The g_{vtx} distribution divided by the time window. The blue line represents the signal part window ($[35, 235]\mu$s), and the red line represents the background part window($[335, 535]\mu$s). Only the cut that selects the fiducial volume is applied to the signal part and the background part. (b) The extracted signal of the goodness of event point reconstruction g_{vtx}. The value of g_{vtx} closer to 1 indicates better reconstruction. The events of the low g_{vtx} value are that spallation neutrons and background events occur simultaneously or background events are mistaken for spallation neutron signals. The right side of the red dotted line (greater than 0.4) is selected.

Distance between muon track and neutron capture vertex L_t

(a)   **(b)**
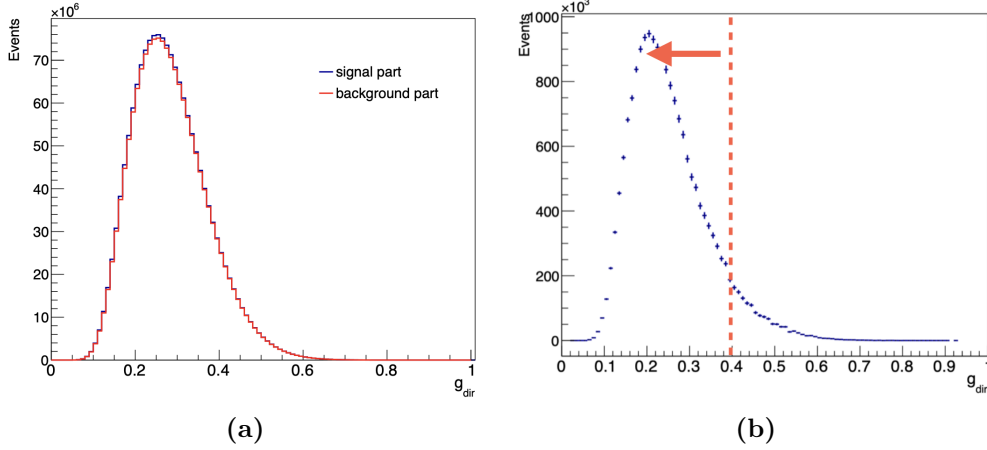
Figure 6.7: (a) The g_{dir} distribution divided by the time window. The blue line represents the signal part window ([35, 235]μs), and the red line represents the background part window([335, 535]μs). Only the cut that selects the fiducial volume is applied to the signal part and the background part. (b) The extracted signal of the goodness of direction reconstruction g_{dir}. The value of g_{dir} closer to 0 indicates better reconstruction. The left side of the red dotted line (less than 0.4) is selected.

To select the signal of neutron captured by gadolinium, we consider the distance between muon track and point of neutron capture event L_t as shown in Figure 6.8. The spallation neutron signal occurs close to the muon track and applying this cut eliminates background not related to muon. The L_t distribution of events from neutron captured by gadolinium is shown in Figure 6.9b. The distribution is obtained by subtracting the background part ([335, 535]μs) from the signal part ([35, 235]μs) (Figure 6.9a). The cuts of the fiducial volume and the reconstruction quality are applied to the signal part and the background part. Most of the events from neutron captured by gadolinium exist within L_t of 300 cm. We set the condition L_t,

$$L_t < 300 \, \text{cm} \tag{6.2}$$

Reconstructed event time

We set a condition for the reconstructed time t_0,

$$t_0 = [0.7, 1.0] \, \mu s \tag{6.3}$$

If there are multiple events in a trigger, the events cannot be reconstructed well, and the reconstructed time is also shifted. This condition is to reduce this effect.
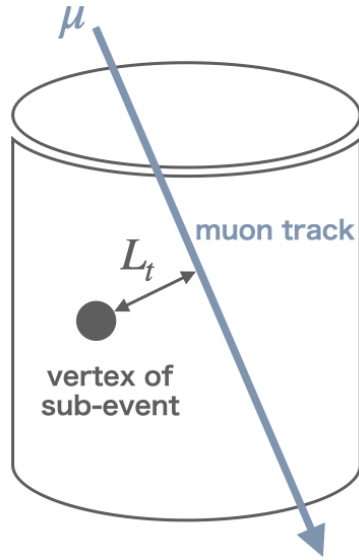
Figure 6.8: Distance between reconstructed point of neutron capture event and muon track.

(a) (b)
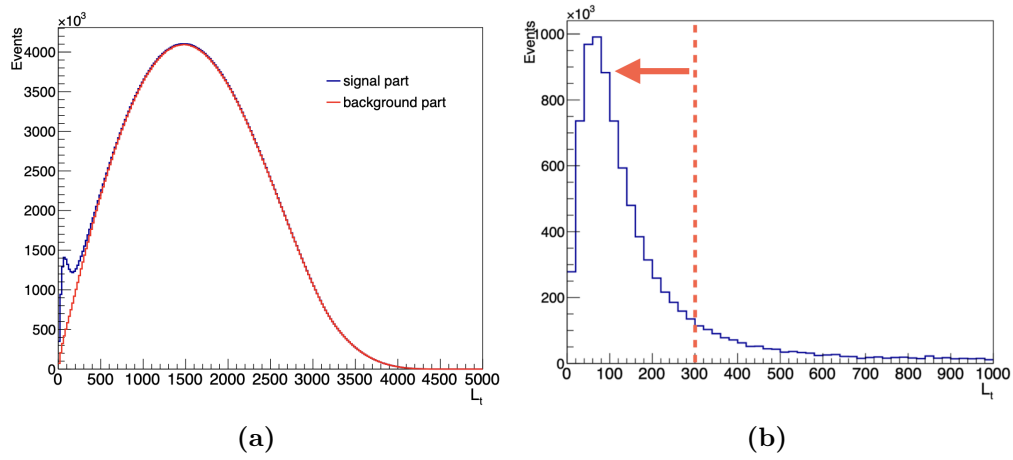
Figure 6.9: (a) The L_t distribution divided by the time window. The blue line represents the signal part window ($[35, 235]\mu$s), and the red line represents the background part window($[335, 535]\mu$s). The cuts of the fiducial volume and the reconstruction quality are applied to the signal part and the background part.(b) The L_t distribution of the extracted signal from neutron capture of gadolinium. The left side of the red dotted line ($L_t < 300$cm) is selected.
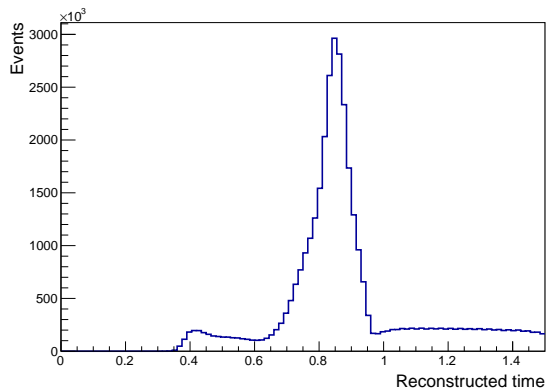
Figure 6.10: The distribution of reconstructed time t_0. The histogram contains the fiducial volume cut, reconstruction quality cut and distance cut described above. Events in the range $0.7 < t_0 < 1.0\,\mu s$ are selected. The few events that exist outside this range are events that occur at the same time as the neutron signal and shift the reconstruction time. It is eliminated to reduce the effect of multiplicity.

When the time is reconstructed successfully, the reconstruction time value of the event is expected to be around $0.9\ \mu$s. The reconstructed time distribution is shown in Figure 6.10. The histogram contains the fiducial volume cut, reconstruction quality cut and distance cut described above.

6.4 Study of pile-up effect

Pile-up occurs due to the multiple spallation neutrons generated from one cosmic muon. Pile-up has a large effect on the evaluation of energy and must be considered when evaluating the energy of spallation neutrons. In this section, first, the method to evaluate the mean N_{50}, which is used to evaluate the energy, is described. The effect of pile-up due to multiplicity is then investigated. Finally, the signal of the Am/Be neutron source, which is less affected by pile-up, is compared with spallation neutron signal to check the consistency.

6.4.1 Evaluation of mean N_{50}

N_{50} is the number of PMT hits within a 50ns interval. In the low energy range, where in most cases one photoelectron is detected by one PMT, N_{50} is used as a parameter to describe the energy. The N_{50} distribution of the spallation neutrons derived from the selection conditions in Section 6.3.3 is shown in Figure 6.11. This
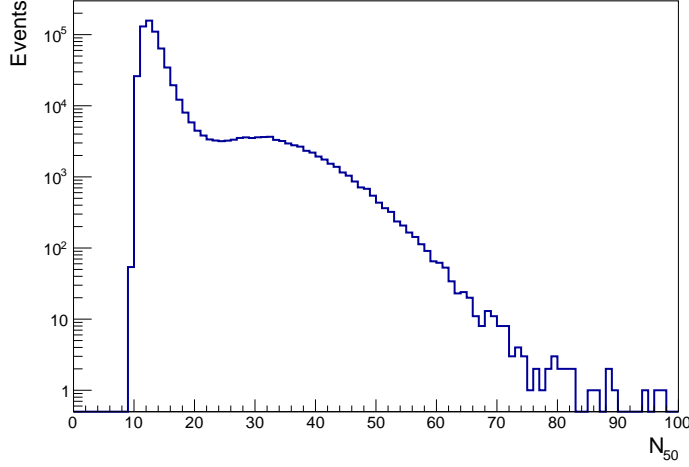
Figure 6.11: The N_{50} distribution.

is the distribution of events that remain after applying the event selection cuts. The sharp peak at the lower N_{50} on the left represents background events, and the broader peak at N_{50} between 30 and 40 represents the spallation neutron events. The spallation neutron signal events are extracted by subtracting the background part ($[335, 535]\mu$s) from the signal part ($[35, 235]\mu$s) (Figure 6.12a). The N_{50} distribution of the extracted spallation neutron signal is fitted to derive the mean N_{50}. The fitting function is Gaussian,

$$f(x) = a\exp\left(-\frac{(x-\mu)^2}{2\sigma^2}\right) \tag{6.4}$$

where μ is the mean and σ is the standard deviation. We repeat the fit three times with different ranges to increase the accuracy. The fit range is shown in Table 6.1. The obtained μ is regarded as the mean N_{50}. (Figure 6.12b).

Table 6.1: Number of fits and fit range

Number of times	Range of fit
1st	$20 < N_{50} < 70$
2nd	$[\mu - 0.4 \times \sigma, \ \mu + 1.5 \times \sigma]$
3rd	$[\mu - 0.7 \times \sigma, \ \mu + 1.5 \times \sigma]$
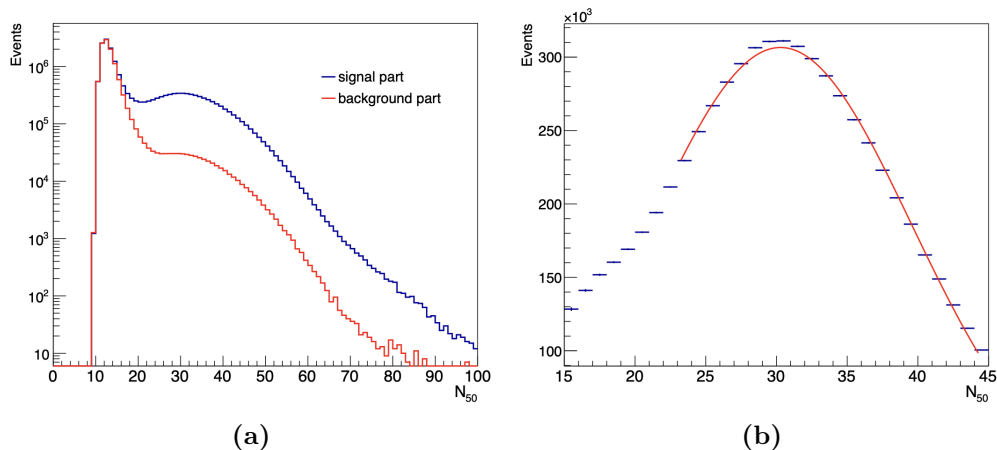
Figure 6.12: (a) The N_{50} distribution divided by window. The blue line represents the signal part window ($[35, 235]\mu$s), and the red line represents the background part window($[335, 535]\mu$s). (b) The extracted spallation neutron signal and fit function.

6.4.2 Neutron multiplicity

For one cosmic ray muon pass through the SK tank, between one and about 100 spallation neutrons are produced (Figure 6.13). The number of spallation neutrons produced is called neutron multiplicity, and it is found that the larger the neutron multiplicity, the larger the mean N_{50} value (Figure 6.14). This is due to the pile-up. When multiple events occurred in a single trigger time window, the one with the greater number of hits is more likely to be selected as the signal (Figure 6.15). Therefore, the greater the neutron multiplicity, the more likely it is that signals with greater energy will be selected, and the mean N_{50} value will also increase.

In addition, it is known that the shape of the dt distribution changes due to the effect of neutron multiplicity, and the time constant changes. If an event is found in which more than 20 PMT hits are clustered in 200 ns time width, the PMT hit information for the surrounding 1.3 μs is stored by the sub-trigger. Therefore, if one sub-event is stored, 1.3 μs around it becomes a dead time, and if the events overlap within 1.3 μs, the event will not be detected. Due to this dead time, some signals are not detected and the number of events decreases in regions with small value of dt, so the shape of the dt distribution becomes smoother than it should be.
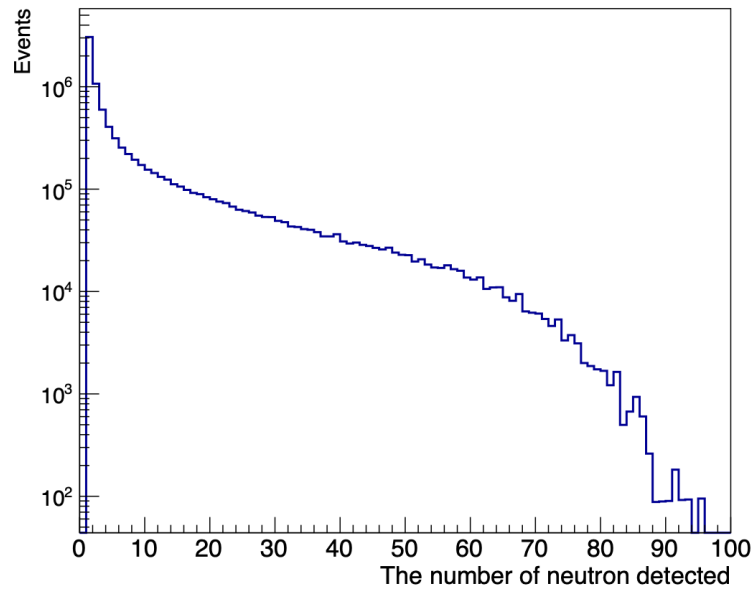
Figure 6.13: The number of spallation neutrons detected by one cosmic ray muon
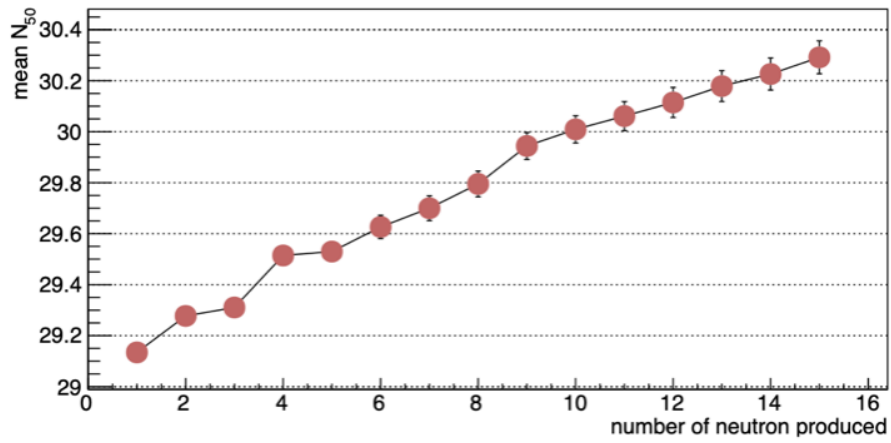
Figure 6.14: Relation between mean N_{50} and neutron multiplicity.
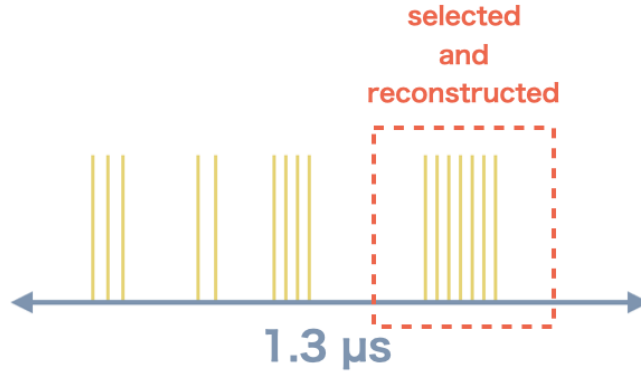
Figure 6.15: The illustration of the selection of the largest signal by sub-trigger. The light blue arrow represents the time width of the sub-trigger (1.3 μs) and the yellow line represents the number of PMT hits. If multiple events occur within one sub-trigger, the signal with the highest number of hits is selected and reconstructed.

6.4.3 Comparison with Am/Be data

In this section, we test the consistency of the spallation neutron signal and Am/Be neutron source signal. Multiple neutrons can be produced by a spallation process and it can affect reconstruction. Therefore it is important to confirm the consistency with the Am/Be source which only one neutron is produced at a time. We will first explain the event selection of Am/Be neutron signal and spalltion neutron signal, and then compare Am/Be neutron signal and spallation neutron signal.

As mentioned above, spallation neutron signals have the effect of neutron multiplicity. For a more accurate evaluation of spallation neutron signal, it is necessary to select a signal with the small multiplicity effect. The effect of the multiplicity of spallation neutrons on the mean N_{50} is shown in Figure 6.16. The top figure shows the variation of the mean N_{50} with neutron multiplicity, and the bottom figure shows the deviation of the mean N_{50} from one detected neutron number where we expect no pile-up effect. It is found that when the number of detected spallation neutrons is up to three, the deviation is within 0.5% compared to when the number of spallation neutrons detected is one. The effect of the pile-up is small up to three neutrons, so the data of 1-3 detected neutrons put together is compared with the Am/Be data in order to increase the number of statistics. Four samples are made with the detected number of spallation neutrons as shown in Table 6.2 and compare with the Am/Be source.

Neutron signal selection
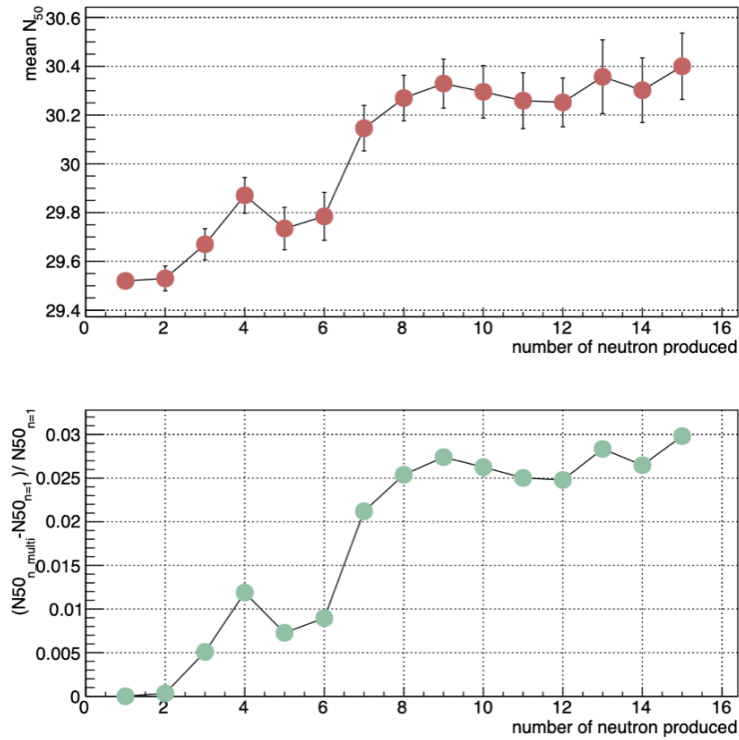
Figure 6.16: The effect of the multiplicity of spallation neutrons on the mean N_{50}. Up to 3 productions, the deviation from 1 is suppressed to 0.5%

Table 6.2: Spallation neutron detection number compared to Am/Be

Display name	Number of detected neutrons
All	Any
n:1	1
n:1-3	1-3
n:2-10	2-10

The Am/Be neutron source emits only one neutron at a time, so confirming that the pile-up effect of the spallation neutrons is negligible after the selection. In order to compare the Am/Be neutron signal and the spallation neutron signal, the event selection conditions are matched as much as possible. Each condition item is described below.

- Sub-trigger threshold

  The sub-trigger thresholds for Am/Be and spallation neutron is adjusted to 20.

- Reconstruction quality

  As mentioned above, both the Am/Be neutron signal and the spallation neutron signal are analyzed under the condition of

  $$(g_{vtx} > 0.40) \cap (g_{dir} < 0.40). \tag{6.5}$$

- Reconstructed time

  The reconstructed time condition to the selection condition of the spallation neutron signal is analyzed under the condition of,

  $$t_0 = [0.7, 1.0] \, \mu s. \tag{6.6}$$

- Time window

  Selected from within the AFT trigger [35, 535] μs

- Position and Region

  Am/Be neutrons are produced at the limited source positions, whereas spallation neutrons can be detected throughout the entire SK detector. Considering the position dependence in the detector, the detection region for spallation neutrons was adjusted to that for Am/Be neutrons. The region is $d < 400$cm centred on three points (x,y,z) = (-389, -70.7, -1200)cm, (-389, -70.7, 0)cm and (-389, -70.7, 1200)cm, where d is the distance between the position where the Am/Be source is placed and the reconstructed event point.

- Date

  The spallation neutron data was summed over runs of about 5 months so that the statistical error of the spallation neutron signal was at least the same as that of the Am/Be neutron signal. Also, taking into account the time dependence within the detector, two periods were used for comparison

Table 6.3: Data used to compare Am/Be and spallation neutrons

Spallation neutron	Am/Be
2021/01/22 - 2021/07/19 (First period)	2021/05/14 #85828(-12m) #85830(0m) #85832(12m) 2021/05/11 #85877(-12m) #85879(0m) #85881(12m) 2021/06/30 #86004(-12m) #86006(0m) #86008(12m)
2021/08/17 - 2022/02/11 (Second period)	2021/09/22 #86291(-12m) #86293(0m) #86295(12m) 2021/11/26 #86439(-12m) #86441(0m) #86443(12m) 2021/12/23 #86504(-12m) #86506(0m) #86508(12m)

with Am/Be. For Am/Be, three runs within one period of spallation neutron were selected for every three points at z = -12 m, 0 m and 12 m per one period. The used data is summarized in Table 6.3.

In order to evaluate the same signal in Am/Be as spallation neutrons, the time window of AFT trigger is divided into signal part time window ($[35, 235]\mu$s) and background part time window ($[335, 535]\mu$s), and the background is subtracted from the signal. In addition, fitting is applied to the N_{50} distribution of Am/Be in the same way as spallation neutron, and the value of mean N_{50} is derived.

Comparison of Am/Be neutron signal and spallation neutron signal

The result of comparing the mean N_{50} derived as above is shown in Figure 6.17. Figure 6.17a shows the N_{50} comparison between Am/Be source and spallation neutrons in the first period, and Figure 6.17b shows the mean N_{50} comparison between Am/Be source and spallation neutrons in the second period. Figure 6.17c shows the deviation of N_{50} between Am/Be source and spallation neutrons in the first period, and Figure 6.17d shows the deviation of N_{50} between Am/Be source and spallation neutrons in the second period. From Figure 6.17c and Figure 6.17d, it can be seen that the spallation neutron signal for n:1-3 agrees with the Am/Be neutron signal within $\pm2\%$. Also, a χ^2 test was performed at six positions to check how much the n:1-3 signal and Am/Be deviated from each other. The χ^2 value with a NDF of 6 is 3.29 and ap-value is 0.78. Therefore, there is no significant deviation between the spallation neutron signal for n:1-3 and AmBe source data. It is found that the signal for n: 1-3 is less affected by pile-up.

Table 6.4: The summary of the conditions for the event selection of neutron to use the analysis.

Type of condition	Condition
Time window	AFT trigger : $[+35, +535]\mu$s
Reconstruction quality	$(g_{vtx} > 0.40) \cap (g_{dir} < 0.40)$
Length of muon track and point of neutron capture event	$L_t < 300$cm
Reconstructed event time	$[0.7, 1.0]\mu$s
The number of neutron detected	n:1-3
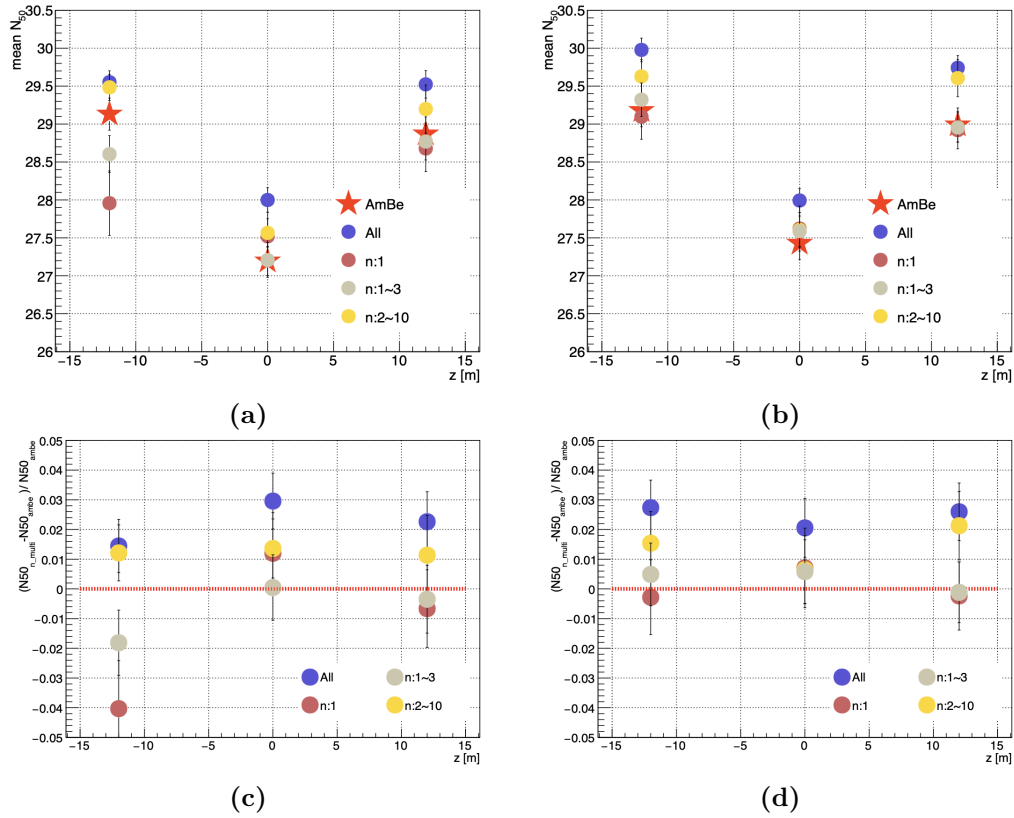
Figure 6.17: Results of comparison between Am/Be neutron and spallation neutron. The upper figures show the comparison of mean N_{50}, and the lower figures show the deviation from the AmBe source. The left side is the first period and the right side is the second period. Red star represents Am/Be, and round dots represent the number of spallation neutrons detected in each (Blue: All, Red: n:1, Gray: n:1~3, Yellow: n: 2~10).

Chapter 7

Detector performance monitoring using spallation neutrons

Spallation neutrons can be used to monitor the stability of the detector response and the uniformity of the Gd concentration. In this chapter, first, the stability and uniformity of the detector response and Gd concentration are evaluated, and then the results of the monitoring of additional Gd-loading in 2022 are described.

7.1 Stability

The stability of the detector response of SK-VI data is monitored in two ways: evaluating the energy using the mean N_{eff} and evaluating the gadolinium concentration using the neutron capture time constant.

7.1.1 Evaluation of stability using energy with mean N_{eff}

In this section, the stability of the detector response is confirmed using the mean N_{eff}. The method to evaluate mean N_{eff} is the same as that of mean N_{eff} described in section 6.4.1.

The data from September 10, 2020, when SK-VI started, to March 12, 2022, before the additional Gd-loading starts, is used for this study. This period is divided into 30-day intervals. Also, the sample is divided into nine parts using the reconstructed vertex positions for each period as shown in Figure 7.1a. Then the fitting is performed to evaluate mean N_{eff} in each area (Figure 7.1b).

The mean N_{eff} value for each area and for each 30-day period result is shown in Figure 7.2a. Also, the stability of the whole area of the detector is shown in Figure 7.2b. This is derived from the difference between the average of the mean N_{eff} of the nine areas for one period and the average for the whole period divided
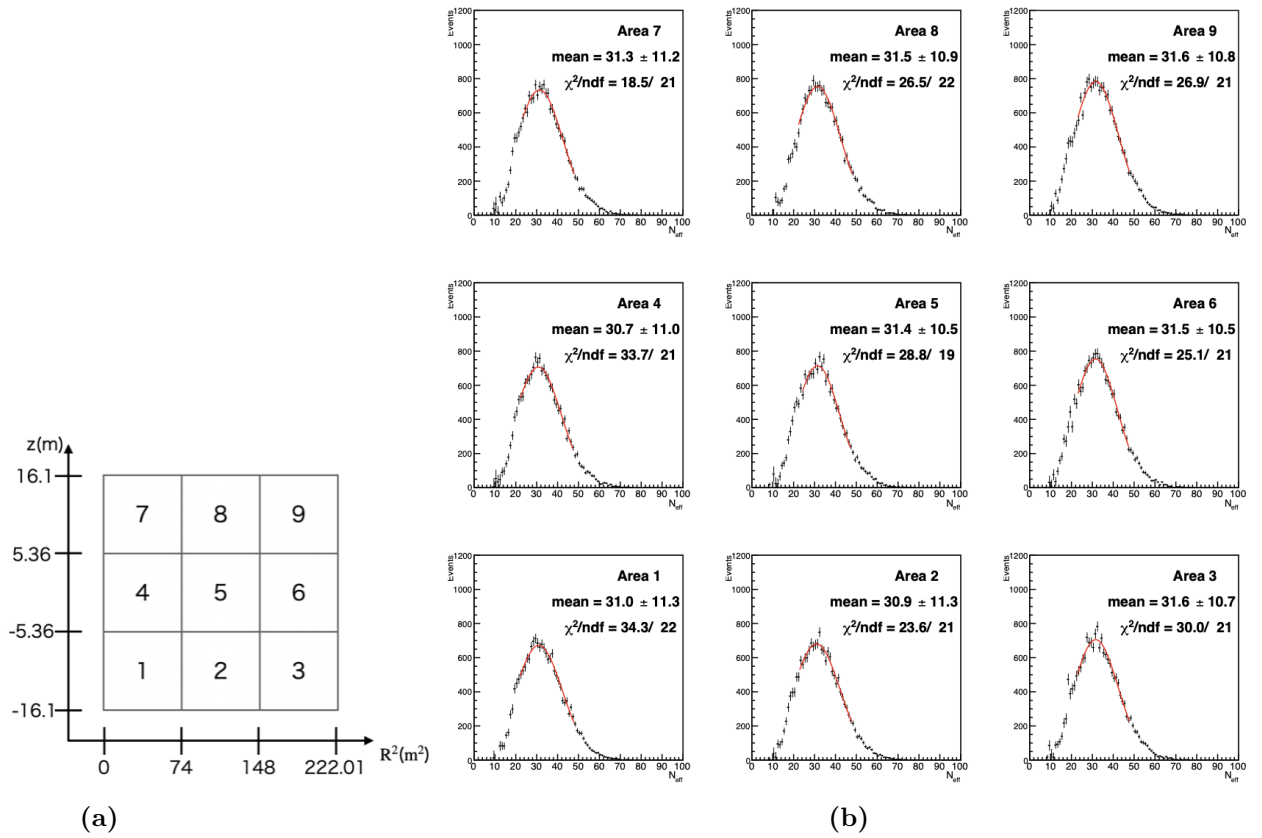
Figure 7.1: (a)Schematic diagram of 9-division detector. (b)The derivation of mean N_{eff} by performing fittings in each area.

by the average for the whole period, written in the equation as follows.

$$\text{deviation} = \frac{(\text{mean } N_{\text{eff}})_{\text{one period}}^{\text{ave}} - (\text{mean } N_{\text{eff}})_{\text{all period}}^{\text{ave}}}{(\text{mean } N_{\text{eff}})_{\text{all period}}^{\text{ave}}} \quad (7.1)$$

It is found to be stable at $\pm 0.5\%$ in most areas.

(a) Stability in each area

(b) Stability of the entire detector
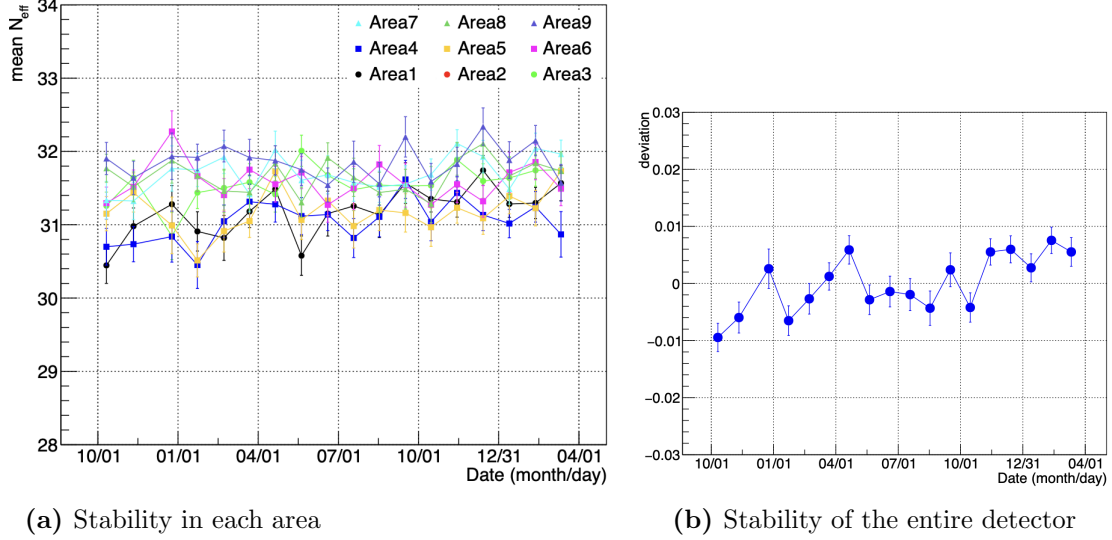
Figure 7.2: Stability of the detector response monitored using mean N_{eff}.

7.1.2 Evaluation of stability using Gd concentration with the time constant

The stability and the uniformity of the Gd concentration is also evaluated using the time constant with the same period and detector division as using mean N_{eff}. The time constant is derived by fitting the dt distribution with a function,

$$f(dt) = a\exp\left(-\frac{dt}{\tau_{\text{cap}}}\right) + b \quad (7.2)$$

where a, b, and τ_{cap} are values determined by this fitting, a is the normalization constant for the number of signal events. b is the constant that determines the number of background events, and τ_{cap} is the time constant for neutron capture by gadolinium. The values of a, b, and τ_{cap} are obtained by fitting at $dt \in [35, 535]$ μs. Figure 7.3 shows the results of fitting the neutron capture timing distributions for one period (about 30 days).

The stability of the time constant from September 10, 2020, to March 12, 2022, is shown in Figure 7.4a. Time constants are between 125 μs to 140 μs in any area.
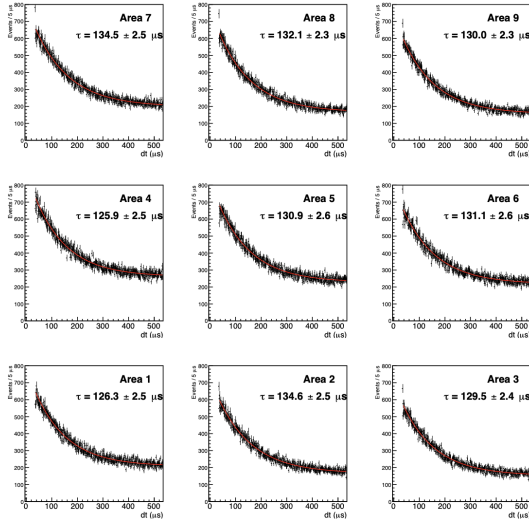
Figure 7.3: The derivation of the time constant τ_{cap} by performing fittings in each are.

This shows that the Gd concentration in the detector is uniform. For the entire detector area, the time constant is stable within $\pm 2\%$ (Figure 7.4b). This shows that the Gd concentration in the detector is also stable within $\pm 2\%$.

7.2 Monitor of additional Gd-loading in 2022

Additional Gd-loading was conducted before the summer of 2022 and the SK phase shifted from SK-VI to SK-VII. This loading took place from 1st June to 5th July 2022 and a total of 27.265 tonnes of $Gd_2(SO_4)_3 \cdot 8H_2O$ was dissolved. In this section, we reporte the state of the Gd concentration in the detector during Gd-loading using the number of spallation neutron signal and the neutron capture time constant with gadolinium.

7.2.1 Event selection of Spallation neutron for Gd-loading monitor

For the Gd-loading monitor, it is more important to monitor the number of neutron captures on Gd than for to evaluate energy scale precisely. So the selection conditions for the event of spallation neutrons used in the Gd-loading monitor differ a little from the event selection described in Section 6.3.3.

- Time window
  The dt distribution of the spallation neutron signal decreases exponentially.

(a) Stability in each area

(b) Stability of the entire detector
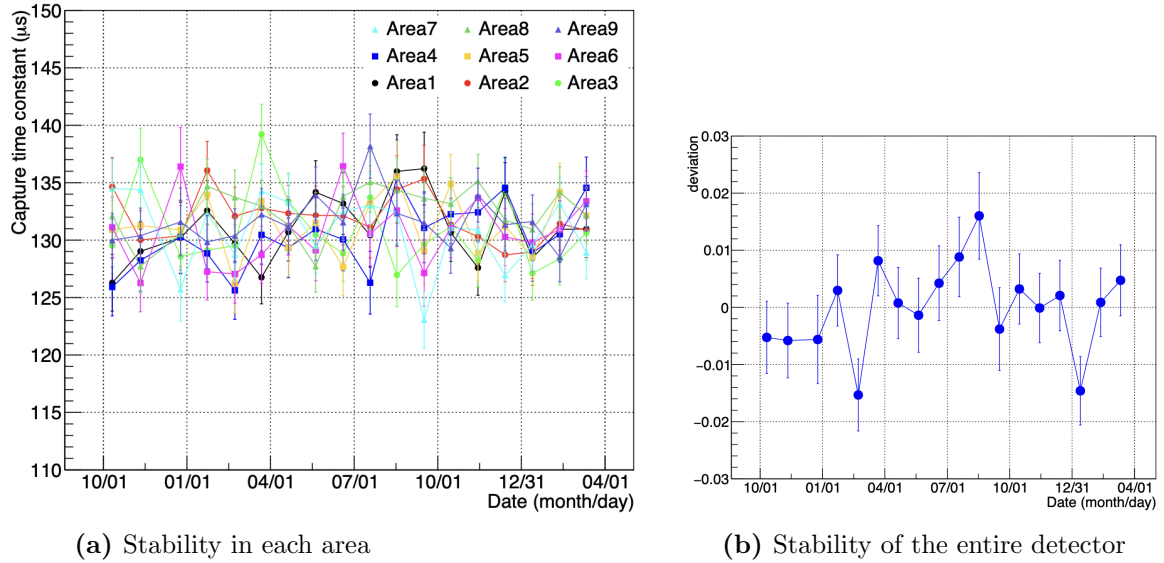
Figure 7.4: Stability of the detector response monitored using the time constant.

As will be described later, the higher the Gd concentration, the smaller the time constant. When the concentration increases from about 0.01% to 0.03%, the spallation neutron signal is more prominent within 35 μs before the AFT trigger is issued (Figure 7.5). As such, the events within the SHE trigger [-5, 35]μs were also used. However, as shown in Figure 7.6, there was a problem that the event before 20 μs in the SHE trigger was not properly detected. It is known that afterpulses occur at a certain rate with dt in the range of 10-20 μs [46]. It is possible that after-pulse affected the event reconstruction. Considering that, the time window used in Gd-loading is [20, 35]μs.

- Reconstructed time and the number of neutron detected
  To obtain more spallation neutron signals, the conditions of reconstructed time and the number of neutrons detected are not used.

7.2.2 Monitor by number of spallation neutron signal

Figure 7.7 shows the distibution of spallation neutron vertex. Each figure shows the state inside the detector up to the date indicated on the top of the figure. As mentioned in Chapter 2, water containing additional Gd is inserted from the bottom of the detector. The intensity of the Gd concentration appears in the contrast of the figure, and as the days pass, the concentration increases from the bottom of the detector, and on July 4th, it was evaluated that the concentration in the detector became constant at 0.03%.

96
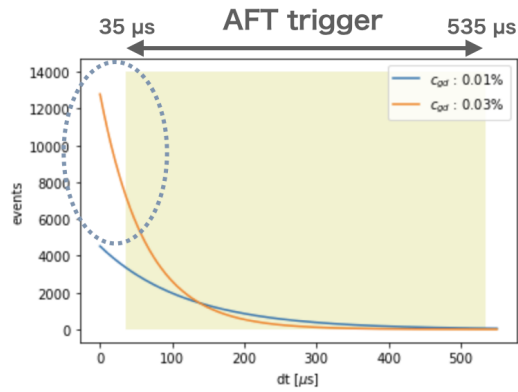
Figure 7.5: Schematic diagram of the difference in dt distribution for Gd concentrations of approximately 0.01% and 0.03%. The blue line represents 0.01% Gd concentration, and the orange line represents 0.03%. The yellow-green area represents the AFT trigger, and it can be seen that the increase in the number of spallation neutron signals is greater in the time before the AFT trigger.
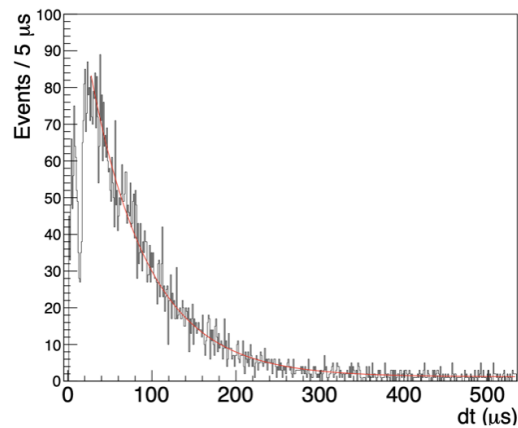
Figure 7.6: The dt distribution including SHE trigger. The number of events should increase exponentially as the capture time decreases, but the number of events decreases before 20 μs. From this, it can be seen that for some reason events are not selected well before 20 μs.
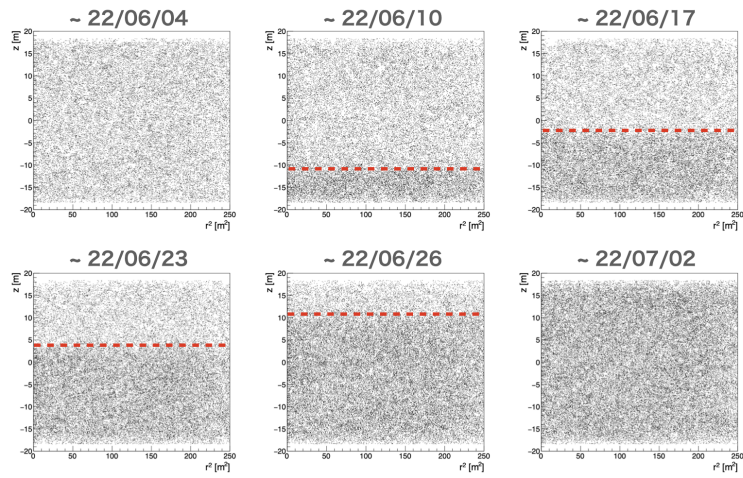
Figure 7.7: The distibution of spallation neutron vertex. The horizontal axis represents the square of the radius of the detector, the vertical axis represents the height, and the plot represents the inside of the detector. The difference of the contrast represents the difference in the number of events, and the figure shows that the Gd concentration is becoming more concentrated from the bottom of the tank by day. The Gd concentration in the tank became almost constant on July 2, 2022.

7.2.3 Monitor by neutron capture time constant

Next, the Gd-loading state is monitored using the neutron capture time constant. It is expected that the time constant is approximately 120 μs at a concentration of 0.01% and 63 μs at a concentration of 0.03%. The time constants were derived as follows. First the sample was divided into 10 parts using the reconstructed z vertex position, and then the time constant of each area was obtained by fitting the dt distribution of each area. Figure 7.8 shows the result of evaluating it about every 3 days. On 4 June (purple line), the time constant was approximately 120 μs across the detector, but the time constant gradually decreased from the bottom of the tank and on 5 July (light blue) the concentration became constant throughout the detector at around 63 μs.

The monitoring of the Gd-loading was carried out successfully. By using the number of spallation neutron signal and the neutron capture time constant with gadolinium, it could be evaluated that Gd concentration gradually increased from the bottom of the tank and finally the Gd concentration remained constant at the time constant expected value of about 63 μs.
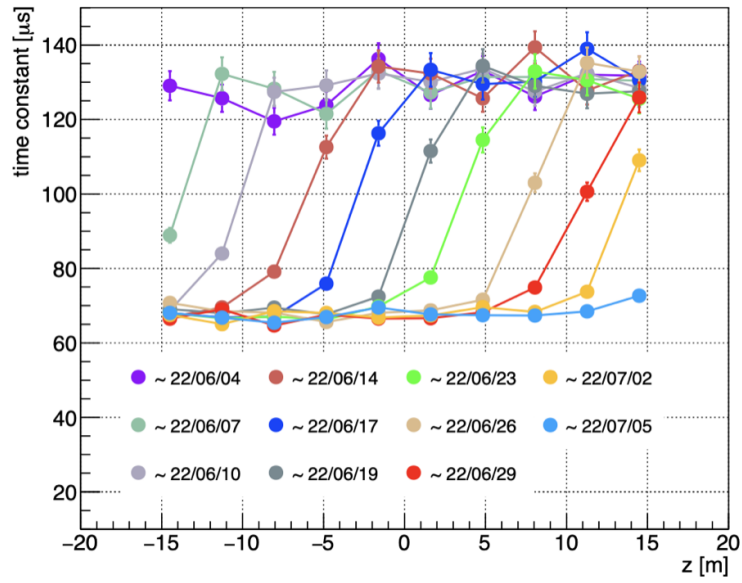
Figure 7.8: The state of Gd-loading using the neutron capture time constant of gadolinium.The horizontal axis represents the z direction of the detector, and the vertical axis represents the time constant. On June 4th (purple line), the time constant was about 130μs throughout the detector, but on July 5th (light blue), the concentration became constant around 65μs.

Chapter 8

Energy scale calibration with spallation neutrons

In this chapter, the energy calibration using spallation neutrons is discussed. It is important for the energy calibration to evaluate the position dependence. Firstly, the position dependence of $\text{Gd}(n, \gamma)$ signal is evaluated by comparing with that of electrons with MC simulation. Then, the $\text{Gd}(n, \gamma)$ signals of data and MC simulation are compared.

8.1 Comparison of position dependence of neutron and electron signals by MC simulation

The primary signals for solar neutrinos and DSNB are electrons and positrons. Therefore, it is important to accurately reconstruct electron energy. In SK, there are calibrations such as LINAC and DT calibration that inject electrons, but the position of the injections is fixed, making a more detailed evaluation of position dependence difficult (Chapter 5). We consider the correction for position dependence using spallation neutrons instead of electrons. Spallation neutron signals have the advantage that they can be observed throughout the entire detector at high rates, but they also have the disadvantage that gamma cascades are detected and the detected energy is low and close to the trigger threshold (Chapter 6). In this section, using the MC simulation, comparison of the deviations in the position dependence of N_{eff} of the electron and $\text{Gd}(n, \gamma)$ signals is described in order to see if neutrons can be used to evaluate the energy scale of electrons.

8.1.1 Evaluation of the electron and neutron signal with MC simulation

The Geant4-based MC simulation package called SKG4 [47] is used in this simulation. It can simulate particle interactions and responses of the SK detector. The output of SKG4 contains the same format as real data, so it can be analyzed in the same way as real data.

Procedure

1. Generate particles uniformly throughout the detector.
2. Add realistic noise to the resulting output.
3. Apply the sub-trigger to the noise added output and save the sub-events.
4. Perform the event reconstruction (Sec. 5.1).

Simuated initial particles

- neutron
  - The energy is set to 200keV. After neutron thermalization, neutron is captured by Gd and gamma rays are emitted. The ANNRI-Gd model is adopted as the model for $Gd(n, \gamma)$ [48].
- electron
  - The energy is set to 10MeV. This is a typical energy of electrons generated from solar neutrino reactions observed by SK.

Evaluation of position dependence

1. The fiducial volume cut and the event quality cut are adapted (Sec. 6.3.3) The distribution of N_{50} of neutron signal after these cuts is shown in Figure 8.1.
2. The position dependence is evaluated in five regions for each of r^2 and z like Figure 8.2. The mean N_{50} and mean N_{eff} are estimated in each area by fitting (Sec. 6.4.1). The fitting results of electron and neutron are shown in Appendix C.
3. By comparing the mean N_{50} and mean N_{eff} in each area, The position dependence of N_{50} and N_{eff} is evaluated. N_{50} has the tendency that the closer the distance from the wall where the PMT is installed, the greater the detected energy. This is because the position dependence in the detector is largely related to the attenuation of water.

The mean N_{eff} is used to evaluate the position dependence of the energy after reconstruction. The deviation is calculated by the following equation,

$$\text{deviation}_i = \frac{(\text{mean } N_{\text{eff}})_i - (\text{mean } N_{\text{eff}})_{\text{ave}}}{(\text{mean } N_{\text{eff}})_{\text{ave}}} \tag{8.1}$$

where i represents the index for each area.

(a) electron
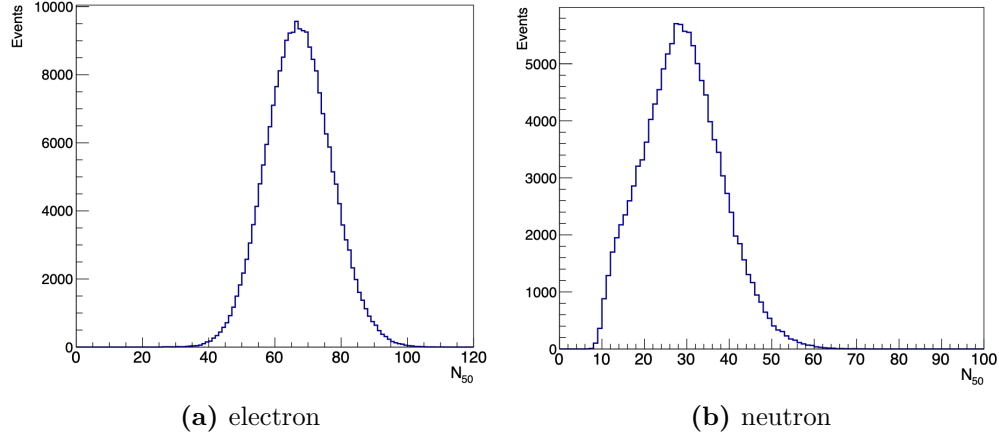
(b) neutron

Figure 8.1: The N_{50} distribution obtained by MC simulation. The histogram contains the fiducial volume cut, the reconstruction quality cut. (a) electron. (b) neutron.

(a)

(b)
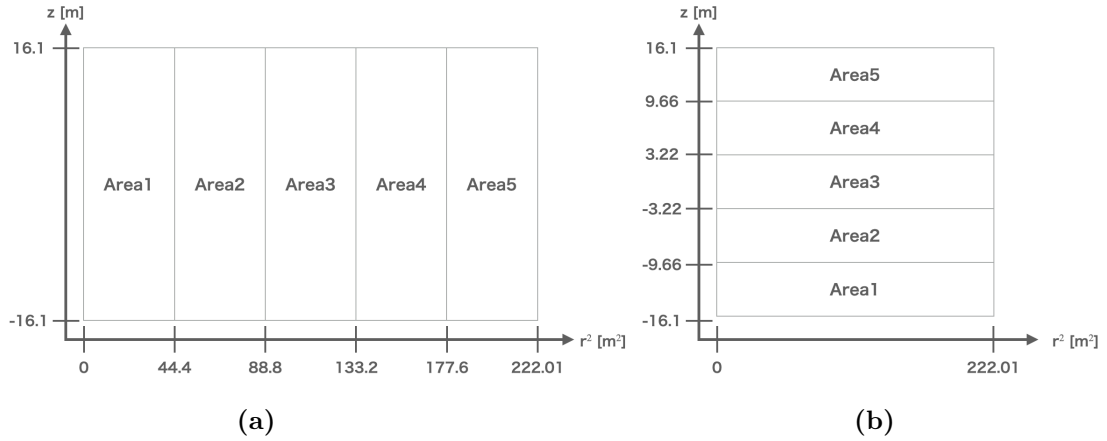
Figure 8.2: (a)The detector divided into five in r^2 direction. (b)The detector divided into five in z direction.

103

8.1.2 Results of the event reconstruction

For electron, the position dependence of N_{50} and N_{eff} in r^2 and z are shown in Figure 8.3a and 8.3b, respectively. For neutron, the position dependence in r^2 and z are shown in Figure 8.4a and 8.4b, respectively. It can be seen that the position dependence of the mean N_{50} values are mostly corrected for the mean N_{eff} values.

(a) r^2

(b) z
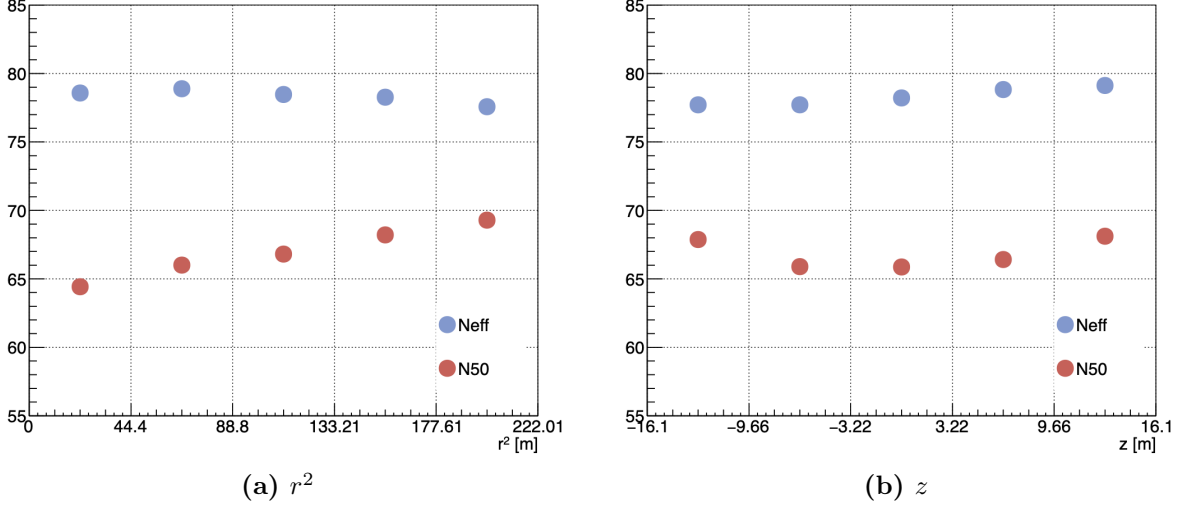
Figure 8.3: The position dependence of mean N_{50} and meanN_{eff} for electron. Red dots represent N_{50} and blue dots represent N_{eff}.

8.1.3 Comparison of the position dependence of the energy scale of electron and neutron

The deviations of N_{eff} for r^2 and z are shown in Figure 8.5a and Figure 8.6a, respectively. Green dots represent electrons and blue dots represent neutrons. Also, the differences in deviation between electron and neutron for r^2 and z are shown in Figure 8.5b and Figure 8.6b, respectively. For the position dependence of the energy scale, it is consistent within about $\pm 2\%$ between electron and neutron. This is however currently larger than the systematic uncertainty of about 0.5% in SK solar neutrino measurement. This difference is still yet to be understood. It is important to understand the causes of this in the future in order to use the spallation neutron source for electron energy scale more reliably.

(a) r^2

(b) z
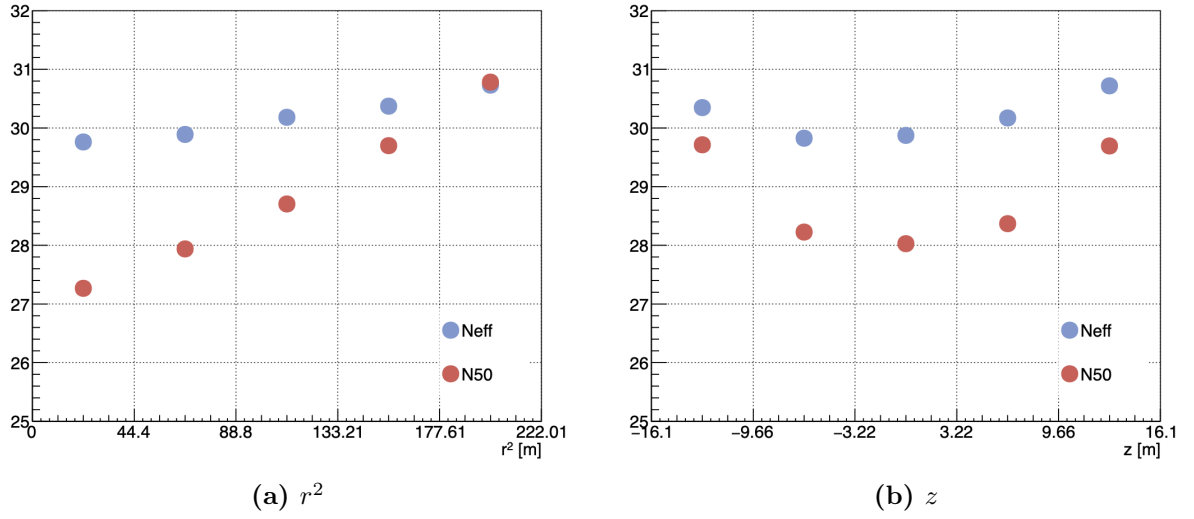
Figure 8.4: The position dependence of mean N_{50} and meanN_{eff} for neutron. Red dots represent N_{50} and blue dots represent N_{eff}.

(a)

(b)
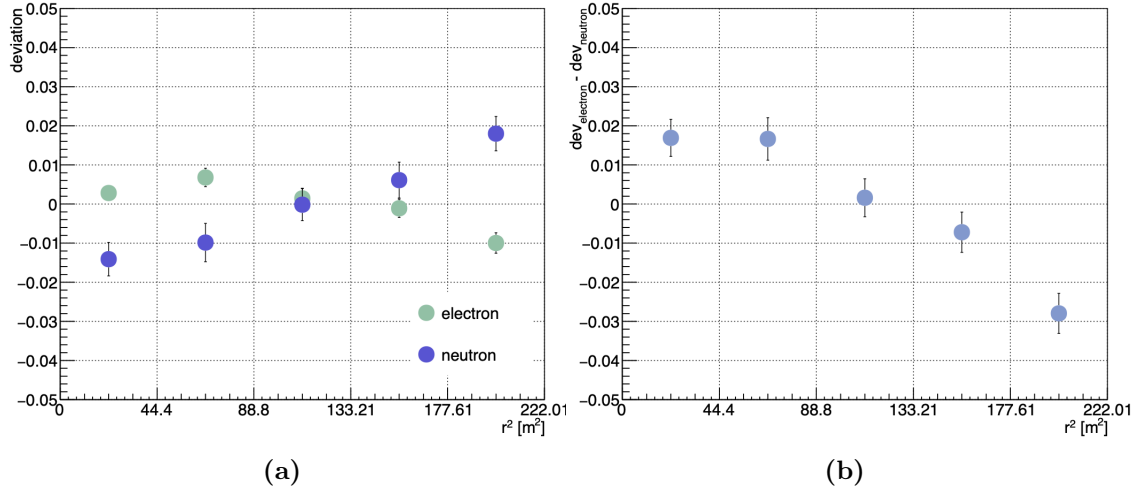
Figure 8.5: (a) The deviation of N_{eff} of electrons and neutrons by MC simulation for r^2. Green dots represent electrons and blue dots represent neutrons. (b) The difference of (a). In the range $88.8 < r^2 < 177.61\,[\mathrm{m}^2]$, they are consistent within $\pm 1\%$. The deviations of electron and neutron are about 2% around the center of the detector ($0 < r^2 < 88.8\,[\mathrm{m}^2]$) and about 3% in the outer region ($177.61 < r^2 < 222.01\,[\mathrm{m}^2]$).

(a)   (b)
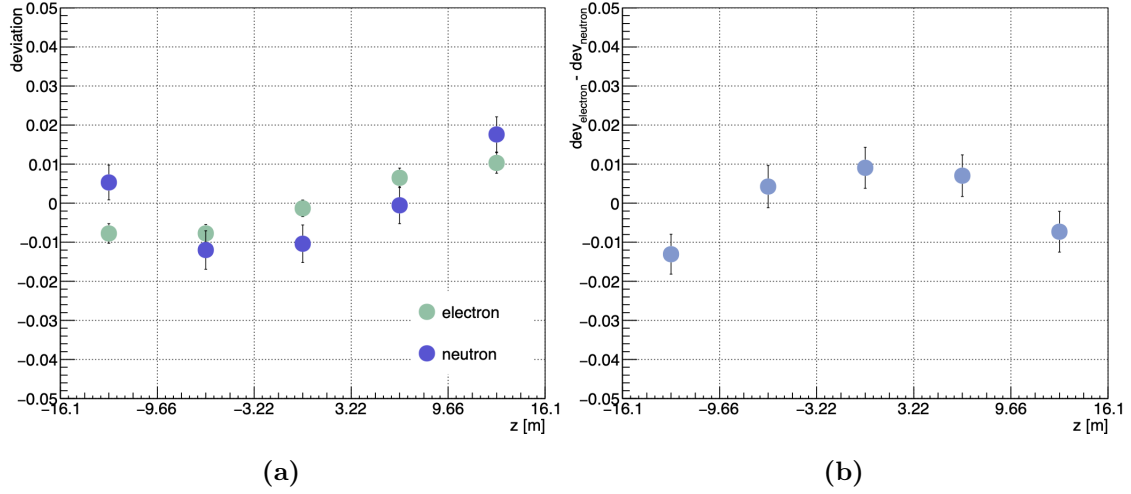
Figure 8.6: (a) The deviation of N_{eff} of electrons and neutrons by MC simulation for z. Green dots represent electrons and blue dots represent neutrons. (b) The difference of (a). In the range $-9.66 < z < 16.1\,[\mathrm{m}]$, they are consistent within $\pm 1\%$, while in the range $-16.1 < z < -9.66\,[\mathrm{m}]$ the deviations of electron and neutron are about 2%.

8.2 Comparison of MC simulation and data for spallation neutron

In order to check the reproducibility of the MC simulation, a comparison with the data is performed.

8.2.1 Results of the event reconstruction for data

The mean N_{50} and mean N_{eff} of the spallation neutron signal are evaluated using the methods described in Section 6.4.1 and the position dependence is investigated. The fitting results of electron and neutron are shown in Appendix C. The data from January 13, 2022 to March 12, 2022 is used for this study.

The position dependence of mean N_{50} and mean N_{eff} in r^2 and z are shown in Figure 8.7a and 8.7b, respectively. It can be seen that N_{eff} almost properly corrects for the effect of light attenuation in the water seen in N_{50}.

8.2.2 Comparison of the deviation of the energy scale of MC simulation and data for $\mathrm{Gd}(n,\gamma)$ signal

The deviations of N_{eff} of r^2 and z are as shown in Figure 8.8a and Figure 8.9a, respectively. Black dots represent the data and red dots represent the MC simula-

(a) r^2 **(b)** z
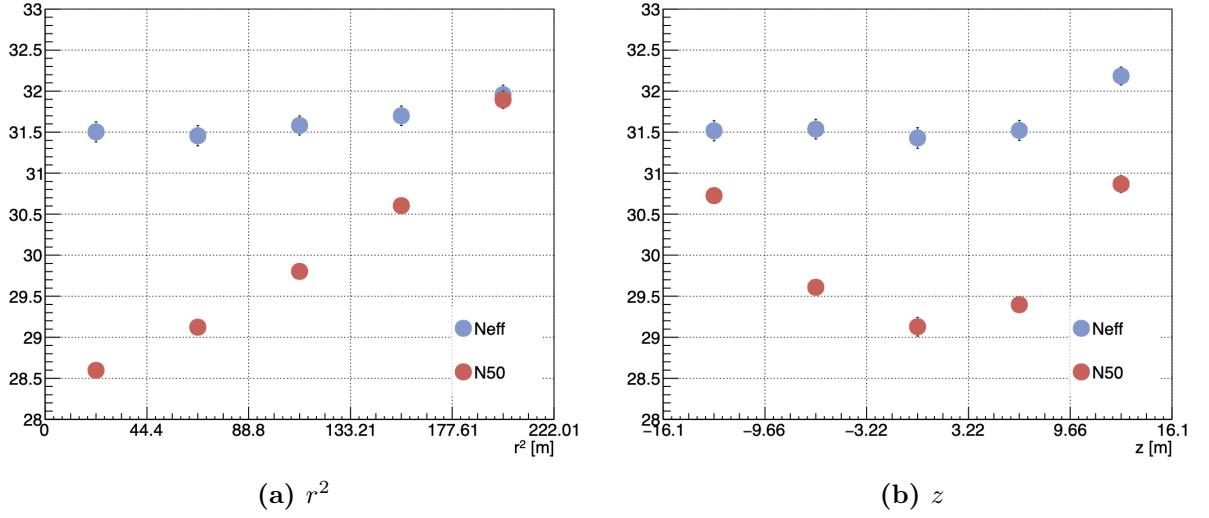
Figure 8.7: The position dependence of mean N_{50} and meanN_{eff}. Red dots represent N_{50} and blue dots represent N_{eff}. It can be seen that the position dependence seen in N_{50} (energy dropped by Cherenkov light due to attenuation of water) has been corrected.

tion. Also, the differences in deviation between electron and neutron for r^2 and z are shown in Figure 8.8b and Figure 8.9b, respectively. In the comparison of the data and the MC simulation, they are consistent within about $\pm 0.5\%$ in the range of $44.4 < r^2 < 177.61\,[\mathrm{m}^2]$ and $-3.22 < z < 16.1\,[\mathrm{m}]$. In other regions, they are consistent in the range of $\pm 1\%$. From Figure 8.8b, it can be seen that the deviation value of the MC simulation is larger than the data at the outer side of the detector. One possible reason for this is that the water transparency introduced in the current simulation is shorter than the actual data. Also, from Figure 8.9b, the difference between the data and MC simulation in the bottom region of the tank ($-16.1 < z < -3.22\,[\mathrm{m}]$) is larger than in other areas, taking into account the error size of about 0.5%. One of possible reasons of this discrepancy is that the model of the top bottom asymmetry (TBA) introduced in the current simulation has shifted in the bottom region of the tank. It is important for energy reconstruction performed using simulation to investigate these and improve the MC simulation to be more in correspondence with the data.
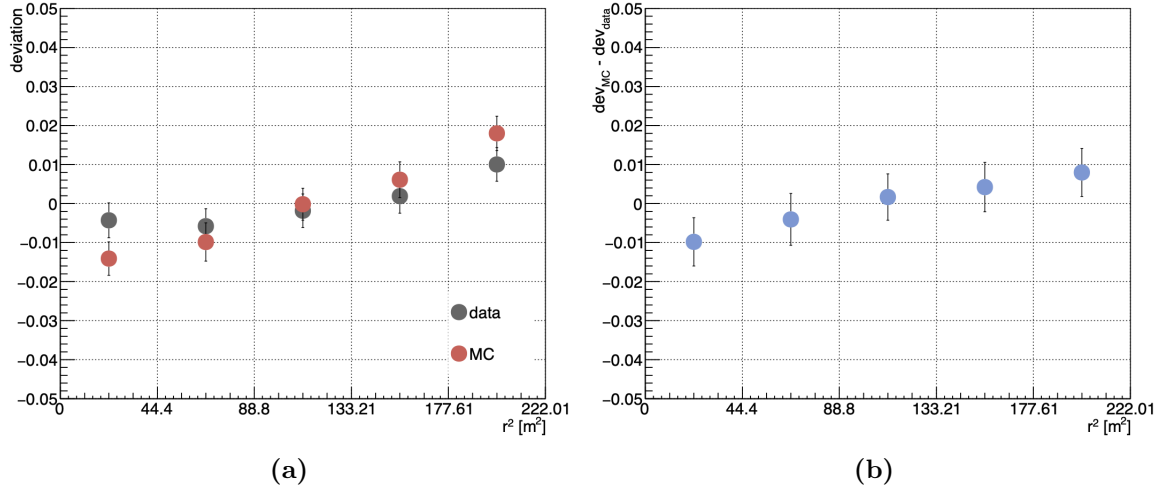
Figure 8.8: (a) The deviation of N_{eff} of the data and the MC simulation for r^2. Black dots represent the data and red dots represent MC simulation. (b) The difference of (a). The data and the MC simulation are consistent within 1% in all areas.
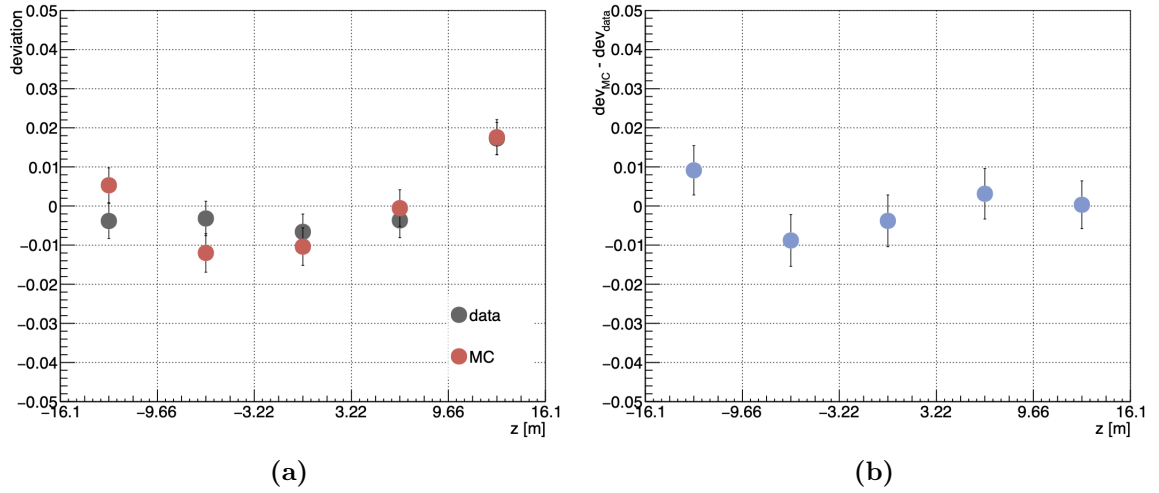
Figure 8.9: (a) The deviation of N_{eff} of the data and the MC simulation for z. Black dots represent the data and red dots represent MC simulation. (b) The difference of (a). The data and the MC simulation are consistent within 1% in all areas. The top of the tank in both data and MC shows about 2% deviation.

Chapter 9

Conclusion

In 2020, gadolinium was introduced to the Super-Kamiokande detector, and it became possible to detect neutron capture signals by Gd. We are developing a new method of calibrating energy reconstruction using spallation neutrons, produced by cosmic ray muons undergoing spallation reaction. The systematic uncertainty on the energy scale of the current solar neutrino observations is 0.54%, and the goal is to reduce this uncertainty with improved calibrations. For this purpose, the spallation neutron signal selection method was developed and the position dependence of the energy reconstruction was evaluated in detail by data and MC simulation.

Spallation neutron signals have the advantages that they can be detected throughout the entire detector at high rates, but they have also the disadvantages that the detected energy is low and background is difficult to remove, and they are affected by pile-up. In this study, the conditions of event selection was developed to reduce these effects as much as possible.

The stability and uniformity of detector response in SK-VI and the Gd concentration of Gd-loading in 2022 are evaluated using spallation neutrons. For the stability in SK-VI, the energy scale and the Gd concentration were found to be stable for the energy scale and Gd concentration at about $\pm 1\%$ and about $\pm 2\%$ respectively throughout the detector. For Gd-loading in 2022, the Gd concentration was evaluated by the number of spallation neutron signal and the neutron capture time constant with gadolinium. Both results showed a gradual increase in Gd concentration from the bottom of the tank as the days passed. After the end of Gd-loading, it was checked that the concentration became constant at the expected level.

The position dependence of the energy scale is evaluated. In SK solar neutrino observation, electrons are detected. Therefore, it is necessary to accurately evaluate the position dependence of the electron energy reconstruction. The response to neutrons and electrons are compared using MC simulation to see if spallation

neutrons can be used to evaluate the position dependence of energy of electron signal. The result is that electrons and neutrons are consistent within about $\pm 2\%$ of the entire detector. This is however a larger deviation compared to the goal of the correction within 0.5% of the position dependence. It is important to understand the causes of this in the future. Also, using the data and the MC simulation of spallation neutron, it was found that the energy value after reconstruction of the MC simulation is larger than the data at the outer side of the detector and the difference of the data and MC simulation in the bottom region of the tank $(-16.1 < z < -3.22\,[\mathrm{m}])$ are further apart than in other areas. Some possible reasons for these are that the water transparency currently introduced in the MC simulation are shorter than the actual data and that the TBA model does not match the data in the bottom of the tank. Since energy reconstruction is carried out using MC simulations, it is important to investigate these in more detail in the future and to improve the MC simulation to better reproduce the data.

Acknowledgment

Appendix A

Water circulating system

The water supplied to SK detector is purified groundwater in the Kamioka Mine. Groundwater contains impurities. Small dust and metal ions scatter or absorb Cherenkov light, reducing the transmittance of the light. Radioactive materials dissolved in water cause background events for neutrino observations. In particular, radon ^{222}Rn becomes a background for analysis near the threshold (3.5 MeV) in solar neutrino observations because radon's daughter nucleus, bismuth ^{214}Bi, emits 3.26 MeV electron through beta decay. Therefore, radon removal is essential.

In SK, water in the tank is circulated at 60 m^3/h to remove impurities and maintain purity. Water is withdrawn from the top of the detector, purified through the purifier, and then entered from the bottom of the detector. The process is below.

1. 1 μm mesh filter
   Remove dust of 1μm or more and radioactive materials attached to it.

2. Heat exchanger
   The temperature of the water in the detector rises due to the heat generated by the circulation pump and high-voltage PMT. This temperature increase causes dark noise, bacterial growth, and water convection. In order to prevent them, three heat exchangers are used for one cycle of water circulation, and water temperature is adjusted to about 13 degrees.

3. Ion exchanger
   Remove ions in water ($Fe^{2+}, Ni^{2+}, Co^{2+}, CO_3^{2-}$, etc.).

4. UV sterilizer
   Ultraviolet radiation is irradiated to kill bacteria.

5. Rn-less-air dissolving system
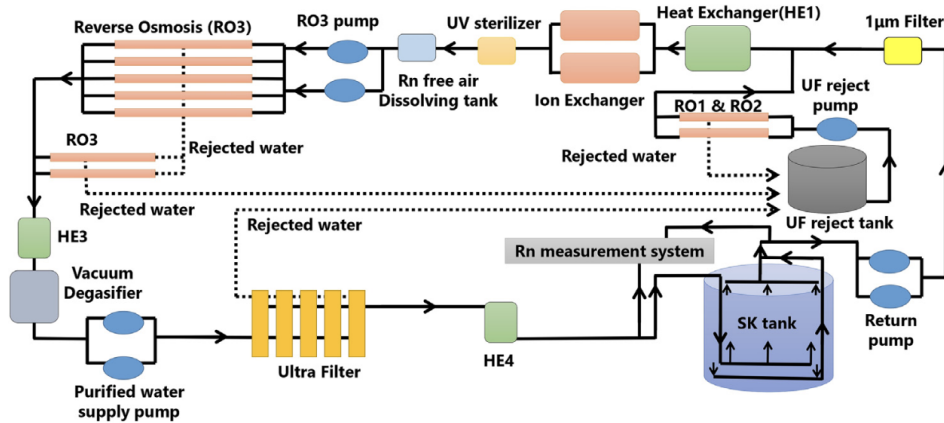
Figure A.1: Water circulating system of SK [49]

Dissolve radon-free air in pure water in order to improve the removal efficiency of radon gas in purification in a vacuum deaerator.

6. Reverse osmosis filter
   Removes organic matter with a molecular weight of about 100 by osmotic pressure and filtration.

7. Cartridge polisher
   Removes ^{222}Rn gas and oxygen dissolved in ultrapure water.

8. Ultra filter
   Removes particles larger than 10nm.

9. Membrane degasifier
   Removes ^{222}Rn left in water.

Through the above process, the purified ultrapure water has a radon concentration of ~ 1.7mBq/m^3 and the transmission length of light is about 100m. However, by water circulating system in which purified water is put in from the bottom and withdrawn from the top, there is a problem of top bottom asymmetry in water quality with higher water transmission at the bottom of the detector than at the top.

Appendix B

Calibration of Gadolinium concentration

B.1   Am/Be neutron source

Overview

Am/Be (Americium/Berylium) neutron source is used for measuring Gd concentration through the neutron capture time. Am/Be source emits neutrons and gamma rays simultaneously from americium and beryllium (B.1~B.3).

$$^{241}\text{Am} \rightarrow {}^{237}\text{Np} + \alpha \tag{B.1}$$

$$^{9}\text{Be} + \alpha \rightarrow {}^{13}\text{C}^* + \text{n} \, (2 - 6 \, \text{MeV}) \tag{B.2}$$

$$^{13}\text{C}^* \rightarrow {}^{12}\text{C} + \gamma \, (4.43 \, \text{MeV}) \tag{B.3}$$

The Am/Be source is surrounded by BGO crystal as shown in B.1. 4.43 MeV gamma ray in a BGO crystal causes photoelectric absorption, Compton scattering, or electron pair production, and scintillation light is emitted. Neutrons are identified as the delayed signal produced by subsequent neutron captures by Gadolinium.

Data acquisition and reduction

In Am/Be data acquisition, the SHE trigger threshold is set to 60 hits or 100 hits due to data transfer volume issues. When 4.43 MeV gamma ray drops its total energy in the BGO crystal, about 1000 p.e. of scintillation light is detected. This exceeds the SHE trigger threshold, so an SHE trigger [-5, 35]μs is issued, followed by an AFT trigger [35, 535]μs. Events exceeding the sub-trigger threshold within the AFT trigger become neutron capture candidates by Gd.

114

Figure B.1: Am/Be neutron source and BGO crystal. The black cylinder in the center on the left is the Am/Be source, and it is assembled by surrounding it with 8 BGO scintillators on the right.

- Prompt signal
  - SHE trigger is issued when there is a PMT hit above the SHE trigger threshold.
  - In order to distinguish between the BGO scintillation light signal and the cosmic ray muon signal, we select SHE events withtout OD trigger.

- Delayed signal
  We remove scintillation light signal of the prompt event and scintillation light from the BGO crystals due to gamma rays emitted by gadolinium. The procedure is below.
  - For the parameter g_{vtx} representing the probability of reconstruction of the event occurrence point and the parameter g_{dir} representing the probability of direction reconstruction,

$$(g_{vtx} > 0.40) \cap (g_{dir} < 0.40) \tag{B.4}$$

  - For the number of PMT hits that detected light within 30 ns around the delayed event time N_{30} and the number of PMT hits that de-
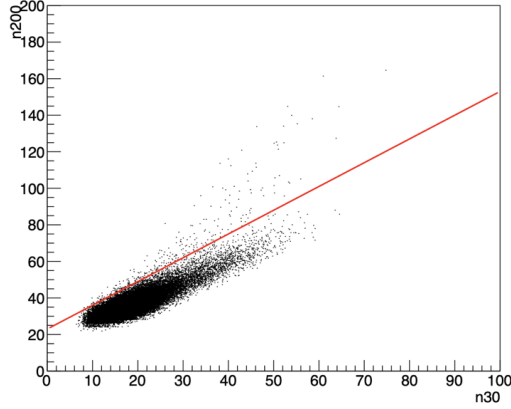
Figure B.2: Distribution of the number N_{30} of PMTs that detected light within 30 ns and the number N_{200} of PMTs that detected light within 200 ns from the delayed event occurrence time. The red line represents the straight line $N_{200} = 1.3 \times N_{30} + 23$, and the region below the straight line satisfies the condition $(N_{200} - 23)/(1.3 \times N_{30}) < 1$.

tected light within 200 ns N_{200} (Figure B.2),

$$\frac{N_{200} - 23}{1.3 \times N_{30}} < 1 \tag{B.5}$$

– For the distance d between the position where the Am/Be source is installed and the reconstructed event point (Figure B.3),

$$d < 400\text{cm} \tag{B.6}$$

Evaluation of neutron capture time constant

The neutron capture time constant is evaluated by fitting the distribution of the dime difference between the prompt and delayed events (dt) with the following function (Figure B.4):

$$f(dt) = a \left[1 - \exp\left(-\frac{dt}{4.3}\right)\right] \exp\left(-\frac{dt}{\tau}\right) + b \tag{B.7}$$

a, b, τ are derived by this fit, where a and b are the constants corresponding to the number of signal and background events respectively, and τ is the time constant for neutron capture by gadolinium. $\left[1 - \exp\left(-\frac{dt}{4.3}\right)\right]$ is the term that takes into account the neutron thermalization time. The fit is performed by tentatively fixing the time constant for neutron thermalization in water to 4.3 μs .
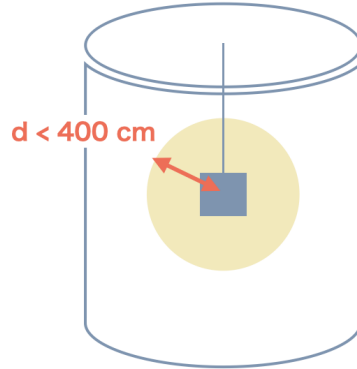
Figure B.3: Schematic diagram of the distance d between the position where the Am/Be source is installed and the reconstructed event point. Events in the region within the yellow sphere with $d < 400$cm are selected.
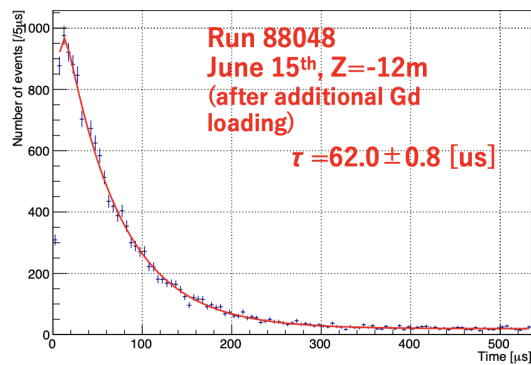
Figure B.4: The dt distribution of neutron signal from Am/Be source. Each point represents the data and the red line represents the fit function to the data.
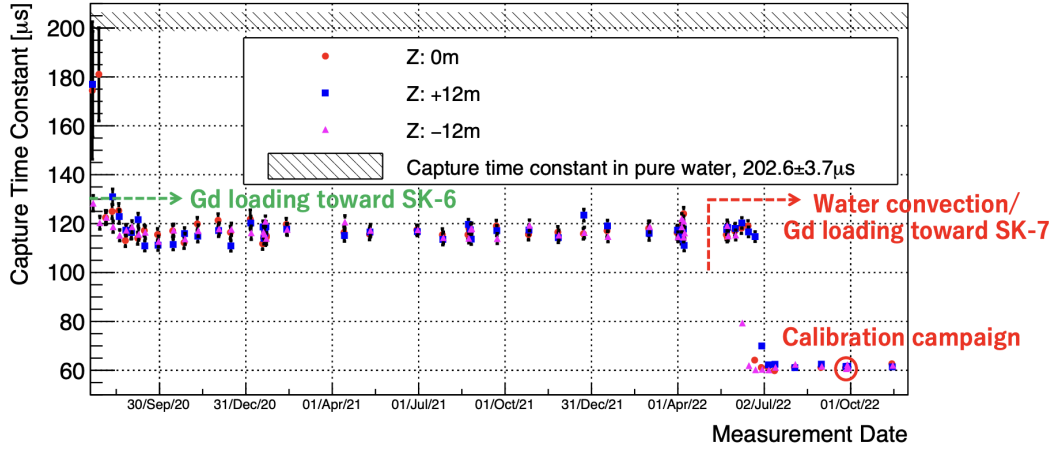
Figure B.5: History of neutron capture time constant τ by gadolinium obtained from detector calibration using Am/Be source

Monitoring of the neutron capture time constant using Am/Be source

From detector calibration using an Am/Be source, the capture time constant τ of neutrons was obtained as shown in Figure B.5. The time constant was stable at around 120 μs at SK-VI when the Gd concentration is 0.01%. After the start of SK7 with a Gd concentration of 0.03%, the time constant decreased to around 60 μs and was stable.

Appendix C

Fitting results

C.1 Position dependence

C.1.1 Electron with MC simulation

The fitting results of electron signal with MC simulation for N_{50} and N_{eff} are shown in Figure C.1 and Figure C.2, respectively. The result of position dependence of N_{50} and N_{eff} for r^2 as shown in Figure 8.3a is obtained from the mean value from the fitting as Figure C.1a and Figure C.2a, respectively. That for z as shown in Figure 8.3b is obtained from the mean value from the fitting as Figure C.1b and Figure C.2b.

C.1.2 Neutron with MC simulation

The fitting results of neutron signal with MC simulation for N_{50} and N_{eff} are shown in Figure C.3 and Figure C.4, respectively. The result of position dependence of N_{50} and N_{eff} for r^2 as shown in Figure 8.4a is obtained from the mean value from the fitting as Figure C.3a and Figure C.4a, respectively. That for z as shown in Figure 8.4b is obtained from the mean value from the fitting as Figure C.3b and Figure C.4b.

C.1.3 Neutron with data

The fitting results of neutron signal with data for N_{50} and N_{eff} are shown in Figure C.5 and Figure C.6, respectively. The result of position dependence of N_{50} and N_{eff} for r^2 as shown in Figure 8.7a is obtained from the mean value from the fitting as Figure C.5a and Figure C.6a, respectively. That for z as shown in Figure 8.7b is obtained from the mean value from the fitting as Figure C.5b and Figure C.6b.
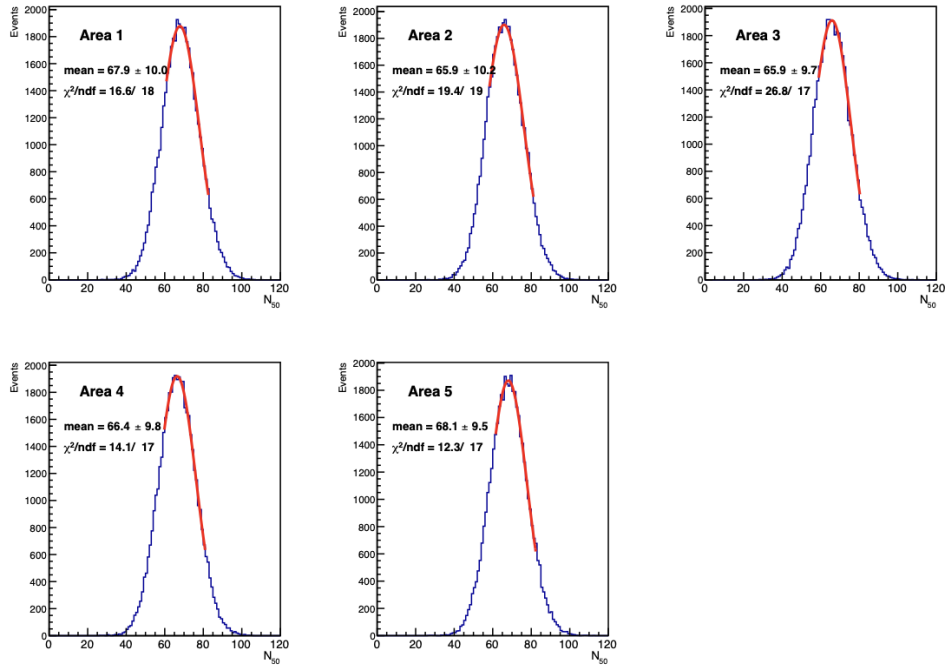
(a) r^2
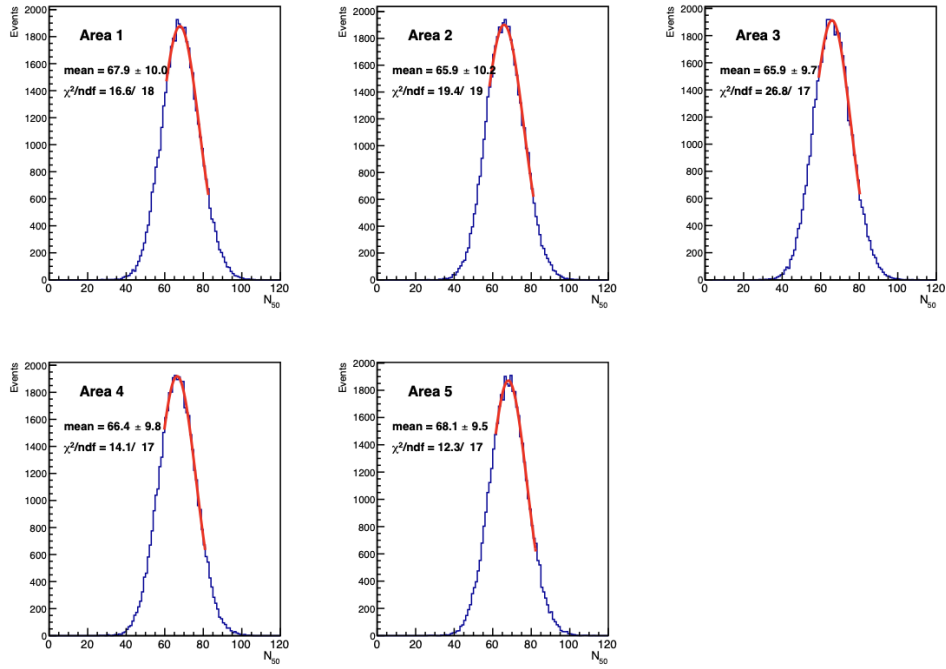
(b) z

Figure C.1: The distribution of N_{50} of electron with MC simulation for r^2 and z, and the results of fitting for each area.
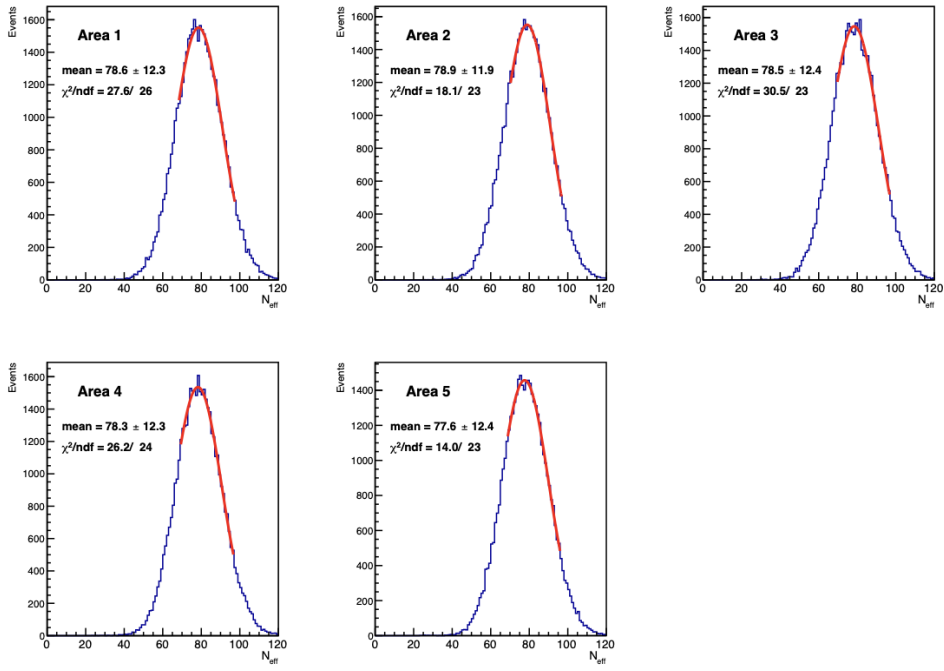
(a) r^2
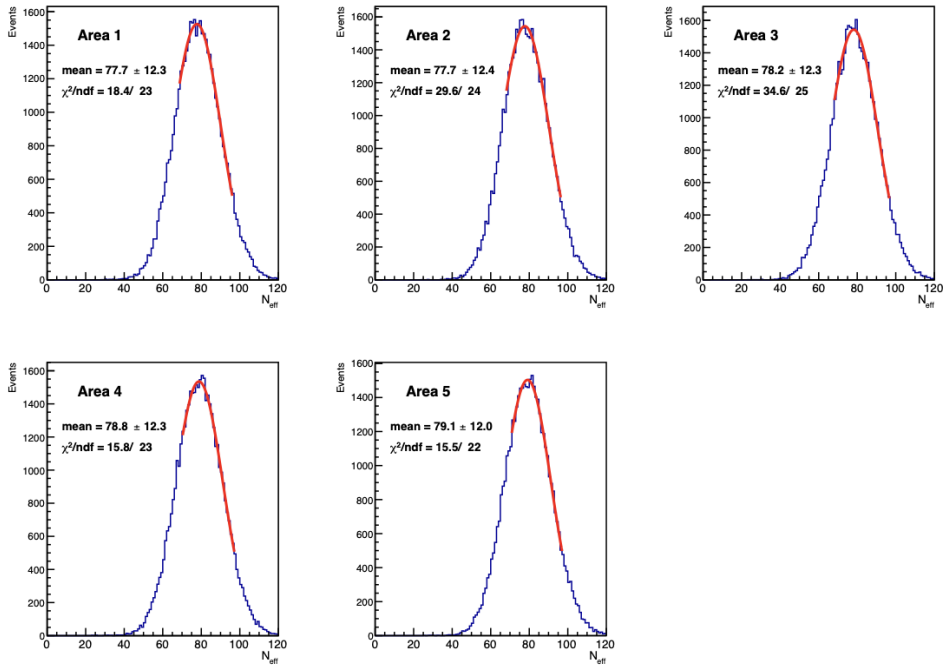
(b) z

Figure C.2: The distribution of N_{eff} of electron with MC simulation for r^2 and z, and the results of fitting for each area.
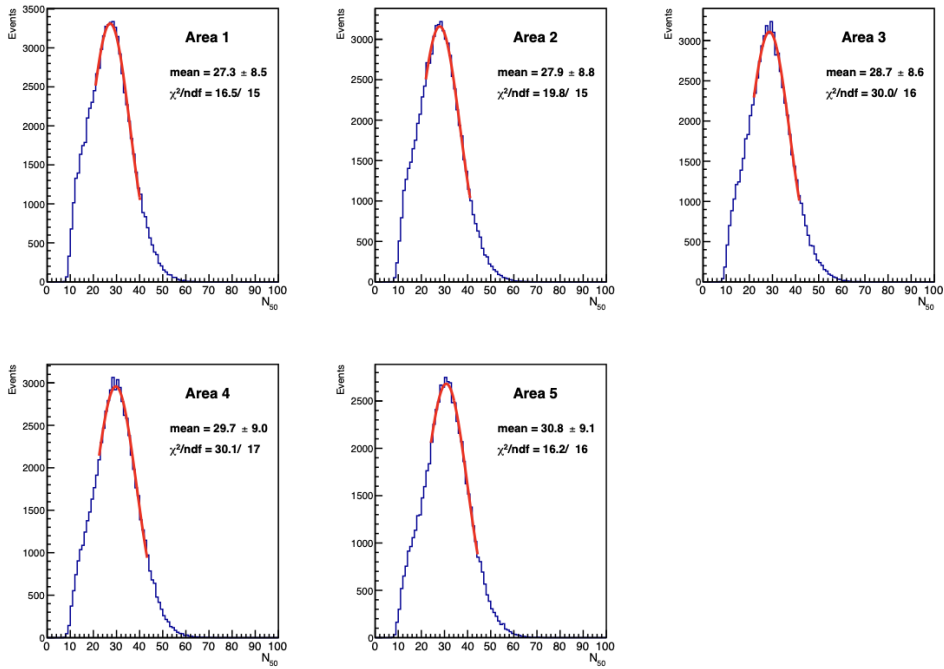
(a) r^2
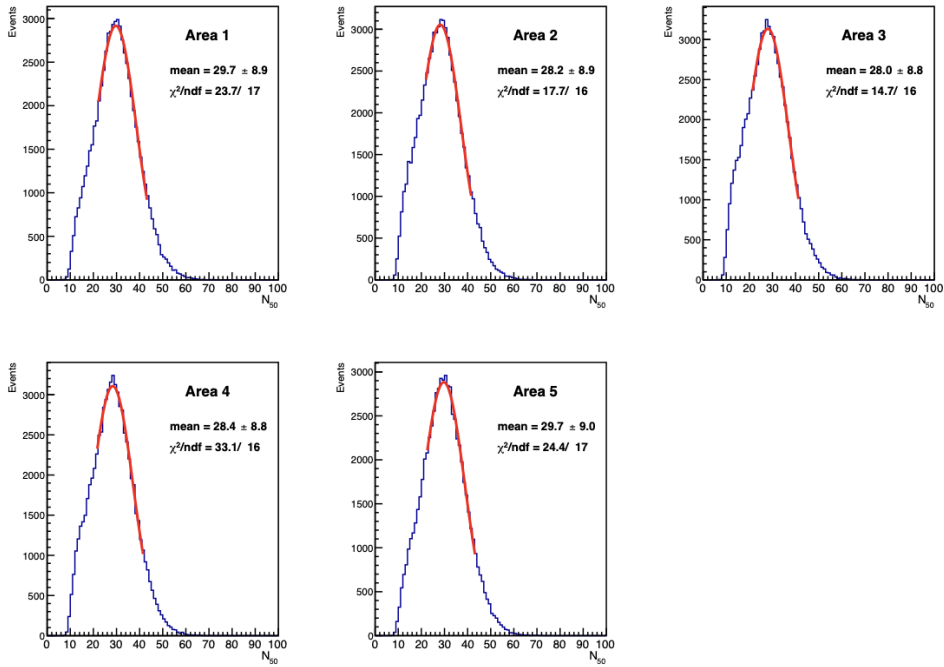
(b) z

Figure C.3: The distribution of N_{50} of $Gd(n, \gamma)$ with MC simulation for r^2 and z, and the results of fitting for each area.
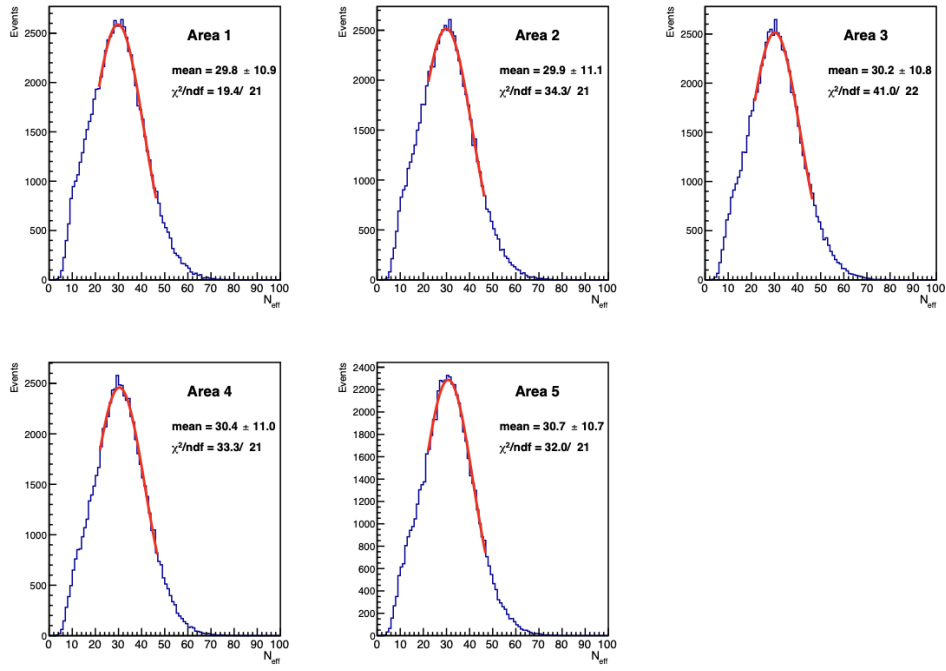
(a) r^2
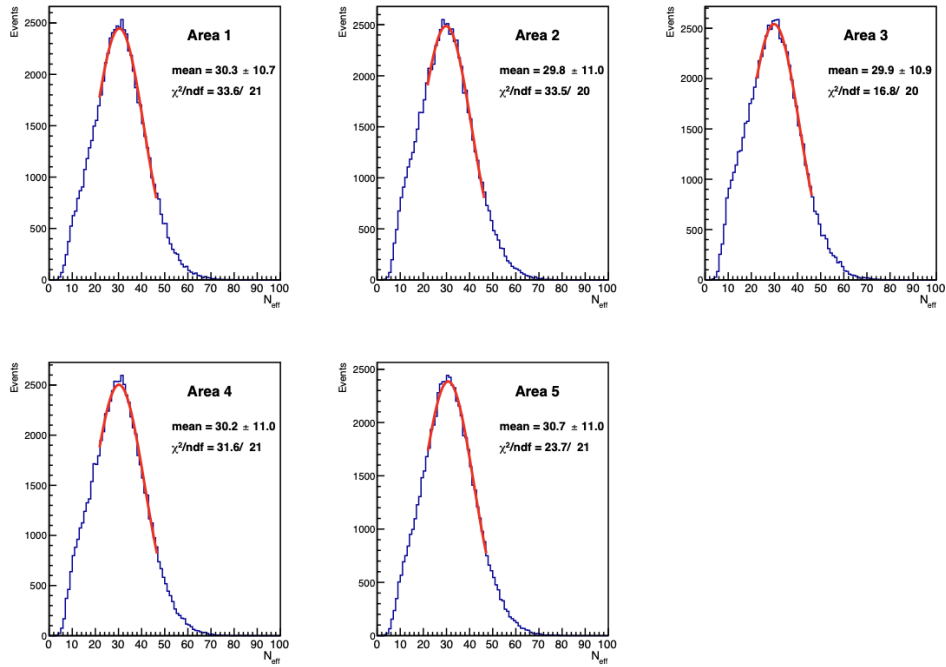
(b) z

Figure C.4: The distribution of N_{eff} of $\text{Gd}(n, \gamma)$ with MC simulation for r^2 and z, and the results of fitting for each area.
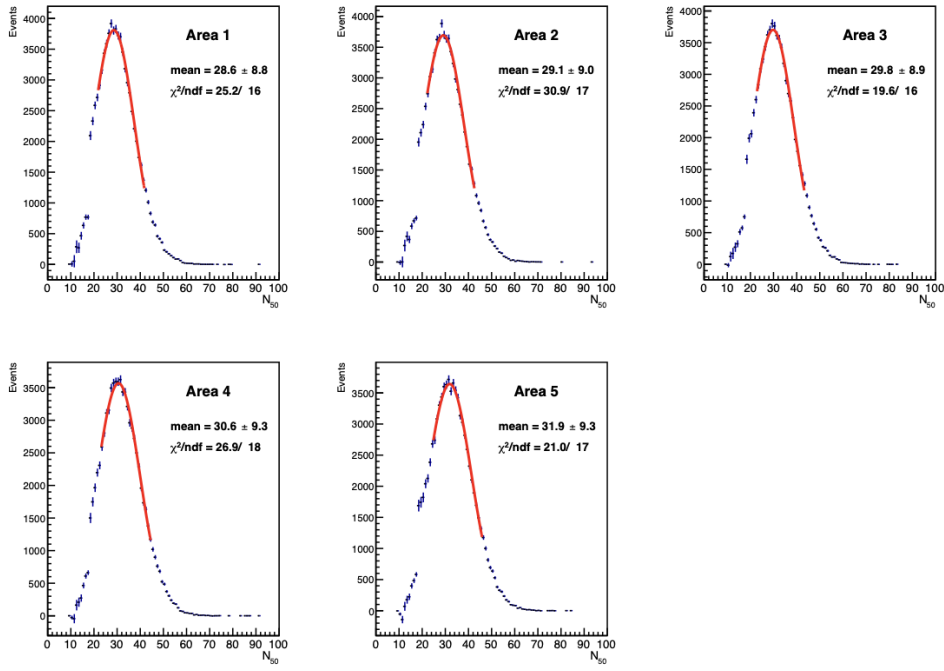
(a) r^2
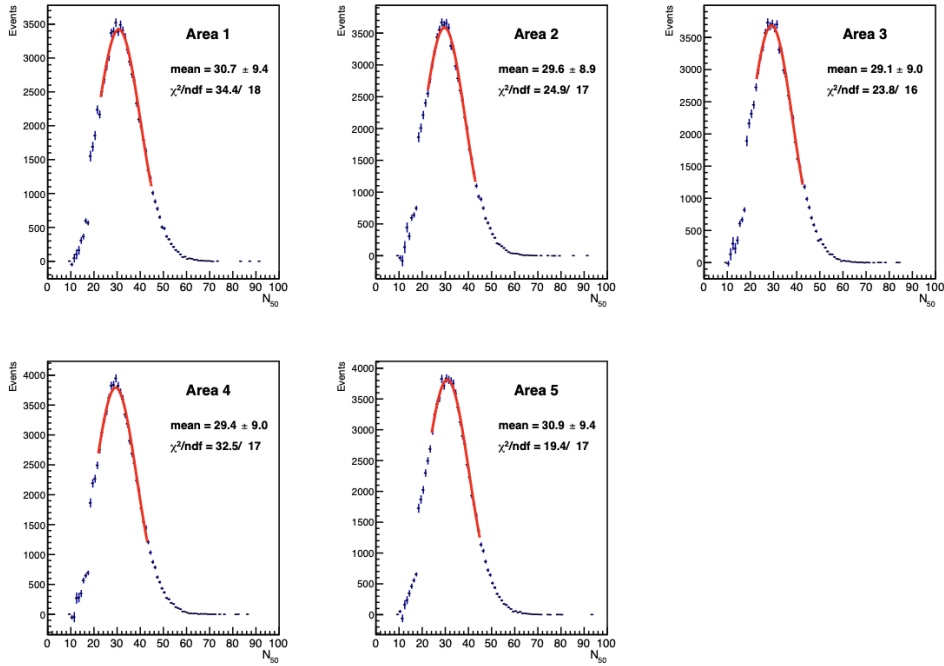
(b) z

Figure C.5: The distribution of N_{50} of spallation neutron with the data for r^2 and z, and the results of fitting for each area.
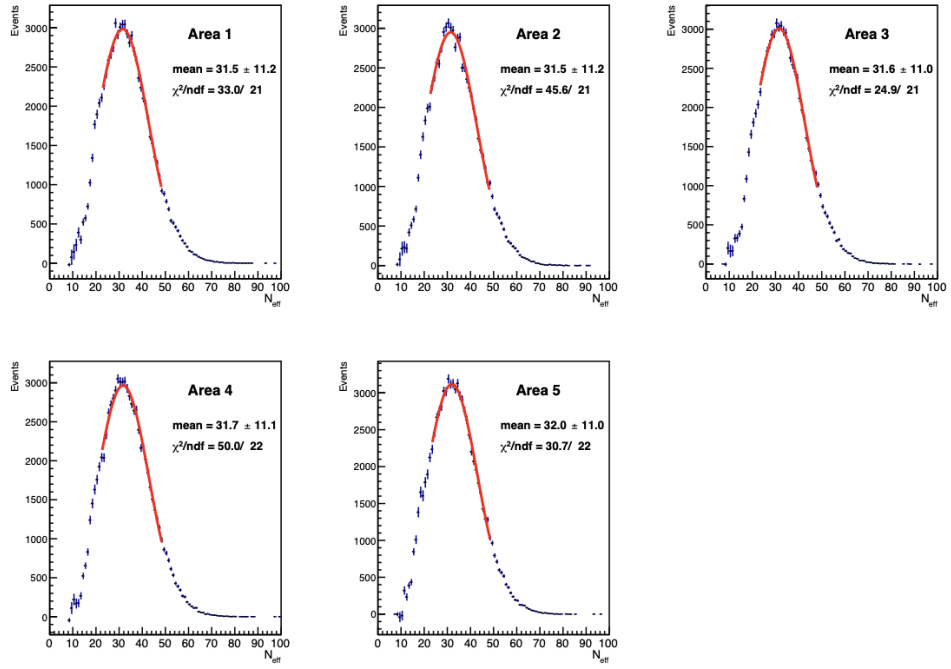
(a) r^2
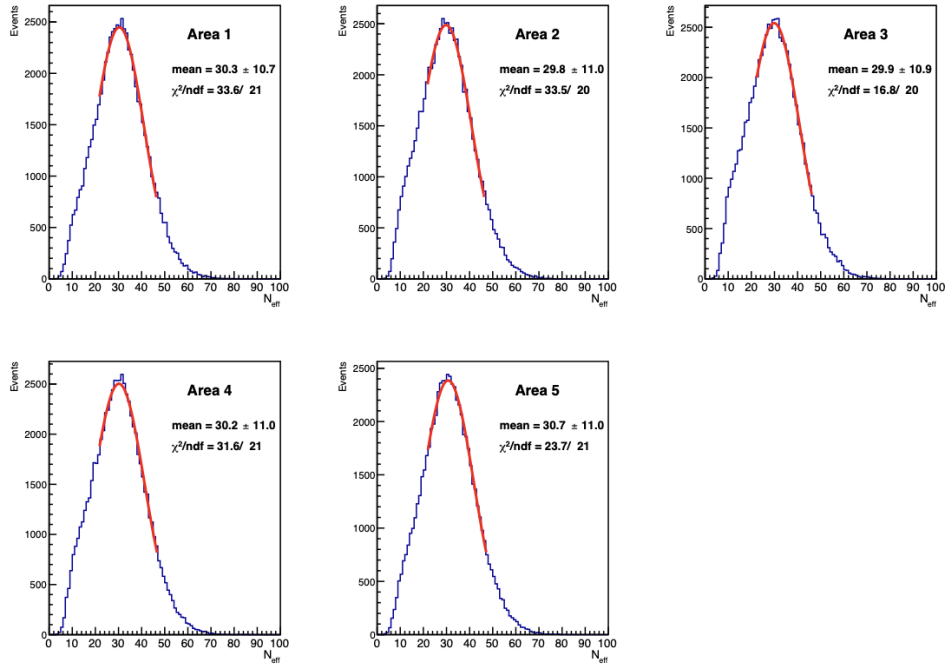
(b) z

Figure C.6: The distribution of N_{eff} of spallation neutron with the data for r^2 and z, and the results of fitting for each area.

List of Figures

131

133

List of Tables

Bibliography

[1]   C. L. Cowan et al. "Detection of the free neutrino: A Confirmation". In: *Science* 124 (1956), pp. 103–104. DOI: `10.1126/science.124.3212.103`.

[2]   Raymond Davis. "A review of the homestake solar neutrino experiment". In: *Progress in Particle and Nuclear Physics* 32 (1994), pp. 13–32. ISSN: 0146-6410. DOI: `https://doi.org/10.1016/0146-6410(94)90004-3`. URL: `https://www.sciencedirect.com/science/article/pii/0146641094900043`.

[3]   K. S. Hirata et al. "Observation of B-8 Solar Neutrinos in the Kamiokande-II Detector". In: *Phys. Rev. Lett.* 63 (1989), p. 16. DOI: `10.1103/PhysRevLett.63.16`.

[4]   M. G. Aartsen et al. "Multimessenger observations of a flaring blazar coincident with high-energy neutrino IceCube-170922A". In: *Science* 361.6398 (2018), eaat1378. DOI: `10.1126/science.aat1378`. arXiv: `1807.08816 [astro-ph.HE]`.

[5]   Y. Fukuda et al. "Evidence for oscillation of atmospheric neutrinos". In: *Phys. Rev. Lett.* 81 (1998), pp. 1562–1567. DOI: `10.1103/PhysRevLett.81.1562`. arXiv: `hep-ex/9807003`.

[6]   J. Farine. "Measurement of the rate of nu/e + d –> p + p + e- interactions produced by B-8 solar neutrinos at the Sudbury Neutrino Observatory". In: *Phys. Atom. Nucl.* 65 (2002). Ed. by V. A. Bednyakov and V. B. Brudanin, pp. 2147–2155. DOI: `10.1134/1.1530292`.

[7]   Z. Maki, M. Nakagawa, and S. Sakata. "Remarks on the unified model of elementary particles". In: *11th International Conference on High-energy Physics*. 1962, pp. 663–666.

[8]   Particle Data Group. "Review of Particle Physics". In: vol. 2022. 2022. eprint: `https://pdg.lbl.gov/`.

[9]   Y. Fukuda et al. "The Super-Kamiokande detector". In: *Nucl. Instrum. Meth. A* 501 (2003). Ed. by V. A. Ilyin, V. V. Korenkov, and D. Perret-Gallix, pp. 418–462. DOI: `10.1016/S0168-9002(03)00425-X`.

[10] Masayuki Nakahata et al. "Atmospheric Neutrino Background and Pion Nuclear Effect for Kamioka Nucleon Decay Experiment". In: *J. Phys. Soc. Jap.* 55 (1986), p. 3786. DOI: 10.1143/JPSJ.55.3786.

[11] Raymond Davis. "A review of measurements of the solar neutrino flux and their variation". In: *Nuclear Physics B - Proceedings Supplements* 48.1 (1996). Proceedings of the Fourth International Workshop on Theoretical and Phenomenological Aspects of Underground Physics, pp. 284–298. ISSN: 0920-5632. DOI: https://doi.org/10.1016/0920-5632(96)00263-0. URL: https://www.sciencedirect.com/science/article/pii/0920563296002630.

[12] S. Abe et al. "Search for Solar Flare Neutrinos with the KamLAND Detector". In: *Astrophys. J.* 924.2 (2022), p. 103. DOI: 10.3847/1538-4357/ac35d1. arXiv: 2105.02458 [astro-ph.SR].

[13] Dzh. N. Abdurashitov et al. "Solar neutrino results from SAGE". In: *Nucl. Phys. B Proc. Suppl.* 77 (1999). Ed. by Y. Suzuki and Y. Totsuka, pp. 20–25. DOI: 10.1016/S0920-5632(99)00385-0.

[14] T. A. Kirsten. "GALLEX solar neutrino results and status of GNO". In: *Nucl. Phys. B Proc. Suppl.* 77 (1999). Ed. by Y. Suzuki and Y. Totsuka, pp. 26–34. DOI: 10.1016/S0920-5632(99)00389-8.

[15] M. Agostini et al. "Search for low-energy neutrinos from astrophysical sources with Borexino". In: *Astropart. Phys.* 125 (2021), p. 102509. DOI: 10.1016/j.astropartphys.2020.102509. arXiv: 1909.02422 [hep-ex].

[16] Gabriel D. Orebi Gann et al. "The Future of Solar Neutrinos". In: *Ann. Rev. Nucl. Part. Sci.* 71 (2021), pp. 491–528. DOI: 10.1146/annurev-nucl-011921-061243. arXiv: 2107.08613 [hep-ph].

[17] P. Langacker et al. "Implications of the Mikheev-Smirnov-Wolfenstein (MSW) Mechanism of Amplification of Neutrino Oscillations in Matter". In: *Nucl. Phys. B* 282 (1987), pp. 589–609. DOI: 10.1016/0550-3213(87)90699-7.

[18] Carlo Giunti and Chung W. Kim. *Fundamentals of Neutrino Physics and Astrophysics.* 2007. ISBN: 978-0-19-850871-7.

[19] Ken'ichiro Nakazato et al. "Supernova Neutrino Light Curves and Spectra for Various Progenitor Stars: From Core Collapse to Proto-neutron Star Cooling". In: *Astrophys. J. Suppl.* 205 (2013), p. 2. DOI: 10.1088/0067-0049/205/1/2. arXiv: 1210.6841 [astro-ph.HE].

[20] K. Abe et al. "Diffuse supernova neutrino background search at Super-Kamiokande". In: *Phys. Rev. D* 104.12 (2021), p. 122002. DOI: 10.1103/PhysRevD.104.122002. arXiv: 2109.11174 [astro-ph.HE].

[21] Shunsaku Horiuchi et al. "Diffuse supernova neutrino background from extensive core-collapse simulations of 8-100M$_\odot$ progenitors". In: *Mon. Not. Roy. Astron. Soc.* 475.1 (2018), pp. 1363–1374. DOI: `10.1093/mnras/stx3271`. arXiv: `1709.06567 [astro-ph.HE]`.

[22] Ken'ichiro Nakazato et al. "Spectrum of the Supernova Relic Neutrino Background and Metallicity Evolution of Galaxies". In: *Astrophys. J.* 804.1 (2015), p. 75. DOI: `10.1088/0004-637X/804/1/75`. arXiv: `1503.01236 [astro-ph.HE]`.

[23] Cecilia Lunardini. "Diffuse neutrino flux from failed supernovae". In: *Phys. Rev. Lett.* 102 (2009), p. 231101. DOI: `10.1103/PhysRevLett.102.231101`. arXiv: `0901.0568 [astro-ph.SR]`.

[24] S. Ando, K. Sato, and T. Totani. "Detectability of the supernova relic neutrinos and neutrino oscillation". In: *Astropart. Phys.* 18 (2003), pp. 307–318. DOI: `10.1016/S0927-6505(02)00152-4`. arXiv: `astro-ph/0202450`.

[25] M. Kaplinghat, G. Steigman, and T. P. Walker. "The Supernova relic neutrino background". In: *Phys. Rev. D* 62 (2000), p. 043001. DOI: `10.1103/PhysRevD.62.043001`. arXiv: `astro-ph/9912391`.

[26] R. A. Malaney. "Evolution of the cosmic gas and the relic supernova neutrino background". In: *Astropart. Phys.* 7 (1997), pp. 125–136. DOI: `10.1016/S0927-6505(97)00012-1`. arXiv: `astro-ph/9612012`.

[27] D. H. Hartmann and S. E. Woosley. "The cosmic supernova neutrino background". In: *Astropart. Phys.* 7 (1997), pp. 137–146. DOI: `10.1016/S0927-6505(97)00018-2`.

[28] Tomonori Totani and Katsuhiko Sato. "Spectrum of the relic neutrino background from past supernovae and cosmological models". In: *Astropart. Phys.* 3 (1995), pp. 367–376. DOI: `10.1016/0927-6505(95)00015-9`. arXiv: `astro-ph/9504015`.

[29] Y. Fukuda et al. "The Super-Kamiokande detector". In: *Nucl. Instrum. Meth. A* 501 (2003). Ed. by V. A. Ilyin, V. V. Korenkov, and D. Perret-Gallix, pp. 418–462. DOI: `10.1016/S0168-9002(03)00425-X`.

[30] T. Kajita. "Status of Super-Kamiokande and the JHF-Kamioka neutrino project". In: *Conference on Physics Beyond the Standard Model: Beyond the Desert 02*. June 2002, pp. 317–329.

[31] H. Nishino et al. "High-speed charge-to-time converter ASIC for the Super-Kamiokande detector". In: *Nucl. Instrum. Meth. A* 610 (2009), pp. 710–717. DOI: `10.1016/j.nima.2009.09.026`. arXiv: `0911.0986 [physics.ins-det]`.

[32] K. Abe et al. "First gadolinium loading to Super-Kamiokande". In: *Nucl. Instrum. Meth. A* 1027 (2022), p. 166248. DOI: `10.1016/j.nima.2021.166248`. arXiv: `2109.00360 [physics.ins-det]`.

[33] John F. Beacom and Mark R. Vagins. "GADZOOKS! Anti-neutrino spectroscopy with large water Cherenkov detectors". In: *Phys. Rev. Lett.* 93 (2004), p. 171101. DOI: `10.1103/PhysRevLett.93.171101`. arXiv: `hep-ph/0309300`.

[34] K. Abe et al. "Measurement of neutrino and antineutrino neutral-current quasielasticlike interactions on oxygen by detecting nuclear deexcitation γ rays". In: *Phys. Rev. D* 100.11 (2019), p. 112009. DOI: `10.1103/PhysRevD.100.112009`. arXiv: `1910.09439 [hep-ex]`.

[35] M. Honda et al. "Improvement of low energy atmospheric neutrino flux calculation using the JAM nuclear interaction model". In: *Phys. Rev. D* 83 (2011), p. 123001. DOI: `10.1103/PhysRevD.83.123001`. arXiv: `1102.2688 [astro-ph.HE]`.

[36] Yang Zhang and Shaomin Chen. "First measurement of radioactive isotope production through cosmic-ray muon spallation in Super-Kamiokande IV". In: *PoS* ICHEP2016 (2017), p. 1014. DOI: `10.22323/1.282.1014`.

[37] K. Abe et al. "Solar Neutrino Measurements in Super-Kamiokande-IV". In: *Phys. Rev. D* 94.5 (2016), p. 052010. DOI: `10.1103/PhysRevD.94.052010`. arXiv: `1606.07538 [hep-ex]`.

[38] T.Tada. "SKG4 Water parameter tuning & QE table modification". In: SK collaboration neeting, 30 November 2022 to 3 December 2022.

[39] Y.Nakano. "^{8}B solar neutrino spectrum measurement using Super-Kamiokande IV". PhD thesis. 2015.

[40] 篠木 正隆. 「スーパーカミオカンデ–ガドリニウム実験による宇宙線ミューオン核破砕反応に由来する中性子生成率の測定」. 2021.

[41] K.Ieki. "Low Energy-specific Calibration Constants for SK-5,6". In: SK collaboration neeting, 30 November 2022 to 3 December 2022.

[42] A.Renshaw. "First Direct Evidence for Matter Enhanced Neutrino Oscillation, Using Super-Kamiokande Solar Neutrino Data". PhD thesis. 2013.

[43] 兼村 侑希. 「スーパーカミオカンデガドリニウム実験のためのエネルギースケール評価とRn濃度解析」. 2021.

[44] E. Blaufuss et al. "N-16 as a calibration source for Super-Kamiokande". In: *Nucl. Instrum. Meth. A* 458 (2001), pp. 638–649. DOI: `10.1016/S0168-9002(00)00900-1`. arXiv: `hep-ex/0005014`.

[45] Y.Nakano. "Data quality in SK7". In: SK collaboration neeting, 30 Novembe 2022 to 3 December 2022.

[46] 前川 雄音. 「光電子増倍管ノイズ低減によるスーパーカミオカンデの中性子識別向上」. 2021.

[47] Masayuki Harada, Yusuke Koshio, and Kaito Hagiwara. "Development of Geant4 based simulation for Super-Kamiokande". In: *PoS* KMI2019 (2019), p. 049. DOI: 10.22323/1.356.0049.

[48] Ajmi Ali et al. "Analysis of Gd(n,gamma) reaction with 155, 157 and natural Gd targets taken with JPARC-ANNRI and development of Gd(n,gamma) decay model for Gd-doped neutron/neutrino detectors". In: *PoS* ICHEP2018 (2019), p. 120. DOI: 10.22323/1.340.0120.

[49] Y. Nakano et al. "Measurement of the radon concentration in purified water in the Super-Kamiokande IV detector". In: *Nucl. Instrum. Meth. A* 977 (2020), p. 164297. DOI: 10.1016/j.nima.2020.164297. arXiv: 1910.03823 [physics.ins-det].